Response properties of open shell molecules and their application in studies of electron paramagnetic resonance parameters

Dissertation
zur
Erlangung des Doktorgrades (Dr. rer. nat.)
der
Mathematisch-Naturwissenschaftlichen Fakultät
der
Rheinischen Friedrich-Wilhelms-Universität Bonn

vorgelegt von
Van Anh Tran
aus
Leipzig

Bonn, Juni 2023

Angefertigt mit Genehmigung der Mathematisch-Naturwissenschaftlichen Fakultät
der Rheinischen Friedrich-Wilhelms-Universität Bonn

1. Gutachter: Prof. Dr. Frank Neese
2. Gutachter: Prof. Dr. Stefan Grimme

Tag der Promotion: 10.10.2023
Erscheinungsjahr: 2023

ABSTRACT

The synergy of experimental and theoretical investigations is highly powerful and is therefore utilized to gain a deeper understanding of (bio)chemical processes. Especially, molecular spectroscopy provides detailed information and thus, serves as a perfect meeting ground for the experimental and theoretical world. Therefore, quantum theoretical methods have to be refined towards more accurate computations of spectroscopic properties.

In this work, both the development of new quantum methods to calculate molecular properties of open shell species and a joint venture of sophisticated experiments with high level theory to investigate solvation effects on electron paramagnetic resonance (EPR) properties are presented.

EPR is a powerful spectroscopic method to study open shell molecules, with the electronic g-tensor being one of its key parameters. We developed an efficient implementation to compute the g-tensor at the level of second-order Møller-Plesset perturbation theory (MP2) using the resolution of identity (RI) approximation for an efficient treatment of the two-electron integrals. To circumvent the gauge problem, which is present for all magnetic property calculations, gauge including atomic orbitals (GIAOs) are applied. The implementation additionally enables calculations at double-hybrid density functional theory (DHDFT) level, of which we have tested the B2PLYP and DSD-PBEP86 functional next to pure RI-MP2. The computed g-values were compared to experimental values and published data from other methods, including coupled cluster singles doubles (CCSD). The results show a clear improvement of DHDFT upon RI-MP2 and good agreement with experimental values, however still being outperformed by the hybrid functional B3LYP for the tested set of small radicals. Evaluation of the computational performance for medium and large size radicals revealed that the RIJCOSX approximation for two-electron integrals distinctly reduces the time for large molecules which consist of more than 100 electrons.

In the joint study, we investigated a nitroxide spin label, HMI, in aqueous solution. Here, we computed the g-tensor and hyperfine couplings (HFCs) for a large set of "HMI in water" configurations (snapshots) to mimic the experimental sample. We conducted an elaborate calibration study to set-up a quantum mechanical/molecular mechanical (QM/MM) model. This facilitated calculations for many thousand snapshots. The established scheme includes HMI and all water molecules up to the second solvation shell in the QM regime, whereas the remaining waters were treated as point charges. Applying DLPNO-CCSD as the most efficient and accurate method for HFC calculations today, provided very good agreement with experiment. Furthermore, we investigated the g-strain effect, which is associated with the distribution of g-values within the measured sample, from a purely theoretical perspective for the first time. For this, we simulated “theoretical spectra” based on the set of computed EPR parameters at different spectrometer frequencies and compared those directly to the experimental EPR spectra. These investigations revealed that the g-strain mainly originates from the conformational flexibility of the molecule itself and is barely influenced by the explicit number of hydrogen bonds formed around the nitroxy group, but rather by solvation as such.

List of publications

Published parts of this thesis

Parts of this thesis have appeared in the following publications:

- **Tran, V. A.**; Teucher, M.; Galazzo, L.; Sharma, B.; Pongratz, T.; Kast, S. M.; Marx, D.; Bordignon, E.; Schnegg, A.; Neese, F. *The Journal of Physical Chemistry A* **2023**, *127*, 6447, DOI: `10.1021/acs.jpca.3c02879`.

  "Dissecting the Molecular Origin of g -Tensor Heterogeneity and Strain in Nitroxide Radicals in Water"

  I performed all single-point quantum chemical calculations (except for those including EC-RISM), the simulation of the theoretical EPR spectra, and analysis in this work while collaborating with and being advised by my coauthors.

  This article is in copyright by the authors and licensed under the Creative Commons Attribution 4.0 International (CC BY 4.0) license.

- Sharma, B.; **Tran, V. A.**; Pongratz, T.; Galazzo, L.; Zhurko, I.; Bordignon, E.; Kast, S. M.; Neese, F.; Marx, D. *Journal of Chemical Theory and Computation* **2021**, *17*, 6366, DOI: `10.1021/acs.jctc.1c00582`.

  "A Joint Venture of Ab Initio Molecular Dynamics, Coupled Cluster Electronic Structure Methods, and Liquid-State Theory to Compute Accurate Isotropic Hyperfine Constants of Nitroxide Probes in Water"

  I performed the calibration studies, the evaluation of the QM/MM model, and all single-point quantum chemical calculations (except for those including EC-RISM or CPCM) while collaborating with and being advised by my coauthors.

  This article is in copyright by the authors and licensed under the Creative Commons Attribution 4.0 International (CC BY 4.0) license.

- **Tran, V. A.**; Neese, F. *The Journal of Chemical Physics* **2020**, *153*, 054105, DOI: `10.1063/5.0013799`.

"Double-Hybrid Density Functional Theory for g-Tensor Calculations Using Gauge Including Atomic Orbitals"

I performed all derivations, implementation, benchmark calculations, and analysis in this work while being advised by my coauthors.

This article is in copyright by the authors and licensed under the Creative Commons Attribution 4.0 International (CC BY 4.0) license.

Further publications

- Auer, A. A.; **Tran, V. A.**; Sharma, B.; Stoychev, G. L.; Marx, D.; Neese, F. *Molecular Physics* **2020**, *118*, e1797916, DOI: `10.1080/00268976.2020.1797916`.

  "A Case Study of Density Functional Theory and Domain-Based Local Pair Natural Orbital Coupled Cluster for Vibrational Effects on EPR Hyperfine Coupling Constants"

- **Tran, V. A.**; Pernpointner, M. *Chemical Physics* **2018**, *509*, 151, DOI: `10.1016/j.chemphys.2017.10.001`.

  "A Quantum Dynamical Study of the Photoelectron Spectra and the Renner-Teller Effect in BrCN and ClCN Based on Four-Component Potential Energy Hypersurfaces"

Acknowledgements

First and foremost, I want to express my gratitude to my supervisor, Prof. Dr. Frank Neese, for providing me with these highly interesting and complementary topics that allowed me to dive into the beauty of science and eventually resulted in the work presented in this thesis.

I also want to thank Prof. Dr. Stefan Grimme for being my second supervisor at the Rheinische Friedrich-Wilhelms-Universität Bonn.

A great part of this work would not have been possible without the magnificent RESOLV collaboration. I therefore want to thank Prof. Dr. Enrica Bordignon, Dr. Laura Galazzo, Prof. Dr. Stefan M. Kast, Prof. Dr. Dominik Marx, Dr. Tim Pongratz, Dr. Alexander Schnegg, Dr. Brikramjit Sharma, and Dr. Markus Teucher for their expertise and effort in our joint venture as well as all the fruitful discussions in which we managed to converge so many different perspectives.

Moreover, I want to thank the ORCA development team – of which I had the privilege to be part of – for all the support, helpful discussions and this team's great work that allowed to me conduct the studies presented here.

Special thanks go to the head of development of ORCA, Dr. Frank Wennmohs aka (Meister) FrankW, for always listening, discussing and providing help – whether it is about weird coding stuff I did not get, fractals, coffee universally, fonts and design, the beauty of LaTeX, encryption and cybersecurity or bags and bikes – for introducing us to the cool stuff such as AoC and mechanical keyboards, or simply for keeping the group together!

Furthermore, I am grateful to the International Max Planck Research School on Reactive Structure Analysis for Chemical Reactions (IMPRS-RECHARGE) for its financial support and the colleagues I have met while being part of it. I especially enjoyed our organization of the symposium on "Catalysis Towards Greener Chemistry" in 2019.

My time in Mülheim would not have been the same without Alexander A., Anneke D., Baptiste D., Benjamin H.-P., Christine S., Corentin P. (best office mate ever!), Diana Y.-T. (the superwoman!), Eduardo S., Georgi S., Gosia K., Hang X., Jilly B., Laure D., Lorenz L., Lucas L., Marvin L., Maxime T., Michael B., Miquel G., Mireia F.-M., Nico S., Nicolas F., Ola W., Pauline C., Rebecca P., Róbert I., Romain B.-P., Saskia S., Spencer L., Stan P., Tim T., and Xin G. Thank you for onboarding me, accompanying me, walks in the sun, swimming in the morning, runs in the evening, cooking nights, (food) excursions, insightful lunch breaks, deep discussions, and simply for making the past years so memorable. In particular, I want to thank Anneke, Diana, Lorenz, Marvin, and Pauline for carefully proofreading this thesis.

Thank you, Lorenz, for being by my side, for your support, and encouragement to grow beyond myself.

Last but not least, I am more than grateful to my family – my sister Kiều, my mother Thúy, and my father Quân – for their unconditional love, support, and confidence in me. Không có bố mẹ và nửa nạc nửa mỡ thì đã không có bài luận án này. Cảm ơn bố mẹ nuôi dạy con, ủng hộ con với tất cả và luôn luôn tin vào khả năng của con.

cho bố mẹ và nửa nạc nửa mỡ

"I find it fascinating that you can look at the same problem from different perspectives and approach it using different methods."

– Maryam Mirzakhani

Contents

1 Introduction

Experiment and theory constitute the two counterparts of science and their synergy are of great power. Their joint application can lead to a deeper understanding of core problems in (bio)chemistry such as a system's stability and reactivity at a molecular level as well as the mechanisms that drive a reaction and processes in nature.[6–8] Highlights that illustrate this power include the *oxygen evolving complex* (*OEC*) in photosystem II as one of the most intensively studied systems, nitrogenase as one of the key enzymes in biochemistry, and complex systems in heterogeneous catalysis such as metal oxides on silica.[6]

OEC is the part of photosystem II where the highly efficient oxidation of water to hydrogen and oxygen happens in nature. Hence, understanding this process is of great interest in energy research that strives for clean-energy solutions. The humongous amount of spectroscopic data were hard to interpret until carefully calibrated computational studies shone light onto the geometric and electronic structure of OEC and its mechanism.[9–14]

Nitrogenase on the other hand is the enzyme that catalyzes the reduction of dinitrogen to ammonia. This key reaction is realized by the Haber-Bosch-process in industry, but at a very inefficient level. Structural details of nitrogenase can help understanding how this reaction happens so efficiently in nature. However, the full characterization of the active site of nitrogenase, more specifically the identification of the light atom found in the center of the active site by X-ray crystallography[15], was only accomplished by a combined study based on X-ray emission spectroscopy and quantum chemical calculations.[16–19] This case additionally illustrates the importance of choosing a property that is sensitive to the structural detail of interest.[6]

Heterogeneous catalysis is a more sophisticated field since it involves the interaction of a non-solid reactant with a solid catalyst. This leads to an extended space of possible conformations and complex dynamics between surface and adsorbate.[20, 21] However, theory has put great effort into the development of methods and models to treat such systems.[22, 23] Here, theory can help to shrink the pool of possible structures to be considered in the explanation of the catalytic function as successfully shown by a study of vanadium oxide on silica.[24–26] Furthermore, the proof that cluster models converge to the same values as periodic calculations enables the computation of energies and properties by wave function based methods.[27–29]

These highlights demonstrate that a common meeting ground between experiment and theory is essential to leverage synergetic effects in science. Perfect candidates to bridge those two counterparts are spectroscopic observables due to their wealth of information. This wealth arises from their sensitivity to the electronic structure and geometry of the molecular system under investigation and the wide range of experimental set-ups that can be applied. As a result, modern experimental spectroscopy enables recording complex spectra that are barely interpretable without any help from the theoretical toolbox. For this purpose, well-defined models are required to accurately link theoretical results to experimental findings. For one thing, theory can help to assign structure-property relationships and disentangle the experimental complexity by switching on and off effects to which the investigated property is sensible. On the other hand, the large amount of available accurate spectroscopic data serves as an important benchmark to test and validate theoretical calculations and quantify their reliability and accuracy.[8] Once accurate computational methods are established, wide-ranging cross-correlations between different experimental observations become possible and the computational methods can be used in a predictive manner.[6, 30]

Electron paramagnetic resonance (*EPR*) spectroscopy is a powerful tool to analyze open shell systems, starting from small radicals up to large biologically active systems. Advances in EPR technology enable recording high resolution spectra today. In addition, the high sophistication reached in the interpretation of the spectra based on the *Spin-Hamiltonian* (*SH*) formalism provides a great stimulus for quantum chemistry to develop more accurate methods to predict SH parameters.[31–33] In fact, quantum chemistry can be of great use for the interpretation of high resolution EPR spectra as thoroughly discussed in the literature.[34]

Comprehensive introductions into the theory of EPR parameters are provided by Harriman[35] and McWeeny[36–38]. One of the central SH parameters is the electronic *g-tensor* which describes the interaction of the fictitious electron spin with an external magnetic field. The g-tensor (more properly referred to as g-matrix as g itself does not have tensorial properties[34, 39]) is a global property of a paramagnetic system. As such it contains information about the geometric structure as well as the spin distribution of the corresponding system.

In some early work, g-tensors were investigated in a wave function based ab initio context.[40–44] A substantial amount of effort has gone into the implementation of accurate g-tensor calculations starting from an unrestricted Slater determinant as in *Hartree-Fock* (*HF*) theory. Thereby, the required quantities are typically computed from a non-relativistic wave function using linear response theory.[45–47] These studies revealed that dynamic electron correlation is essential in order to obtain accurate results.[47] Lushington and Grein were the first to use elaborate *multi-reference configuration interaction* (*MR-CI*) methods in g-tensor calculations based on a *sum-over-states* (*SOS*) formulation.[48, 49] Along the same lines, Neese and coworkers have previously introduced the so-called *spectroscopy oriented multi-reference configuration interaction* (*SORCI*) variant and applied it, among other systems, to several smaller transition metal complexes.[50, 51] However, considering the high computational effort and the lack of size consistency, such methods are impractical for routine use in computational chemistry on larger systems. Hence, size consistent single-reference methods are particularly promising candidates for accurate g-tensor calculations. In fact, Gauss et al. implemented the g-tensor at *coupled cluster singles doubles* (*CCSD*) level, making it the most accurate method available up to now.[52] Extended work along these lines has recently been reported by Perera et al.[53] All these studies demonstrated the substantial impact of correlation on the accuracy of computing g-tensors, whereas the effects of orbital relaxation were found to be very limited.

Given the explosive costs of the post-HF methods with increasing system size, the focus of method development has subsequently shifted towards *density functional theory* (*DFT*) which has shown very good price/performance ratios in many areas of computational chemistry. Schreckenbach and Ziegler implemented an algorithm for the g-tensor calculation using *gauge including atomic orbitals* (*GIAOs*)[54] to circumvent the "gauge dependency problem" of magnetic properties, albeit its effect on the g-tensor is not as pronounced as for *nuclear magnetic resonance* (*NMR*).[55–58] This method was then applied to large molecules.[59, 60] Neese and coworkers have previously presented an elaborate study on the electronic g-tensor based on the *coupled-perturbed self-consistent field* (*CP-SCF*), making the use of *unrestricted Hartree-Fock* (*UHF*) and hybrid functional calculations possible.[47, 61] More recently, Glasbrenner et al. studied the gauge-origin dependence of g-tensor calculations in detail and implemented a low-order scaling DFT based method.[62, 63] Distinct effort was also made in the treatment of the *spin-orbit coupling* (*SOC*) by which the g-tensor is dominantly affected. The importance of high-order *spin-orbit* (*SO*) effects for heavy-element compounds amplified the development within the two- and four-component approaches.[64] Important contributions to relativistic DFT were made by van Lenthe et al. Applying the *zeroth-order regular approxi-*

mation (*ZORA*) to the Dirac equation SO coupling effects are taken into account variationally.[65] An alternative DFT formalism was presented by Malkina et al. They reported the usage of both the all-electron atomic mean-field approximation to the complete Breit-Pauli SO operators and the combination of quasi-relativistic *effective core potentials* (*ECPs*) with SO-ECPs for g-tensor calculations, allowing an inexpensive yet accurate treatment of the SO coupling.[66] Mean field spin-orbit operators and their multicenter generalization[67] where also used in previous work of Neese et al.[47] In this study, calculations on a series of small organic radicals were reported at HF and DFT level, covering a range of the "Jacob's ladder"[68]: *local density approximation* (*LDA*), *generalized gradient approximation* (*GGA*) and hybrid functionals (e.g., B3LYP).[47] The results were compared not only to experimental values, but also to other results obtained by Schreckenbach and Ziegler, MR-CI results by Lushington and Grein and results based on the ZORA treatment of the SO coupling.[56, 57, 65, 66] The best agreement with experiment was found for the hybrid density functional B3LYP. The inclusion of exact Fock exchange seems to compensate the missing explicit treatment of electron correlation effects to a certain extent. Nonetheless, DFT is still limited within the accurate prediction of g-tensors for transition metal complexes as reported by Kaupp and co-workers in extensive studies including global and local hybrid functionals.[69–72]

The next higher level DFT methodology, fifth and highest rung as of today, that comes after hybrid DFT is *double-hybrid density functional theory* (*DHDFT*) according to "Jacob's ladder". Here, not only exact Fock exchange but also non-local correlation contribution is included by taking into account virtual *molecular orbitals* (*MOs*). Such functionals may be realized in the DHDFT context as proposed by Grimme.[73] Thereby, a fraction of wave function based correlation is mixed into a DFT functional and computed using the *second order Møller-Plesset perturbation theory* (*MP2*) energy expression. Double-hybrid functionals have shown excellent performance for total energies and other properties in a large body of benchmark calculations.[74] Given the more elaborate form of the energy expression and its non-variational nature, the calculation of properties is much more involved in DHDFT compared to standard DFT. Early on, the geometry gradient has been formulated by Neese et al.[75, 76] while analytic second derivatives were reported by Johnson et al. and Stanton et al.[77, 78] More recently, Stoychev et al. have shown that the DHDFT approach allows for the efficient and accurate prediction of nuclear magnetic resonance shielding tensors.[79] This marks the first implementation of analytic second derivatives including GIAOs for closed shell systems and renders the extension to open shell systems as an evident next step.

The other central parameter characterizing an EPR spectrum is the *hyperfine coupling* (*HFC*) constant (or A-tensor) that describes the interaction between the electron spin and the magnetic moment of a given nucleus. This parameter is highly sensitive to the chemical environment of the corresponding nucleus which is why hyperfine EPR spectroscopy is often used to extract local information.[80–82] In the context of quantum chemistry HFC is a first order property if considering light atoms and therefore solely depends on an accurate description of the spin density whereas the second order SOC term is of importance for heavier elements, such as transition metals.[83–85] In fact, a proper description of the origin of the spin density at a nucleus is key to understand the mechanism of HFC[86] which strongly depends on the level of theory applied.[87–91] HF based calculations give wrong results due to a poor description of core level spin polarization and the lack of electron correlation.[92–94] Hence, the inclusion of higher excitations are necessary for accurate spin densities, more precisely, highly correlated methods such as *configuration interaction singles doubles* (*CISD*) or CCSD are required. This limits the application of post-HF calculations of HFCs to small organic radicals or light main group systems. Thus, many DFT studies were conducted at different rungs of "Jacob's ladder".[95–102] Although it is indeed possible to obtain results of the quality of highly correlated methods based on DFT, all single-determinant methods will fail when MR-CI is required.[103, 104] Those good results, however, are mostly based on fortuitous error cancellation and a good functional choice relies on benchmarking the class of systems under investigation.[104] Despite all the obstacles, great effort was put into the development of local correlation methods that allows for accurate electron and spin density calculations at the *coupled cluster* (*CC*) level. The *domain based local pair natural orbital* (*DLPNO*)-CCSD method allows for the computation of HFCs within an error margin of ±1 MHz for organic radicals and good agreement with experimental values could be obtained for transition metal isotropic HFCs.[105]

The achievements of quantum chemical method development to compute accurate EPR parameters described so far usually rely on studies of static pictures in gas phase. However, the experiments are typically conducted in condensed matter, such as liquids or frozen solutions. Furthermore, the experimentalist is mostly interested in extracting information of the molecular system within its surrounding. Consequently, the next step towards building a stable bridge between theory and experiment is to include environmental effects into the modeling and calculation. Modeling of solvation is challenging but its necessity gave rise to a big research field.[106–110] One approach is based on a continuum solvation model.[108] Here, the solvent is accounted for in an average manner and purely electrostatically, rendering it good enough for a rough estimation. Whenever specific solvent-solute interactions are part of the investigation the inclusion of solvent molecules explicitly becomes indispensable. The difficulty though is to choose the amount of solvent molecules and their cluster conformations towards the solute. Solutions yet imply a dynamical picture due to the constant movements of the molecules in the sample and the weakness of solvent-solute interactions. It can therefore become necessary to make use of *molecular dynamics* (*MD*) to simulate the molecular structure over time.[111, 112] By now, it is even possible to conduct simulations at a quantum mechanical level, known as *ab-initio molecular dynamics* (*AIMD*).[113] In this way the analysis of the simulated trajectories allows to obtain averaged properties including their statistics over the simulated ensemble.[114–116] Since the experimental measurement as well captures an average picture of the dynamics, this statistical approach gives a more realistic representation of the studied system, though computationally significantly more demanding.

One class of molecules that is widely subjected to experimental and theoretical EPR investigation are *nitroxides*. Nitroxides are organic radicals with an unpaired electron being localized at the nitroxy (N-O) group and are stabilized by bulky alkyl groups. They are most commonly used as spin labels in organic chemistry and biochemistry to monitor characteristics of their microenvironment by EPR spectroscopy. As a sole paramagnetic label in a diamagnetic surrounding they provide unique information. Their stability in non-reducing environments at any temperature renders nitroxides one of the most useful EPR probes. In fact, they can be utilized in multiple contexts to help understanding characteristics of materials on a molecular level.[117, 118] Previous studies has applied nitroxides as radical traps[119] or as site specific labels in structural biology[120–122]. Due to the formation of *hydrogen bonds* (*H-bonds*) their aqueous solution is not only facilitated but also makes them perfect candidates for studying local properties of solvation, such as polarity, pH sensitivity or H-bond networks. In addition, the basic structure of nitroxides can be chemically modified to tune its response to the microenvironment.[117, 123–126]

The high sensitivity of nitroxides to their surrounding can be directly extracted from their g- and A-tensor (of the nitroxy nitrogen ^{14}N nucleus), more precisely the g_{xx} and A_{zz} component. While g_{xx} decreases in polar/protic environments A_{zz} increases.[123, 124] The g- and A-tensors, more precisely their principal values g_{xx}, g_{yy}, g_{zz} and A_{xx}, A_{yy}, A_{zz}, can be obtained by simulation of an EPR spectrum based on the phenomenological SH approach to fit the experimental spectrum. While freely tumbling nitroxides in a sample give averaged values, denoted g_{iso} and A_{iso}, frozen solutions result in powder pattern and therefore resolve the anisotropies of the g- and A-tensor. Conventional X-band (9.5 GHz/0.34 T) are mainly influenced by the A-tensor anisotropy, whereas the g-tensor anisotropy dominates at higher frequencies/fields ($\geq$95 GHz/3.4 T). In particular, the g_{xx} region is rich in information. For example, discrete g_{xx} values due to multiple spectral components in the EPR spectrum could be assigned to specific H-bond situations in previous studies.[125, 127, 128] Furthermore, it was shown that the fraction of such resolved spectral components strongly depend on the thermal history of the frozen solution.[129]

Besides the peak positions in the EPR spectrum the *linewidth* (or line broadening) associated to the peaks as well provide information of the system under investigation. The *apparent linewidth* (*ALW*) as depicted by the measured spectrum consists of different components.[130] The first one is related to the relaxation time of electron spin and commonly referred to as intrinsic linewidth. For nitroxides in frozen solution the intrinsic linewidth amounts to <1 MHz.[131] The second one is denoted *field independent linewidth* that results from small unresolved HFCs from the solute itself or also from the magnetic nuclei of the solvent, e.g., solvent protons. The last one is the *field dependent linewidth*. The term already indicates that this linewidth component changes with measuring frequency/field. The consensus exists that the micro-heterogeneity of the molecular ensemble in frozen solutions leads to slightly different g-values for each single molecule in the sample due to different microenvironments. These differences split further apart with increasing spectrometer frequency and result in a distribution of g-values. This phenomenon is referred to as *g-strain*[132] and this increase of linewidth is believed to be linear.[132–134] By increasing the measuring frequency further possibly enables the resolution of subensembles of the solute in discrete resonances, with each subensemble characterized by its own g-strain. For nitroxides the field dependent linewidth was assigned to g-tensor variations via site-to-site variations of the local environment[128] and nitroxide structure[135]. Furthermore, experimentally observed variations of g_{xx} values on the order of 500 ppm were assigned to a varying number of H-bonds that led to a heterogeneous g_{xx} region.[124, 125, 128] However, an in-depth analysis of the molecular origin of the g-strain is missing so far. While multifrequency EPR experiments are known for linewidth studies, further insight on the molecular level most likely needs support by computational spectroscopy.

This thesis encompasses three parts. First, the theoretical foundations are provided on which die following parts are built. Besides an overview of different electronic structure methods the molecular properties within the linear response framework are discussed. Furthermore, the investigated EPR parameters, namely g- and A-tensor, are given in this context. The second part comprises the projects related to method development. Analytical second derivatives for *resolution of the identity* (*RI*)-MP2 and DHDFT in the open shell framework were derived, implemented and applied to the calculation of g-tensors using GIAOs. In addition, analytical second derivatives for *orbital optimized MP2* (*OO-MP2*) were derived and the concept of its preliminary implementation is presented. All developed methods described in this part were implemented in the quantum chemical ORCA program package.[136–138] The third part of this thesis deals with the application of quantum chemistry to investigate solvation effects on EPR properties of a nitroxide in aqueous solution. This project was conducted in collaboration with experimentalists and theoreticians of different field of expertise. In this joint work the accurate calculation of HFCs in solution is presented by pushing the limits of state-of-the-art computational methodologies. This was subsequently extended to the prediction of the full EPR spectrum of the nitroxide and finally to the investigation of the molecular origin of the g_{xx} heterogeneity and g-strain as observed in the multifrequency EPR experiments. Finally, an overall conclusion of work presented in this thesis with an outlook of future perspectives is provided.

Part I

Theoretical background

2 Electronic structure methods

The starting point in most quantum chemical problems is the solution of the (time-independent) electronic *Schrödinger equation* (*SE*) [139]

$$\hat{\mathcal{H}}\Psi_n = \mathcal{E}_n\Psi_n \tag{2.1}$$

with $\hat{\mathcal{H}}$ being the Hamilton operator, $\mathcal{E}_n$ the corresponding eigenvalue that is the total energy of the system's state n described by the electronic wave function Ψ_n. Its solution renders access to the electronic structures of atoms and molecules and subsequently their properties. Since the SE is only exactly solvable for the hydrogen atom, approximation methods are required for many-electron systems. For each quantum chemical problem a suitable model needs to be found that can be described by mathematical formulas considering the underlying physics correctly. In this section we will give an overview of the common methods in electronic structure theory that paves the way for the quantum chemical description of molecular properties.

2.1 Notations and definitions

Throughout this thesis i, j, k denote the occupied MOs, a, b, c the virtual MOs and p, q, r any MOs if not mentioned otherwise; with the overline variant corresponding to the other spin case.[1] The *atomic orbitals* (*AOs*) are given by $\chi, \mu, \nu, \ldots$ and the two-electron integrals are written in the Mulliken notation $(1^*1|2^*2)$. The superscript x refers to the total derivative with respect to the perturbation x whereas the superscript (x) refers to solely the basis function and operator derivatives if dependent on the perturbation, not the MO coefficients. The perturbations here are either the electric field F or magnetic field B. Note that the field derivative has to be taken for each component (x, y, z) of the electric/magnetic field.

---

[1] This also holds for their use as subscripts.

2.2 Hartree-Fock theory

A first approach to mathematically describe an N-particle system is to consider it as a system which can approximately be characterized by N statistically independent particles. As follows, the wave function can be written as a product of the single-particle wave functions. For the electronic SE, N indistinguishable electrons have to be considered. Electrons are fundamental particles belonging to the group of fermions. According to *Pauli's principle*, fermions possess the property of being anti-symmetric in terms of permutation. Therefore, a physically correct description of an N-electron system can be achieved by a Slater determinant, which takes account of anti-symmetry. In HF theory the quantum mechanical system is depicted by *one* Slater determinant made of N single-particle wave functions [140, 141]

$$
\begin{aligned}
\Psi &= \Phi\left[\phi_1(1)\phi_2(2)\ldots\phi_N(N)\right] \\
&= \frac{1}{\sqrt{N!}}\begin{vmatrix} \phi_1(1) & \phi_2(1) & \ldots & \phi_N(1) \\ \phi_1(2) & \phi_2(2) & \ldots & \phi_N(2) \\ \vdots & \vdots & \ddots & \vdots \\ \phi_1(N) & \phi_2(N) & \ldots & \phi_N(N) \end{vmatrix} = \frac{1}{\sqrt{N!}}\begin{vmatrix} \phi_1 & \phi_2 & \ldots & \phi_N \end{vmatrix} .
\end{aligned}
\tag{2.2}
$$

The single-particle wave functions of electrons in a molecule are chosen to be MOs. Note that the MOs of an electron consist of a spatial and spin part. If not further notified, by using MO we only refer to the spatial orbitals.

The electronic ground state energy $\mathcal{E}_0$ of the system is obtained by calculating the expectation value of the electronic SE with a Slater determinant (2.2) as wave function

$$
\mathcal{E}_0 = \left\langle \Phi_0 \,\middle|\, \hat{\mathcal{H}} \,\middle|\, \Phi_0 \right\rangle , \tag{2.3}
$$

where the Φ_0 is the normalized ground state Slater determinant. The electronic Hamiltonian $\hat{\mathcal{H}}$ can be split into a one-particle operator part, which is the kinetic energy operator and attraction between nuclei and electrons together defined as $\hat{h}$, and a two-particle operator part, which is the electron repulsion,

$$
\hat{\mathcal{H}} \equiv \hat{H}_{el} = \underbrace{\hat{T}_{el} + \hat{V}_{nuc,el}}_{\hat{h}} + \underbrace{\hat{V}_{el}}_{\frac{1}{r_{12}}} . \tag{2.4}
$$

By applying Slater-Condon rules[142, 143], equation (2.3) will become

$$
\begin{aligned}
E_{HF}\left[\{\phi_i\}\right] = \sum_{i}^{N} \left\langle \phi_i \middle| \hat{h} \middle| \phi_i \right\rangle + \frac{1}{2}\sum_{i,j}^{N} \Bigg(&\left\langle \phi_i(1)\phi_j(2) \middle| \frac{1}{r_{12}} \middle| \phi_i(1)\phi_j(2) \right\rangle \\
- &\left\langle \phi_i(1)\phi_j(2) \middle| \frac{1}{r_{12}} \middle| \phi_i(2)\phi_j(1) \right\rangle \Bigg) .
\end{aligned}
\tag{2.5}
$$

The HF ground state energy is a functional of the MOs. Since the MOs are orthonormalized, for the one-particle term only those integrals over the same orbitals survive, whereas for the two-particle term one permutation is allowed for the integrals not to vanish, hence a double sum remains.

The task now is to optimize the MOs so that the HF ground state energy is minimized. To assure that the MOs remain orthonormalized during the optimization a Lagrange parameter λ_{ij} is added

$$
\tau\left[\{\phi_i\}\right] = E_{HF}\left[\{\phi_i\}\right] + \sum_{i,j}^{N} \lambda_{ij}\left(\delta_{ij} - \langle \phi_i \,|\, \phi_j \rangle\right) . \tag{2.6}
$$

Applying the variational principle to expression (2.6) an upper limit of the exact ground state energy can be determined by taking the derivative with respect to ϕ_i^*, ϕ_i and λ_{ij} and setting it zero. After unitary transformation the HF equations are obtained

$$
\underbrace{\left\{ \hat{h}_i + \sum_{j=1} \int \phi_j^*(2) \frac{1-\hat{P}_{12}}{r_{12}} \phi_j(2) d2 \right\}}_{\hat{F}_i} \phi_i(1) = \epsilon_i \phi_i(1), \tag{2.7}
$$

$$
\hat{F}_i = \hat{h}_i + \sum_j \left(\hat{J}_{ij} - \hat{K}_{ij}\right) , \tag{2.8}
$$

$$
\epsilon_i = h_i + \sum_j \left(J_{ij} - K_{ij}\right) \tag{2.9}
$$

where $\hat{P}_{12}$ is the permutation operator. $\hat{F}_i$ is the Fock operator which gives the orbital energy ϵ_i with $\hat{J}_j$ and $\hat{K}_j$ being the Coulomb and exchange integrals, respectively. The Fock operator is an effective one-electron energy operator describing the kinetic energy of an electron and its attraction to all the nuclei as well as its repulsion with all other electrons. This interaction of one electron with all other electrons regarded as one object is called "mean field approximation". It is important to note that the sum over all Fock orbital energies is *not* the HF ground state energy since the electron-electron interaction is counted twice by the Fock operator. Therefore the HF ground state energy is

$$E_{HF} = \sum_{i}^{N} \epsilon_i - \frac{1}{2} \sum_{i}^{N} \left(J_{ij} - K_{ij} \right) . \tag{2.10}$$

The canonical HF equation (2.7) is solved iteratively by initially guessing a set of MOs to determine the Fock operator which then can be used to optimize the molecular orbitals. Those will be used to create a new Fock operator which is then used in turn to re-optimize the new set of orbitals. This procedure is repeated until the previous and resulting orbitals do not differ anymore, i.e., convergence towards the numerically exact solution is reached, and is known as the *self-consistent field* (*SCF*) method.[144]

2.2.1 The Roothaan-Hall and Pople-Nesbet equations

In practice, implementation of the *Hartree-Fock self-consistent field* (*HF-SCF*) procedure for molecular systems requires a reformulation in terms of expanding the MOs in a *linear combination of atomic orbitals* (*LCAO*). This LCAO-MO procedure, independently developed by C. C. J. Roothaan and G. G. Hall [145, 146], is based on the idea of introducing a set of N_{bas} basis functions $\{\chi\}$ that can be considered as atomic orbitals centered around the atoms of the molecule. Thus, the MO $\phi_i(r)$ can be written as the linear combination of these basis functions

$$\phi_i(r) = \sum^{N_{bas}} c_{\chi i} \chi \tag{2.11}$$

with $c_{\chi i}$ being the unknown MO coefficients. Substituting the expansion of equation 2.11 into equation 2.7 and some further mathematical reformulations result in the "Roothan-Hall" equations that can be written in a single matrix equation

$$\mathbf{Fc} = \boldsymbol{\epsilon}\mathbf{Sc} \tag{2.12}$$

with **F** being the Fock matrix, **S** the overlap matrix, **c** the $N_{bas} \times N_{bas}$ MO coefficient matrix and $\boldsymbol{\epsilon}$ the $N_{bas} \times N_{bas}$ diagonal matrix of the orbital energies ϵ_i. Thus, the problem of calculating the wave function has been transformed to one of computing the MO coefficients. The overlap matrix results from the non-orthonormality of the basis functions and its elements are defined as

$$S_{\mu\nu} = \int \mu^*(1)\nu(1)d1. \tag{2.13}$$

The MO coefficients define the electron density matrix **P** with its elements being

$$P_{\mu\nu} = n_{occ} \sum_i c^*_{\mu i} c_{\nu i} \tag{2.14}$$

where n_{occ} is the occupation number of MO i. The Roothaan-Hall equations are formulated for closed-shell *restricted Hartree-Fock* (*RHF*) systems, i.e., all MOs are doubly occupied ($n_{occ} = 2$). In case of molecular systems having unpaired electrons, i.e., open-shell systems, the UHF formulation is required. This generalization of the Roothaan-Hall equations are known as the "Pople-Nesbet" equations.[147] Here, two sets of MO coefficients, one for the α electrons and one for the β electrons, need to be optimized. These two sets of coefficients are solutions to two coupled matrix eigenvalue problems

$$\mathbf{F}^\alpha \mathbf{c}^\alpha = \boldsymbol{\epsilon}^\alpha \mathbf{S} \mathbf{c}^\alpha, \tag{2.15}$$
$$\mathbf{F}^\beta \mathbf{c}^\beta = \boldsymbol{\epsilon}^\beta \mathbf{S} \mathbf{c}^\beta. \tag{2.16}$$

The density matrix elements for the respective spin case are then defined as

$$P^\sigma_{\mu\nu} = \sum_i^{i \in N^\sigma} c^{\sigma *}_{\mu i} c^\sigma_{\nu i} \qquad \sigma \in \{\alpha, \beta\}. \tag{2.17}$$

The (total) electron density is the sum of the α- and β-density

$$\mathbf{P}^{tot} = \mathbf{P}^\alpha + \mathbf{P}^\beta \tag{2.18}$$

while the difference between the α- and β-density is known as the spin density

$$\mathbf{P}^{spin} = \mathbf{P}^\alpha - \mathbf{P}^\beta. \tag{2.19}$$

2.3 Correlation methods

The wave functions constructed according to HF theory can account for $\sim$ 99% of the total energy provided a sufficiently large basis set is used. Nevertheless, problems in chemistry do not deal with total energies but rather with relative energies. Thus, the remaining $\sim$ 1% can become essential for the description of chemical phenomena, so that the approximations introduced by HF theory can cause severe deviations. This energy difference between the exact and HF energy is known as "electron correlation"

$$E^{corr} = E^{exact} - E^{HF}. \tag{2.20}$$

There are two (main) sources of error in the HF ansatz which lead to this discrepancy. The first one is related to the mean-field approximation which neglects the instantaneous interaction of the electrons with one another. Since this refers to the electrons' dynamic it is known as "dynamic correlation". The second one is related to the single Slater determinant approach by the HF ansatz, which is a rather poor description of a many-electron system. In certain cases, the system can only be properly described by a linear combination of multiple (nearly-) degenerate Slater determinants. The missing component due to this inaccurate description is known as "static correlation". Note, that it is rather impossible to separate both types of correlation since they originate from the same physics, but one can say that perturbation theory primarily recovers dynamic correlation whereas multi-configurational approaches primarily accounts for static correlation. In the following, different "post-HF" approaches which take into account electron correlation will be shortly depicted. [148–150]

2.3.1 Møller-Plesset-perturbation theory

One approach to include electron correlation is based on *perturbation theory* (*PT*), more specifically *Rayleigh Schrödinger perturbation theory* (*RSPT*). The key idea in PT is to split the Hamiltonian into an unperturbed (0^{th} order) part $\hat{H}_0$ and a contribution from a perturbation $\hat{V}$

$$\hat{\mathcal{H}} = \hat{H}_0 + \lambda \hat{V} \tag{2.21}$$

with λ being a dimensionless ordering parameter. Equation 2.1 then becomes

$$\hat{\mathcal{H}}\Psi_n = \left(\hat{H}_0 + \lambda\hat{V}\right)\Psi_n = \mathcal{E}_n\Psi_n. \tag{2.22}$$

The unperturbed Hamiltonian is usually chosen such that the eigenfunctions and eigensolutions are known as given by the 0^{th} order wave function

$$\hat{H}_0\Psi_n^{(0)} = E_n^{(0)}\Psi_n^{(0)}. \tag{2.23}$$

If the perturbation $\hat{V}$ is fairly small, $\Psi_n^{(0)}$ and $E_n^{(0)}$ are expected to be reasonably close to the exact solutions Ψ_n and $\mathcal{E}_n$. By expanding the exact solutions in a Taylor series expression higher order corrections to the 0^{th} order energy and wave function can be obtained.[2]

The idea by C. Møller and M. S. Plesset was to choose the unperturbed Hamiltonian to be the Fock operator, hence the perturbation to be the correction of the electron-electron interaction double-counting [152]

$$\hat{H}_0 = \hat{F} = \sum_i \hat{f}_i, \tag{2.24}$$

$$\hat{V} = \sum_i \sum_{i<j} \frac{1}{r_{ij}} - \sum_i \sum_j \left(\hat{J}_{ij} - \hat{K}_{ij}\right). \tag{2.25}$$

This application of RSPT is therefore often referred to as *Møller-Plesset perturbation theory* (*MPPT*), most commonly known by its form of second order correction, MP2. The 0^{th} order wave function then is the HF wave function of which the eigenvalues are known.

However, the general formulation of perturbation theory does not provide variational energies. Instead using the Lagrange method of undetermined multipliers to reformulate the MP2 energy expression does.[153, 154] The starting point is therefore the Hylleraas MP2 functional which has the following form for the unrestricted case using the RI formulation

---

[2] For a detailed derivation the reader is referred to common textbook literature [144, 148, 149, 151].

$$\begin{aligned}\mathcal{J}_2\left[t\right] = \sum_{ijab,P} \Bigg\{ & \frac{1}{4}\left[B^P_{ia}B^P_{jb} - B^P_{ib}B^P_{ja}\right] t^{ij}_{ab} + \frac{1}{4}\left[B^P_{ai}B^P_{bj} - B^P_{aj}B^P_{bi}\right] t^{ij*}_{ab} \\ & + \frac{1}{4}\left[B^P_{\overline{ia}}B^P_{\overline{jb}} - B^P_{\overline{ib}}B^P_{\overline{ja}}\right] t^{\overline{ij}}_{\overline{ab}} + \frac{1}{4}\left[B^P_{\overline{ai}}B^P_{\overline{bj}} - B^P_{\overline{aj}}B^P_{\overline{bi}}\right] t^{\overline{ij}*}_{\overline{ab}} \\ & + B^P_{\overline{ia}}B^P_{jb}t^{\bar{i}j}_{\bar{a}b} + B^P_{\overline{ai}}B^P_{bj}t^{\bar{i}j*}_{\bar{a}b} \Bigg\} + \left\langle \mathbf{D'}^{\dagger}\mathbf{F} \right\rangle + \left\langle \overline{\mathbf{D'}}^{\dagger}\overline{\mathbf{F}} \right\rangle \end{aligned} \tag{2.26}$$

with t being the MP2 amplitudes and $\mathbf{D}'$ the unrelaxed MP2 density. The overline denotes the opposite spin case. The unrestricted formulation distinguishes between three cases: $\alpha\alpha$, $\beta\beta$ and $\alpha\beta = \beta\alpha$. The pointy brackets imply the trace of the resulting matrix. The three-index RI integrals are[155–157]

$$\sum_P B^P_{pr}B^P_{qs} = \sum_{PQ} (pr|Q) \left(V^{-1}\right)_{PQ} (Q|qs)\,, \tag{2.27}$$

$$V_{PQ} = (P|Q)\,, \tag{2.28}$$

$$B^P_{pq} = \sum_Q (pq|Q) \left(V^{-\frac{1}{2}}\right)_{QP}, \tag{2.29}$$

where P, Q denote the auxiliary basis functions. Optimizing the Hylleraas functional with respect to the three sets of amplitudes gives us three equations for the residuals:

$$\frac{\partial \mathcal{J}_2}{\partial t^{ij}_{ab}} = R^{ij}_{ab} = \left\{ \left(B^P_{ai}B^P_{bj} - B^P_{aj}B^P_{bi}\right) - \sum_k \left[t^{ik}_{ab}F_{kj} + t^{kj}_{ab}F_{ki}\right] + \sum_c \left[t^{ij}_{ac}F_{cb} + t^{ij}_{cb}F_{ca}\right] \right\}, \tag{2.30}$$

$$\frac{\partial \mathcal{J}_2}{\partial t^{\overline{ij}}_{\overline{ab}}} = R^{\overline{ij}}_{\overline{ab}} = \left\{ \left(B^P_{\overline{ai}}B^P_{\overline{bj}} - B^P_{\overline{aj}}B^P_{\overline{bi}}\right) - \sum_k \left[t^{\overline{ik}}_{\overline{ab}}F_{\overline{kj}} + t^{\overline{kj}}_{\overline{ab}}F_{\overline{ki}}\right] + \sum_c \left[t^{\overline{ij}}_{\overline{ac}}F_{\overline{cb}} + t^{\overline{ij}}_{\overline{cb}}F_{\overline{ca}}\right] \right\}, \tag{2.31}$$

$$\frac{\partial \mathcal{J}_2}{\partial t^{\bar{i}j}_{\bar{a}b}} = R^{\bar{i}j}_{\bar{a}b} = \left\{ B^P_{\overline{ai}}B^P_{bj} - \sum_k \left[t^{\bar{i}k}_{\bar{a}b}F_{kj} + t^{\bar{k}j}_{\bar{a}b}F_{\overline{ki}}\right] + \sum_c \left[t^{\bar{i}j}_{\bar{a}c}F_{cb} + t^{\bar{i}j}_{\bar{c}b}F_{\overline{ca}}\right] \right\}. \tag{2.32}$$

The amplitudes are then obtained by setting the residual to 0 and rearranging, given here for the same spin and opposite spin cases

$$\text{same spin:} \qquad t_{ab}^{ij} = \frac{B_{ai}^{P} B_{bj}^{P} - B_{aj}^{P} B_{bi}^{P}}{\epsilon_i + \epsilon_j - \epsilon_a - \epsilon_b}, \tag{2.33}$$

$$\text{opposite spin:} \qquad t_{\bar{a}b}^{\bar{i}j} = \frac{B_{\overline{ai}}^{P} B_{bj}^{P}}{\epsilon_{\bar{i}} + \epsilon_j - \epsilon_{\bar{a}} - \epsilon_b}. \tag{2.34}$$

The MP2-correction energy with the optimized amplitudes then is

$$E^{MP2corr} = \frac{1}{4} \sum_{ijab} (ia||jb)\, t_{ab}^{ij} = \frac{1}{4} \sum_{ijab} \frac{|(ia||jb)|^2}{\epsilon_i + \epsilon_j - \epsilon_a - \epsilon_b}. \tag{2.35}$$

The occupied/virtual part of unrelaxed density are defined as

$$D'_{ij} = -\sum_{k} \left[\frac{1}{2} \left\langle \mathbf{T}^{jk*} \mathbf{T}^{ki} \right\rangle + \left\langle \mathbf{T}^{j\bar{k}*} \mathbf{T}^{\bar{k}i} \right\rangle \right], \tag{2.36}$$

$$D'_{ab} = \sum_{ij} \left[\frac{1}{2} \mathbf{T}^{ji*} \mathbf{T}^{ij} + \mathbf{T}^{j\bar{i}*} \mathbf{T}^{\bar{i}j} \right]_{ab}, \tag{2.37}$$

with **T** being the amplitude matrices for the given occupied MO indices.
Often the unrelaxed density is not sufficient, e.g., for molecular properties. Therefore, the relaxed density is required, i.e., allowing the mixing between the occupied and virtual space. This is achieved by adding the Brillouin condition to the formulation of the Lagrangian[158, 159]

$$\mathcal{L} = \mathcal{J}_2 + \sum_{ia} Z_{ai} F_{ai} + \sum_{\overline{ia}} Z_{\overline{ai}} F_{\overline{ai}}. \tag{2.38}$$

Solving the resulting Z-vector equation[160] which is given here for the α-case

$$\begin{aligned} &\sum_{ia} Z_{ai} \left[\left(\epsilon_b - \epsilon_j \right) \delta_{ab} \delta_{ij} + (ai||jb) + (ai||bj) \right] \\ &= -2 \left\{ \sum_{aP} B_{ba}^{P} \left(\overset{ssP}{\Gamma}_{ja} + \overset{osP}{\Gamma}_{ja} \right) - \sum_{iP} B_{ij}^{P} \left(\overset{ssP}{\Gamma}_{ib} + \overset{osP}{\Gamma}_{ib} \right) + \frac{1}{2} \mathcal{R} \left[\mathbf{D}' \right]_{bj} \right\} \end{aligned} \tag{2.39}$$

by making the Lagrangian stationary with respect to orbital rotations provides the relaxed density by filling the occupied-virtual/virtual-occupied part of the density matrix according to [161–163]

$$D_{ai} = -\frac{1}{2} Z_{ia} = D_{ia}. \tag{2.40}$$

The three-index density matrix and the Fock response operator which occur in equation 2.39 are defined as[163, 164]

$$\text{same spin:} \quad \overset{ssP}{\Gamma}_{ia} = \sum_{jb} t^{ij}_{ab} B^{P}_{jb}, \tag{2.41}$$

$$\text{opposite spin:} \quad \overset{osP}{\Gamma}_{ia} = \sum_{\bar{j}\bar{b}} t^{i\bar{j}}_{a\bar{b}} B^{P}_{\bar{j}\bar{b}}, \tag{2.42}$$

$$\mathcal{R}\left[\mathbf{D}\right]_{rs} = 2\left[\sum_{pq} D_{pq}\left(pq||rs\right) + \sum_{\overline{pq}} \left(\overline{pq}|rs\right) + \mathcal{R}^{XC}\right]. \tag{2.43}$$

The (antisymmetrized) two-electron integrals can be approximated using RIJK[165] or RIJCOSX[166]. The contribution $\mathcal{R}^{XC}$ arising from the *exchange correlation* (*XC*) functional is given and discussed in reference [167]. The β-case is defined analogously.

2.3.2 Orbital-optimized Møller-Plesset-perturbation theory

The MP2 correlation energy as obtained in 2.3.1 can be considered stationary with respect to the MP2 amplitudes since the Hylleraas functional was minimized with respect to those. However, it is not stationary with respect to the MOs, thus no orbital relaxation is accounted for the additional electron correlation field. An approach to reformulate the MP2 functional that takes into account orbital relaxation is known as OO-MP2.[168–173] The idea is to start with a reformulation of the Hylleraas functional and make this stationary with respect to both MP2 amplitudes and MOs coefficients. The general OO-MP2 Hylleraas functional applying the RI formulation is

$$\begin{aligned}\mathcal{L}^{RI}\left[t,\kappa\right] = &\sum_{i} h_{ii} + \frac{1}{2}\sum_{ij}\left(ii||jj\right) + \sum_{iaP}\left(ia|P\right)\Gamma^{P}_{ia} \\ &+ \sum_{ij} D_{ij}F_{ij} + \sum_{ab} D_{ab}F_{ab}\end{aligned} \tag{2.44}$$

with

$$\Gamma_{ia}^{P} = \sum_{Q} V_{PQ}^{-1} \sum_{jb} (Q|jb)\, t_{ab}^{ij}. \tag{2.45}$$

While the amplitudes are obtained as for MP2 by making equation 2.44 stationary with respect to t, accounting for orbital relaxation requires a parameterization of the MOs by means of an anti-hermitian orbital rotation matrix $\boldsymbol{\kappa}$

$$c^{new} = c^{old} \exp(\boldsymbol{\kappa}) \qquad \text{with} \qquad \boldsymbol{\kappa} = \begin{pmatrix} 0 & \kappa_{ia} \\ -\kappa_{ia} & 0 \end{pmatrix} \tag{2.46}$$

such that the orbital changes to second order are

$$\exp(\kappa)\,|i\rangle = |i\rangle + \sum_{a} \kappa_{ai}\,|a\rangle - \frac{1}{2} \sum_{jb} \kappa_{bi}\kappa_{bj}\,|j\rangle + \ldots, \tag{2.47}$$

$$\exp(\kappa)\,|a\rangle = |a\rangle - \sum_{i} \kappa_{ai}\,|i\rangle - \frac{1}{2} \sum_{jb} \kappa_{aj}\kappa_{bj}\,|b\rangle + \ldots. \tag{2.48}$$

Applying this parameterization on equation 2.44 and taking the derivative with respect to κ_{ai} results in the orbital gradient or OO-MP2 Lagrangian

$$\begin{aligned} \frac{\partial \mathcal{L}_{OO}[t,\kappa]}{\partial \kappa_{ai}} \equiv g_{ai} = {} & 2F_{ai} + 2\sum_{cP} (ac|P)\Gamma_{ic}^{P} - 2\sum_{kP} (ik|P)\Gamma_{ka}^{P} \\ & + 2\sum_{j} D_{ij}F_{aj} - 2\sum_{b} D_{ab}F_{ib} + \mathcal{R}\,[D]_{ai}\,. \end{aligned} \tag{2.49}$$

The optimized MOs that account for electron correlation are obtained if $g_{ai} \overset{!}{=} 0$. The OO-MP2 density is then defined as

$$D^{OO} = P^{ref} + D^{MP2} \tag{2.50}$$

$$\text{with} \qquad P_{\mu\nu}^{ref} = \sum_{i} c_{\mu i} c_{\nu i}, \tag{2.51}$$

where P^{ref} consists of the orbital-optimized coefficients and D^{MP2} is the (unrelaxed)

MP2-like density as defined in equations 2.36 and 2.37. Note that D^{OO} is a relaxed density since it is made stationary with respect to orbital rotations.

2.3.3 Coupled cluster theory

An elegant theory that includes electron correlation is CC theory.[174–177] The central tenet is the description of the exact (within the basis set approximation) wave function as

$$\Psi = \Psi^{CC} = \exp\left(\hat{T}\right)\Phi_0 \tag{2.52}$$

with Φ_0 being the reference wave function, usually chosen as the ground state HF wave function, and $\hat{T}$ being an excitation operator that is defined as

$$\hat{T} = \hat{T}_1 + \hat{T}_2 + \hat{T}_3 + \cdots + \hat{T}_{N_{el}}. \tag{2.53}$$

The $\hat{T}_i$ operators generate all i^{th} excited Slater determinants upon acting on Φ_0, e.g.

$$\hat{T}_1\Phi_0 = \sum_i \sum_a t_i^a \Phi_i^a, \qquad \textit{single excitation } (S) \tag{2.54}$$

$$\hat{T}_2\Phi_0 = \sum_{ij} \sum_{ab} t_{ij}^{ab} \Phi_{ij}^{ab}, \qquad \textit{double excitation } (D) \tag{2.55}$$

where the expansion coefficients t are referred to as CC amplitudes. The exponential excitation operator can be expanded in a Taylor series

$$\exp\left(\hat{T}\right) = \sum_{k=0}^{\infty} \frac{1}{k!}\hat{T}^k = 1 + \hat{T}_1 + \left(\hat{T}_2 + \frac{1}{2}\hat{T}_1^2\right) + \left(\hat{T}_3 + \hat{T}_2\hat{T}_1 + \frac{1}{6}\hat{T}_1^3\right) + \ldots, \tag{2.56}$$

where the first term generates the HF reference wave function Φ_0, the second term all single excitations, the third term all double excitations and so forth. Since a variational treatment of the CC wave function leads to non-vanishing terms up to the order of N_{el}, standard CC theory proceeds by projecting the SE onto the reference wave function Φ_0^* that leads to the expectation value

$$E^{CC} = \left\langle \Phi_0 \,\middle|\, \hat{H} \exp\left(\hat{T}\right) \,\middle|\, \Phi_0 \right\rangle . \tag{2.57}$$

To obtain the expectation value the CC wave function needs to be calculated, for which the CC amplitudes have to be determined. Equations for those are obtained by similarity transformation of the Hamiltonian and multiplying the similarity transformed SE with an excited state

$$\begin{aligned} \left\langle \Phi_i^a \,\middle|\, \exp\left(-\hat{T}\right) \hat{H} \exp\left(\hat{T}\right) \,\middle|\, \Phi_0 \right\rangle &= 0, \\ \left\langle \Phi_{ij}^{ab} \,\middle|\, \exp\left(-\hat{T}\right) \hat{H} \exp\left(\hat{T}\right) \,\middle|\, \Phi_0 \right\rangle &= 0, \\ &\vdots \end{aligned} \tag{2.58}$$

In case that all operators up to $\hat{T}_{N_{el}}$ are included, all possible excited determinants are generated, hence rendering the CC wave function to be equivalent to *full configuration interaction* (*FCI*) [3]. Clearly, this is not feasible except for the smallest systems. CC is commonly applied in its truncated forms, i.e., including only certain $\hat{T}_i$ operators, for instance

- CCD: $\hat{T} = \hat{T}_2$,
- CCSD: $\hat{T} = \hat{T}_1 + \hat{T}_2$,
- CCSDT: $\hat{T} = \hat{T}_1 + \hat{T}_2 + \hat{T}_3$.

While *coupled cluster doubles* (*CCD*) and CCSD show a scaling behavior of $\mathcal{O}(N_{el}^6)$, including the excitations originating from $\hat{T}_3$ to obtain *coupled cluster singles doubles triples* (*CCSDT*) increases the scaling behavior massively to $\mathcal{O}(N_{el}^8)$, rendering this version of CC computationally barely feasible. By including the effects of the $\hat{T}_3$ excitation by means of perturbation theory, known as *coupled cluster singles doubles and perturbative triples* (*CCSD*(*T*))[178], a much more effective method with scaling behavior of $\mathcal{O}(N_{el}^7)$ was developed, hitherto renowned as the "gold standard" of single reference methods.[148, 149]

---

[3] FCI is considered the exact wave function within the basis set approximation.

2.3.4 Domain based local pair natural orbital approach

In recent times, enormous progress has been made within the electronic structure method development community to render highly accurate correlation methods, such as CC, accessible to larger molecular systems. The short-range character of dynamic correlation, that accounts for the majority of the correlation energy in single-reference systems, is exploited and the steep computational scaling behavior is avoided by using localized orbitals. Pioneering work has been achieved in this large field by Pulay and co-workers, who has introduced the concept of "correlation domains".[158, 179–181] This method is based on generating the virtual orbital space by projecting the occupied orbital space out of the atomic orbitals. Since the occupied space has first been transformed to a local orbital basis, the projected virtual space spanned by *pair atomic orbitals* (*PAOs*) remains local as well and, hence, can be assigned to correlation domains. While each occupied orbital is assigned a correlation domain, the union of these domains are used to describe higher excitations. Despite the optimization and efficient implementation of the PAO-methodology[182–185], PAO-based correlated wave functions are not suitable for chemical accuracy, which is in the order of $1\,\mathrm{kcal\,mol^{-1}}$.[186] An alternative approach in local correlation methods is based on using *pair natural orbitals* (*PNOs*) instead to span the virtual space. The PNO scheme was initially applied by Meyer and co-workers to study small molecules with great success[187–190], whereas its utilization in local correlation approaches were pioneered by Neese and co-workers.[191, 192] By means of the DLPNO approach, a linear scaling ($\mathcal{O}(N_{el})$) variant of CCSD, named DLPNO-CCSD, for closed shell systems was implemented.[193] Further developments using the DLPNO scheme include DLPNO-CCSD(T)[194, 195], extension to open-shell systems[105] and molecular properties[196–198]. The key concept that enabled reduced-scaling of the methods is the sparse representation of tensors, a data object within the implementation of the algorithms.[186, 193, 199, 200]

2.4 Density functional theory

DFT has become one of the most popular methods in computational chemistry. The foundation is given by the Hohenberg-Kohn theorems[201]:

1. The ground state energy and all other ground state properties are uniquely defined by the electron density. ("Hohenberg-Kohn existence theorem")

2. For a trial density function $\rho'(r)$ the energy functional $E_0\left[\rho'\right]$ cannot be less than

the true ground state energy. ("Hohenberg-Kohn variational theorem")

The advantage of DFT compared to wave function theory is that the density is a function of only 3 spatial coordinates for a given spin and independent of N_{el}, whereas the wave function contains $4N_{el}$ variables. The energy as a functional of the density can then be written as

$$E\left[\rho\right] = T\left[\rho\right] + V_{ee}\left[\rho\right] + V_{ext}\left[\rho\right] \tag{2.59}$$

with $T\left[\rho\right]$ corresponding to the kinetic energy, $V_{ee}\left[\rho\right]$ to the electron-electron potential and $V_{ext}\left[\rho\right]$ to an external potential that is the known nuclei-electron attraction $\left(V_{ne}\left[\rho\right]\right)$ for molecules in the absence of other external potentials. $V_{ee}\left[\rho\right]$ again is the sum of the classical Coulomb repulsion $J\left[\rho\right]$ and the exchange interaction $K\left[\rho\right]$, the latter being of quantum mechanical origin. While $V_{ne}\left[\rho\right]$ and $J\left[\rho\right]$ are given by their classical expressions, the exact form of neither $T\left[\rho\right]$ nor $K\left[\rho\right]$ is known. A pivotal moment within the development of DFT for molecules was the reintroduction of orbitals by W. Kohn and L. J. Sham.[202] The starting point is to consider a fictitious system of N_{el} non-interacting (ni) electrons that has the same ground-state density as the real system of interacting electrons. By calculating the kinetic energy under the assumption of non-interacting electrons the DFT energy can then be written as

$$E\left[\rho\right] = T_{ni}\left[\rho\right] + J\left[\rho\right] + V_{ne}\left[\rho\right] + E_{XC}\left[\rho\right] \tag{2.60}$$

where the XC energy is given by

$$E_{XC}\left[\rho\right] = \left(T\left[\rho\right] - T_{ni}\left[\rho\right]\right) + \left(V_{ee}\left[\rho\right] - J\left[\rho\right]\right). \tag{2.61}$$

In an non-interacting system the one-electron *Kohn-Sham* (KS) orbitals are eigenfunctions to the one-electron KS Hamiltonians

$$\hat{h}_i^{KS}\phi_i^{KS} = \epsilon_i^{KS}\phi_i^{KS} \tag{2.62}$$

where the one-electron KS operator is defined as

$$\hat{h}_i^{KS} = -\frac{1}{2}\nabla_i^2 - \sum_k^{N_{nuc}} \frac{Z_k}{|r_i - R_k|} + \int \frac{\rho(r')}{|r_i - r'|} dr' + v_{XC}. \tag{2.63}$$

The exchange-correlation potential is the derivative of the exchange-correlation energy functional

$$v_{XC} = \frac{\partial E_{XC}\left[\rho\right]}{\partial \rho}. \tag{2.64}$$

The Kohn-Sham equations 2.62 are solved self-consistently similarly to the HF equations.[148, 149, 203]

One key task in DFT is to derive approximations to the XC energy functional. The existing approaches to construct these density functionals are categorized by Perdews's "Jacob's ladder" analogy.[68] The initial developments were derived from the uniform-electron-gas model, known as LDA, with the only variable being the electron density. This description is however not suitable for inhomogeneous systems. The next level of functionals, named GGA, includes a gradient correction of the density and therefore allows for more flexibility. The extension of GGA, called *meta-generalized gradient approximation* (*mGGA*), adds the second density derivative or the kinetic energy to the description of the XC functional. The next level of density functionals furthermore substitutes a fraction of the density functional exchange with exact Hartree-Fock exchange, known as hybrid functionals. One of the most popular hybrid functionals is B3LYP[204, 205] that contains 20 % HF exchange. The highest rung of density functionals belong to *spin-component scaled double-hybrid density functional theory* (*DSD-DFT*)[206–208].

The general expression for DSD-DFT is

$$\begin{aligned} E^{DSD-DFT} &= \underbrace{T_S + J + E_{ne} + c_X E_X^{HF} + (1 - c_X) E_X^{DFT} + c_C E_C^{DFT}}_{E^{SCF}} \\ &+ \underbrace{c_O E_O^{MP2} + c_S E_S^{MP2}}_{E^{MP2}} + s_6 E_D \end{aligned} \tag{2.65}$$

with the terms being, respectively, the kinetic energy, the electron-electron and electron-nuclear Coulomb energies, the exact (HF) exchange energy, the exchange and correlation contribution of the density functional and the opposite and same spin energy con-

tribution at MP2 level. The last term takes into account the dispersion correction which is inevitable to achieve accurate results.[209–213]
Dependent on the coefficients the previously described different cases may be considered:

- $c_X = c_O = c_S = 0$: "pure" DFT
- $c_X = 1, c_O = c_S = c_C = s_6 = 0$: pure HF
- $c_X = c_O = c_S = 1, c_C = s_6 = 0$: pure MP2
- $c_O = c_S = 1 - c_C, s_6 = 0$: simpler *double-hybrid density functionals* (*DHDFs*), e.g., B2PLYP[73]

3 Molecular properties

In quantum chemistry most insight is obtained by connecting theory to experiment. Clearly, this means going beyond solving the electronic Schrödinger equation and obtaining the electronic energy. Theoretical models and algorithms to compute experimental observables are therefore required.

Quantities of interest for a molecule of a given electronic state can be categorized based on the underlying characteristics of the property. One category of molecular properties considers energy differences, such as reaction energies, dissociation energies or energy differences between different conformers or isomers. This properties are related to different points on the Born-Oppenheimer potential energy surfaces. Another category are properties for a specific electronic state, such as equilibrium structures, dipole moment, polarizabilities, vibrational frequencies or hyperfine interactions. These properties require more information than "just" the energy at a specific point on the potential energy surface. The last category of properties considers transitions between different electronic states such as electronic excitation energies or ionization potentials.

One obvious approach to compute molecular properties is to go via the expectation value formalism for the corresponding operator $\hat{O}$. However, this can lead to ambiguities if no well-defined wave function exists. A more general approach is to consider the property as the response of a molecule to an external perturbation, and thereby the property can be calculated as an energy derivative, hence the name "response theory". Derivatives can be either computed numerically or analytically. For numerical derivatives "only" energy calculations at the presence of the perturbation are required, thus being more straightforward. The accuracy however is limited and the computational costs are high and renders this approach less suitable for large molecules. The advantage of analytical derivatives is the higher accuracy and lower computational costs compared to numerical differentiation. Furthermore, magnetic properties are easier to treat by means of the analytical approach. However, the development of analytical derivatives is usually related to elaborate derivations and complicated implementation techniques. Nevertheless, the benefits outweigh the effort put into enabling analytical derivatives for molecular properties.[148, 149, 214, 215]

In the following, a short overview on the analytical approach to compute molecular properties is given and then a closer look is taken at the computation of EPR parameters within the framework of linear response theory.

3.1 Analytical derivatives

In derivative theory[216] a molecular property can be described as response of the energy of a specific electronic state towards a perturbation x. The starting point here is to expand the energy in a Taylor series

$$E(x) = E(0) + \underbrace{\frac{\partial E}{\partial x} x}_{first\ order} + \underbrace{\frac{\partial^2 E}{\partial x^2} x^2}_{second\ order} + \ldots \tag{3.1}$$

with the first order term that is linear in x containing the first energy derivative, the second order term that is quadratic in x containing the second derivative and so forth. The order of the derivative defines the order of the corresponding property. To find proper expressions for the energy derivatives it is crucial to consider the physics of the interaction with the external perturbation. A small compilation of different molecular properties expressed as energy derivatives is given in table 3.1. Besides derivatives w.r.t. one type of perturbation there exist as well mixed derivatives, e.g., the nuclear magnetic shielding as a second order property described as energy derivative w.r.t. the magnetic field and the nuclear spin.

Considering the general energy expression $E = E(x, c(x))$ the first energy derivative has the general form of

$$\frac{dE}{dx} = \frac{\partial E}{\partial x} + \frac{\partial E}{\partial c}\frac{\partial c}{\partial x} \tag{3.2}$$

with c being the perturbation dependent wave function parameters, e.g., MO coefficients. Note, that in general one has to distinct between explicit and implicit dependencies of the energy and wave function on the external perturbation. Examples for the latter are MO coefficients, CI coefficients or CC amplitudes whereas explicit dependencies occur for the Hamiltonian or basis functions. In the case of variationally determined wave function parameters, equation 3.2 simplifies to

Table 3.1: Small compilation of molecular properties expressed as the n^{th} energy derivative with respect to the cartesian coordinates (n_R), electric field (n_F), magnetic field (n_B) or nuclear spin (n_I).[149]

n_R	n_F	n_B	n_I	property
1	0	0	0	energy gradient
2	0	0	0	harmonic vibrational frequencies
3	0	0	0	(cubic) anharmonic corrections
0	1	0	0	electric dipole moment
0	2	0	0	electric polarizability
0	0	1	0	magnetic dipole moment
0	0	2	0	magnetic susceptibility
0	0	0	1	hyperfine coupling
0	0	0	2	spin-spin coupling of different nuclei
1	1	0	0	intensities of fundamental IR transitions
0	1	1	0	circular dichroism
0	0	1	1	nuclear magnetic shielding

$$\frac{dE}{dx} = \frac{\partial E}{\partial x}, \tag{3.3}$$

because the energy is stationary with respect to changes in c and therefore

$$\frac{\partial E}{\partial c} = 0. \tag{3.4}$$

For non-variational wave functions the starting point is the constructions of an energy functional by means of the “Lagrange method of undetermined multipliers”.[151] Given the set of equations $g(x, c(x))$ that determine c, the energy equation is augmented as

$$\tilde{E}(x, c(x), \lambda(x)) = E(x, c(x)) + \lambda(x) g(x, c(x)). \tag{3.5}$$

By making the energy functional stationary w.r.t λ and c the first energy derivative then simplifies to

$$\frac{d\tilde{E}}{dx} = \frac{\partial \tilde{E}}{\partial x} = \frac{\partial E}{\partial x} + \lambda \frac{\partial g}{\partial x} \tag{3.6}$$

where the set of equations $\frac{d\tilde{E}}{d\lambda} = 0$ determines c, $\frac{d\tilde{E}}{dc} = 0$ determines λ and $\tilde{E} = E$. Consequently, no first-order response of the wave function parameters is needed but the zeroth order response to determine λ according to

$$\frac{\partial g}{\partial c}\lambda = -\frac{\partial E}{\partial c}. \tag{3.7}$$

The general expression for the second derivative is

$$\frac{d^2E}{dxdy} = \frac{\partial^2 E}{\partial x \partial y} + \frac{\partial^2 E}{\partial x \partial c}\frac{\partial c}{\partial y} + \frac{\partial^2 E}{\partial y \partial c}\frac{\partial c}{\partial x} + \frac{\partial^2 E}{\partial^2 c}\frac{\partial c}{\partial x}\frac{\partial c}{\partial y} + \frac{\partial E}{\partial c}\frac{\partial^2 c}{\partial x \partial y} \tag{3.8}$$

with the last term again vanishing for variational wave functions.[149, 215]

3.1.1 SCF energy derivative

The SCF energy for unrestricted open-shell systems is given in the AO basis as

$$\begin{aligned} E^{UHF} = &\sum_{\mu\nu}^{\alpha+\beta} P_{\mu\nu} H_{\mu\nu} + \frac{1}{2}\sum_{\mu\nu\sigma\tau} P^{\alpha}_{\mu\nu} P^{\alpha}_{\sigma\tau} (\mu\nu||\sigma\tau) + \frac{1}{2}\sum_{\mu\nu\sigma\tau} P^{\beta}_{\mu\nu} P^{\beta}_{\sigma\tau} (\mu\nu||\sigma\tau) \\ &+ \frac{1}{2}\sum_{\mu\nu\sigma\tau} P^{\alpha}_{\mu\nu} P^{\beta}_{\sigma\tau} (\mu\nu|\sigma\tau) + \frac{1}{2}\sum_{\mu\nu\sigma\tau} P^{\beta}_{\mu\nu} P^{\alpha}_{\sigma\tau} (\mu\nu|\sigma\tau) + V_{nuc} \end{aligned} \tag{3.9}$$

with $H_{\mu\nu}$ being the one-electron integrals, $(\mu\nu|\sigma\tau)$ the two-electron integrals (antisymmetrized in the same-spin case) in Mulliken notation and V_{nuc} the nuclear potential. With the MO coefficients being the variational wave function parameters that are determined via the orthonormality constraint (see subsection 2.2) the first energy derivative is given by

$$\begin{aligned} \frac{dE^{UHF}}{dx} = &\sum_{\mu\nu}^{\alpha+\beta} P_{\mu\nu} \frac{\partial H_{\mu\nu}}{\partial x} + \frac{1}{2}\sum_{\mu\nu\sigma\tau} P^{\alpha}_{\mu\nu} P^{\alpha}_{\sigma\tau} \frac{\partial}{\partial x} (\mu\nu||\sigma\tau) + \frac{1}{2}\sum_{\mu\nu\sigma\tau} P^{\beta}_{\mu\nu} P^{\beta}_{\sigma\tau} \frac{\partial}{\partial x} (\mu\nu||\sigma\tau) \\ &+ \frac{1}{2}\sum_{\mu\nu\sigma\tau} P^{\alpha}_{\mu\nu} P^{\beta}_{\sigma\tau} \frac{\partial}{\partial x} (\mu\nu|\sigma\tau) + \frac{1}{2}\sum_{\mu\nu\sigma\tau} P^{\beta}_{\mu\nu} P^{\alpha}_{\sigma\tau} \frac{\partial}{\partial x} (\mu\nu|\sigma\tau) + \frac{\partial V_{nuc}}{\partial x} \\ &+ \sum_{\mu\nu} W^{\alpha}_{\mu\nu} \frac{\partial S_{\mu\nu}}{\partial x} + \sum_{\mu\nu} W^{\beta}_{\mu\nu} \frac{\partial S_{\mu\nu}}{\partial x} \end{aligned} \tag{3.10}$$

with the energy weighted density matrix for the α-case[1] being

$$W^{\alpha}_{\mu\nu} = \sum_i c^{*\alpha}_{\mu i} \epsilon^{\alpha}_i c^{\alpha}_{\nu i}. \tag{3.11}$$

The expression for the second energy derivative is

$$\begin{aligned}
\frac{d^2 E^{UHF}}{dxdy} =& \sum_{\mu\nu} P_{\mu\nu} \frac{\partial^2 H_{\mu\nu}}{\partial x \partial y} + \frac{1}{2} \sum_{\mu\nu\sigma\tau} P^{\alpha}_{\mu\nu} P^{\alpha}_{\sigma\tau} \frac{\partial^2}{\partial x \partial y} (\mu\nu||\sigma\tau) + \frac{1}{2} \sum_{\mu\nu\sigma\tau} P^{\beta}_{\mu\nu} P^{\beta}_{\sigma\tau} \frac{\partial^2}{\partial x \partial y} (\mu\nu||\sigma\tau) \\
&+ \frac{1}{2} \sum_{\mu\nu\sigma\tau} P^{\alpha}_{\mu\nu} P^{\beta}_{\sigma\tau} \frac{\partial^2}{\partial x \partial y} (\mu\nu|\sigma\tau) + \frac{1}{2} \sum_{\mu\nu\sigma\tau} P^{\beta}_{\mu\nu} P^{\alpha}_{\sigma\tau} \frac{\partial^2}{\partial x \partial y} (\mu\nu|\sigma\tau) \\
&+ \frac{\partial^2 V_{nuc}}{\partial x \partial y} + \sum_{\mu\nu} W^{\alpha}_{\mu\nu} \frac{\partial^2 S_{\mu\nu}}{\partial x \partial y} + \sum_{\mu\nu} W^{\beta}_{\mu\nu} \frac{\partial^2 S_{\mu\nu}}{\partial x \partial y} \\
&+ \sum_{\mu\nu} \frac{\partial P_{\mu\nu}}{\partial y} \frac{\partial H_{\mu\nu}}{\partial x} + \frac{1}{2} \sum_{\mu\nu\sigma\tau} \frac{\partial P^{\alpha}_{\mu\nu}}{\partial y} P^{\alpha}_{\sigma\tau} \frac{\partial}{\partial x} (\mu\nu||\sigma\tau) + \frac{1}{2} \sum_{\mu\nu\sigma\tau} \frac{\partial P^{\beta}_{\mu\nu}}{\partial y} P^{\beta}_{\sigma\tau} \frac{\partial}{\partial x} (\mu\nu||\sigma\tau) \\
&+ \frac{1}{2} \sum_{\mu\nu\sigma\tau} \frac{\partial P^{\beta}_{\mu\nu}}{\partial y} P^{\alpha}_{\sigma\tau} \frac{\partial}{\partial x} (\mu\nu|\sigma\tau) + \frac{1}{2} \sum_{\mu\nu\sigma\tau} \frac{\partial P^{\alpha}_{\mu\nu}}{\partial y} P^{\beta}_{\sigma\tau} \frac{\partial}{\partial x} (\mu\nu|\sigma\tau) \\
&+ \sum_{\mu\nu} \frac{\partial W^{\alpha}_{\mu\nu}}{\partial y} \frac{\partial S_{\mu\nu}}{\partial x} + \sum_{\mu\nu} \frac{\partial W^{\beta}_{\mu\nu}}{\partial y} \frac{\partial S_{\mu\nu}}{\partial x}.
\end{aligned} \tag{3.12}$$

For the second energy derivative the response density, i.e., the response of the MO coefficients, are needed. Those are determined by the CP-SCF equations.[61, 217]

3.1.2 MP2 energy derivative

The total MP2 energy is the sum of the SCF and MP2 correction energies. Therefore, the total MP2 energy derivative simply consists of the SCF energy derivative and the MP2 energy correction derivative

$$\frac{d^2 E^{MP2}}{dxdy} = \frac{d^2 E^{SCF}}{dxdy} + \frac{d^2 E^{MP2corr}}{dxdy}. \tag{3.13}$$

---

[1] The β-case being defined analogously.

3.2 Coupled-perturbed self-consistent field

The response electron(+)/spin(-) density is obtained by taking the derivative of the electron/spin density with respect to the perturbation

$$\frac{d}{dx}\mathbf{P}^{\alpha\pm\beta} = \mathbf{P}^{\alpha\pm\beta,x} = \mathbf{P}^{\alpha,x} \pm \mathbf{P}^{\beta,x}. \tag{3.14}$$

In the following we will look at the spin-α case only and therefore will omit the spin-superscript in favor of clarity.[2] By taking the derivative of equation 2.14 we obtain the SCF response density as

$$\begin{aligned} P^x_{\mu\nu} &= \sum_i \left(c^{*,x}_{\mu i} c_{\nu i} + c^*_{\mu i} c^x_{\nu i} \right) \\ &= \sum_{ia} U^x_{ai} \left(c_{\mu i} c_{\nu a} \pm c_{\mu a} c_{\nu i} \right) - \sum_{ij} S^{(x)}_{ij} c_{\mu j} c_{\nu i} \end{aligned} \tag{3.15}$$

where we have expanded the perturbed MO coefficients as

$$c^x_{\mu p} = \sum_q c_{\mu q} U^x_{qp} \tag{3.16}$$

and made use of the orthonormality condition

$$U^{*,x}_{qp} + S^{(x)}_{pq} + U^x_{pq} = 0 \tag{3.17}$$

as well as the antisymmetry of the perturbed overlap matrix $\mathbf{S}^{(x)}$ so that

$$U^x_{ij} = -U^x_{ji} = -U^{*,x}_{ij} = U^{*,x}_{ji} = -\frac{1}{2} S^{(x)}_{ij}. \tag{3.18}$$

The occupied-virtual/virtual-occupied part of the U^x-coefficients as needed in equation 3.15 are obtained by taking the derivative of the Brillouin condition

---

[2] The spin-β case is defined analogously.

$$0 = \frac{\mathrm{d}}{\mathrm{dx}} \sum_{\mu\nu} c^{*}_{\mu a} F_{\mu\nu} c_{\nu i} = \sum_{\mu\nu} \left(c^{*,x}_{\mu a} F_{\mu\nu} c_{\nu i} + c^{*}_{\mu a} F^{x}_{\mu\nu} c_{\nu i} + c^{*}_{\mu a} F_{\mu\nu} c^{x}_{\nu i} \right) \tag{3.19}$$

where

$$F_{\mu\nu} = \left(\mu | \hat{\mathrm{h}} | \nu \right) + \sum_{\sigma\tau} P_{\sigma\tau} \left(\mu\nu || \sigma\tau \right) + \sum_{\overline{\sigma\tau}} P_{\overline{\sigma\tau}} \left(\mu\nu | \overline{\sigma\tau} \right) \tag{3.20}$$

in the unrestricted case and the overline denotes the opposite spin (here β) contribution. The field derivatives of the individual terms are

$$\begin{aligned}
\sum_{\mu\nu} c^{*,x}_{\mu a} F_{\mu\nu} c_{\nu i} &= \sum_{\mu\nu} \sum_{q} c^{*}_{\mu q} U^{*,x}_{qa} F_{\mu\nu} c_{\nu i} = \left(-U^{x}_{ai} - S^{(x)}_{ai} \right) \epsilon_i && (3.21) \\
\sum_{\mu\nu} c^{*}_{\mu a} F_{\mu\nu} c^{x}_{\nu i} &= \sum_{\mu\nu} c^{*}_{\mu} F_{\mu\nu} \sum_{q} c_{\nu q} U^{*,x}_{qi} = \epsilon_a U^{x}_{ai} && (3.22) \\
\sum_{\mu\nu} c^{*}_{\mu a} \left(\mu | \hat{\mathrm{h}} | \nu \right)^{x} c_{\nu i} &= \sum_{\mu\nu} c_{\mu a} c_{\nu i} h^{(x)}_{\mu\nu} && (3.23) \\
\sum_{\mu\nu\sigma\tau} c^{*}_{\mu a} \left(P_{\sigma\tau} \left(\mu\nu || \sigma\tau \right) \right)^{x} c_{\nu i} &= \sum_{\mu\nu\sigma\tau} c_{\mu a} P^{x}_{\sigma\tau} \left(\mu\nu || \sigma\tau \right) c_{\nu i} + \sum_{\mu\nu\sigma\tau} c_{\mu a} P_{\sigma\tau} \left(\mu\nu || \sigma\tau \right)^{(x)} c_{\nu i} \\
&= \sum_{jb} U^{x}_{bj} \left[\left(ai || jb \right) \pm \left(ai || bj \right) \right] - \sum_{jk} S^{(x)}_{jk} \left(ai || kj \right) && (3.24) \\
&\quad + \sum_{j} \left(ai || jj \right)^{(x)} && (3.25) \\
\sum_{\mu\nu\overline{\sigma\tau}} c^{*}_{\mu a} \left(P_{\overline{\sigma\tau}} \left(\mu\nu | \overline{\sigma\tau} \right) \right)^{x} c_{\nu i} &= \sum_{\mu\nu\overline{\sigma\tau}} c_{\mu a} P^{x}_{\overline{\sigma\tau}} \left(\mu\nu || \overline{\sigma\tau} \right) c_{\nu i} + \sum_{\mu\nu\overline{\sigma\tau}} c_{\mu a} P_{\overline{\sigma\tau}} \left(\mu\nu || \overline{\sigma\tau} \right)^{(x)} c_{\nu i} \\
&= - \sum_{\overline{kj}} S^{(x)}_{\overline{jk}} \left(ai | \overline{kj} \right) + \sum_{\bar{j}} \left(ai | \overline{jj} \right)^{(x)} && (3.26)
\end{aligned}$$

Note that the unperturbed MO coefficients are all real whereas the perturbed U^x- coefficients are complex. In case of electric/magnetic properties the U^x-coefficients are purely real/imaginary, hence the sign ±. Collecting all terms containing the U-coefficients on one side and combining the indices ai to a single index gives the final CP-SCF equations in matrix notation

$$\mathbf{X}\mathbf{U}^{x} = \mathbf{b} \tag{3.27}$$

with

$$\begin{aligned} X_{ai,bj} &= (\epsilon_a - \epsilon_i)\,\delta_{ai,bj} + \left[(ai||jb) \pm (ai||bj)\right] \\ b_{ai} &= S^{(x)}_{ai}\epsilon_i - h^{(x)}_{ai} + \sum_{jk} S^{(x)}_{jk}\,(ai||kj) + \sum_{\bar{j}\bar{k}} S^{(x)}_{\bar{j}\bar{k}}\left(ai||\bar{k}\bar{j}\right) \\ &\quad - \sum_{j}(ai||jj)^{(x)} - \sum_{\bar{j}}\left(ai|\bar{j}\bar{j}\right)^{(x)} \end{aligned} \tag{3.28}$$

In the case of DFT, an additional term due to the XC-functional[218] V_{XC} has to be considered on the *right-hand side* (*RHS*)

$$b_{ai} \leftarrow \sum_{\mu\nu} c_{\mu a} c_{\nu i} \frac{\mathrm{d}\,\langle \mu \mid V_{XC} \mid \nu \rangle}{\mathrm{dx}} \tag{3.29}$$

and for hybrid DFT the HF exchange contributions have to be scaled accordingly in the CP-SCF equations.

In the unrestricted framework the same set of CP-SCF equations has to be formulated analogously for the spin-β case. Hence, a linear equation system of the following form needs to be solved iteratively

$$\begin{pmatrix} \mathbf{X}^{\alpha} & 0 \\ 0 & \mathbf{X}^{\beta} \end{pmatrix} \begin{pmatrix} \mathbf{U}^{\alpha,x} \\ \mathbf{U}^{\beta,x} \end{pmatrix} = \begin{pmatrix} \mathbf{b}^{\alpha} \\ \mathbf{b}^{\beta} \end{pmatrix} \tag{3.30}$$

3.3 EPR parameters

The experimental observables of EPR spectroscopy are given by the SH formalism.[33] These SH parameters alias EPR parameters (within the framework of EPR experiments) depict a very concise summary of the experimental outcome. Here, we will focus on the following form of the Spin-Hamiltonian

$$\hat{H}_{SH} = \mu_B \vec{B}\mathbf{g}\hat{S} + \sum_{N} \hat{S}\mathbf{A}^{(N)}\hat{I}^{(N)} \tag{3.31}$$

with the EPR parameters under consideration $\mathbf{g}$ being the g-tensor and $\mathbf{A}^{(N)}$ the A-tensor for the nuclei N. μ_B is the Bohr magneton, $\vec{B}$ the magnetic field, $\hat{I}^{(N)}$ the nuclear spin for nuclei N and $\hat{S}$ a "fictitious" electron spin. This SH acts on a set of product states solely characterized by the the spin-variables. It is therefore usually of low-dimension and easily to handle by numerical simulation programs such as EasySpin.[219] All spatial parts of the multi-electron wave function are contained implicitly withing the SH parameters.[220] While spectroscopists obtain these parameters by least-square fitting to experimental data, theoreticians aim at connecting fundamental physics to derive at expressions to calculate those parameters. Starting from the Born-Oppenheimer Hamiltonian $\hat{H}_{BO}$ a perturbing Hamiltonian $\hat{H}_1$ is added comprising all interactions based on first-principle physics that give rise to the experimental observations

$$\hat{H} = \hat{H}_{BO} + \hat{H}_1. \tag{3.32}$$

Such interactions can arise from relativity, i.e., SOC or describe couplings between electrons to an external magnetic field, i.e., Zeeman effect, and couplings between electronic and nuclear spins, respectively.[34] In the following we will have a closer look at the expressions for the g- and A-tensor as a result from the linear response treatment of SH parameters as described in subsection 3.1. Within this framework the g- and A-tensor can be calculated at the chosen level of theory providing that the (spin) density and response (spin) density are available for the particular method.

3.3.1 A-tensor

The A-tensor, rather known as *hyperfine coupling constant* (*HFCC*), describes the interaction between the electron spin and the magnetic moment of the nuclei N. For light elements the A-tensor can be separated into two main contributions[98, 104, 221]

$$A^{(N)} = A^{(N),FC} + A^{(N),SD} \tag{3.33}$$

with $A^{(N),FC}$ being the Fermi coupling term, which is the isotropic contribution to the HFCC, and $A^{(N),SD}$ being the spin dipole term, which is the anisotropic contribution.

Within the framework of linear response theory the components of the HFCC can be simply calculated by means of the spin density $\mathbf{P}^{\alpha-\beta}$

$$A_{pq}^{(N),FC} = \delta_{pq}\frac{8\pi}{3}\frac{P_N}{2S}\sum_{\mu\nu} P_{\mu\nu}^{\alpha-\beta}\left\langle \mu \,\middle|\, \delta(\vec{R}_N) \,\middle|\, \nu \right\rangle, \tag{3.34}$$

$$A_{pq}^{(N),SD} = \frac{P_N}{2S}\sum_{\mu\nu} P_{\mu\nu}^{\alpha-\beta}\left\langle \mu \,\middle|\, r^{-5}\left(\vec{r}_N^{\,2}\delta_{pq} - 3\vec{r}_{N,p}\vec{r}_{N,q}\right) \,\middle|\, \nu \right\rangle, \tag{3.35}$$

where $p, q \in \{x, y, z\}$, S being the total spin and the prefactor P_N being the product of the electronic and nuclear g-values and Bohr-magnetons, respectively,

$$P_N = g_e g_N \gamma_e \gamma_N. \tag{3.36}$$

For the given terms the A-tensor is thus considered a first order property. Second order terms arise from SOC interactions that become crucial for heavier nuclei.[83, 84, 222, 223] It is evident that the Fermi coupling term depends on the spin density at the nucleus of interest. This requires very accurate descriptions of the wave function close to the nucleus. Consequently, the chosen basis set should be flexible at the core region and capable of describing core level spin polarization accurately.[224]

3.3.2 g-tensor

In the one-component scheme the g-tensor is described as a second order property by linear response theory, i.e., being the second energy derivative with respect to the magnetic field B and the total electron spin S

$$\mathbf{g} = \frac{1}{\mu_B}\left.\frac{\partial^2 E}{\partial B \partial S}\right|_{B,S=0}. \tag{3.37}$$

The g-tensor itself can be separated into four main contributions[35, 38, 47, 225, 226]

$$\mathbf{g} = g_e\mathbf{1} + \Delta\mathbf{g}^{\mathrm{RMC}} + \Delta\mathbf{g}^{\mathrm{GC}} + \Delta\mathbf{g}^{\mathrm{OZ/SOC}} \tag{3.38}$$

of which the latter three correction terms describe the deviations from the g-value of a free-electron[227]

$$g_e = 2.002319304386(20). \tag{3.39}$$

The second and third terms refer to the relativistic mass correction (RMC) and the diamagnetic correction (GC) to the g-tensor which can be expressed by means of the spin density $P_{\mu\nu}^{\alpha-\beta}$

$$\Delta \mathbf{g}^{\mathrm{RMC}} = -\frac{\alpha^2}{S}\sum_{\mu\nu} P_{\mu\nu}^{\alpha-\beta} \left\langle \mu \left| -\frac{1}{2}\vec{\nabla}^2 \right| \nu \right\rangle , \tag{3.40}$$

$$\Delta g_{pq}^{\mathrm{GC}} = \frac{\alpha^2}{4S}\sum_{A,i} Z_{eff}^{A} \sum_{\mu\nu} P_{\mu\nu}^{\alpha-\beta} \left\langle \mu \left| \frac{\delta_{pq}\vec{r}_A\vec{r}_O - \vec{r}_{A,p}\vec{r}_{O,q}}{\left|\vec{r}_i - \vec{R}_A\right|^3} \right| \nu \right\rangle \qquad p,q \in \{x,y,z\}, \tag{3.41}$$

where α is the fine structure constant and Z_{eff}^{A} the semi-empirically chosen effective nuclear charge from atom A at position $\vec{R}_A$.[228] $\vec{r}_O$ is the vector relative to the chosen origin O and, analogously, $\vec{r}_A$ is the electronic position with respect to nucleus A.

The last term is the actual second order orbital Zeemann/SOC term which contains the perturbed (response) spin density[34]

$$\Delta g_{pq}^{\mathrm{OZ/SOC}} = -\frac{1}{S}\sum_{\mu\nu} \frac{\partial P_{\mu\nu}^{\alpha-\beta}}{\partial B_p} \left\langle \mu \left| \hat{\mathrm{h}}_q^{\mathrm{SOC}} \right| \nu \right\rangle \qquad p,q \in \{x,y,z\}. \tag{3.42}$$

In this thesis the spin-orbit operator $\hat{\mathrm{h}}_q^{\mathrm{SOC}}$ is chosen to be the spin-orbit mean field operator[229] applied with the *spin-orbit mean field one-center approximation* (*SOMF*(*1X*)).[67]

As it is known for magnetic properties, the g-tensor is origin dependent for finite basis sets.[230] Though, its dependency is not as pronounced as for nuclear magnetic shieldings because it is a molecular property, i.e., averaged over the whole molecule.[52] This “gauge dependency problem” can be circumvented by using GIAOs[54, 56, 65, 231] for which the latter two correction terms of the g-tensor change to

$$\Delta g_{pq}^{\mathrm{GC}} = \frac{\alpha^2}{4S}\sum_{A,i} Z_{eff}^{A}\sum_{\mu\nu} P_{\mu\nu}^{\alpha-\beta}\left\langle \mu \left| \frac{\delta_{pq}\vec{r}_A\vec{r}_N - \vec{r}_{A,p}\vec{r}_{N,q}}{\left|\vec{r}_i - \vec{R}_A\right|^3} \right| \nu \right\rangle \qquad p,q \in \{x,y,z\} \tag{3.43}$$

$$\Delta g_{pq}^{\mathrm{OZ/SOC}} = -\frac{1}{S}\sum_{\mu\nu}\left[\frac{\partial P_{\mu\nu}^{\alpha-\beta}}{\partial B_p}\left\langle \mu \left| \hat{\mathrm{h}}_q^{\mathrm{SOC}} \right| \nu \right\rangle + P_{\mu\nu}^{\alpha-\beta}\frac{\partial}{\partial B_p}\left\langle \mu \left| \hat{\mathrm{h}}_q^{\mathrm{SOC}} \right| \nu \right\rangle\right] \quad p,q \in \{x,y,z\} \tag{3.44}$$

with the perturbed SOMF(1X) integrals being

$$\frac{\partial}{\partial B_p}\left\langle \mu \left| \hat{\mathrm{h}}_q^{\mathrm{SOC}} \right| \nu \right\rangle = \mathbf{Q}_{MN}\left\langle \mu \left| r_N \hat{\mathrm{h}}^{\mathrm{SOC}} \right| \nu \right\rangle \tag{3.45}$$

where $\vec{r}_N$ refers to the electronic position with respect to nucleus N. $\mathbf{Q}_{MN}$ is the antisymmetric matrix

$$\mathbf{Q}_{MN} = \begin{bmatrix} 0 & -Z_{MN} & Y_{MN} \\ Z_{MN} & 0 & -X_{MN} \\ -Y_{MN} & X_{MN} & 0 \end{bmatrix} \tag{3.46}$$

which can be used to rewrite a cross product as a matrix multiplication $\vec{R}_{MN} \times \vec{r} = \mathbf{Q}_{MN}\,\vec{r}$.

The application of GIAOs however give rise to additional terms at the expense of significantly higher computational costs.[232, 233] Therefore, alternative choices of a reasonable origin can be justified for special cases. For instance if the spin density is strongly localized, setting the origin to the center of spin density can give reasonable results at lower computational costs.[62]

3.4 Origin of $\Delta \mathbf{g}^{GC}$ and $\Delta \mathbf{g}^{OZ/SOC}$

The origin of the last two correction terms for the g-tensor in equation 3.38 is rooted in the treatment of the SO interaction. It is a commonly used approximation to treat the two electron term resulting from the Breit-Pauli SOC operator as "screening" of the nuclear charges. Therefore, the SOC term can be treated as a one-electron term and the effective SOC operator consequently has the following form

$$\hat{\mathrm{h}}_{SOC} = \sum_{A}\sum_{i}\xi(r_{iA})\left(\vec{r}_i^{A} \times \vec{p}_i\right)\vec{s}_i \qquad \text{with} \qquad \xi(r_{iA}) = \frac{\alpha^2}{2}\frac{Z_{eff}^{A}}{r_{iA}^{3}}. \tag{3.47}$$

In the case of a magnetic field the particle momentum operator is replaced by

$$\pi = -i\vec{\nabla} + A(\vec{r}) \qquad \text{with} \qquad A(\vec{r}) = \frac{1}{2}\vec{B} \times \vec{r}_O \tag{3.48}$$

with $A(\vec{r})$ as the vector potential introducing the dependency on the magnetic field. Plugging equation 3.48 into equation 3.47 and expanding the terms gives the operator for the gauge correction term of the SOC for $\Delta\mathbf{g}^{GC}$ in the no-GIAO case.
In the case of using GIAOs field dependent atomic orbitals are applied of the following form

$$\tilde{\chi}(\vec{r}_M, A_M) = \exp\left(-iA_M \cdot \vec{r}\right)\chi(\vec{r}_M) \qquad \text{with} \qquad A_M = \frac{1}{2}\vec{B} \times R_{MO}. \tag{3.49}$$

Inserting those into the molecular integrals and reformulating them in the regular AO basis gives

$$\left\langle \tilde{\mu}(\vec{r}_M, A_M) \middle| \hat{\mathrm{h}}_{SOC} \middle| \tilde{\nu}(\vec{r}_N, A_N) \right\rangle \tag{3.50}$$

$$= \left\langle \mu \middle| \exp(iA_M \cdot \vec{r})\hat{\mathrm{h}}_{SOC}\exp(-iA_N \cdot \vec{r}) \middle| \nu \right\rangle \tag{3.51}$$

$$= \left\langle \mu \middle| \exp(iA_{MN} \cdot \vec{r})\sum_{i,A}\xi(r_{iA})\left[(\vec{s}_i \times \vec{r_{iA}})(-i\vec{\nabla}) + \frac{1}{2}(\vec{s}_i \times \vec{r}_{iA})(\vec{B} \times \vec{r}_N)\right] \middle| \nu \right\rangle \tag{3.52}$$

due to the non-zero commutator

$$\left[-i\vec{\nabla}, \exp(-iA_N \cdot \vec{r})\right] = -\exp(-iA_N \cdot \vec{r})A_N. \tag{3.53}$$

Taking the partial derivatives $\left.\frac{\partial^2}{\partial B \partial S}\right|_{B,S=0}$ and $\left.\frac{\partial}{\partial B}\right|_{B,S=0}$ then results in the final GIAO correction terms of the g-tensor given in equations 3.43 and 3.44.

4 Line broadening in EPR

Experimental spectra are characterized by the following main features: the position of the signal as well as the intensity and width (related to shape) of the corresponding signal. Differences in linewidths originate from different broadening mechanisms, which in return define the shape of the signal. There are two types of broadening mechanisms leading to either *homogeneous* or *inhomogeneous* line broadening. The first is caused by the Heisenberg uncertainty principle and leads to a Lorentzian line shape with the corresponding *full width at half maximum* (*FWHM*) being related to the electron spin relaxation time of the system. In EPR it is usually referred to as "intrinsic linewidth". The inhomogeneous line broadening is rooted in the structural inhomogeneity of the measured sample and gives rise to a Gaussian line shape. It reflects the distribution of the measured EPR parameters which is caused by the different microenvironment each molecule in the sample is exposed to.[130] The ALW that results from the experimental measurement is therefore a convolution of these two broadening mechanisms.

From a chemical perspective the inhomogeneous line broadening is of interest and can further be divided into a *field independent* and a *field dependent* broadening. The former results from unresolved hyperfine and quadruple interactions of weakly coupled nuclei in the surrounding, either from the solute itself or from the solvent. This line broadening does not change the ALW with increasing microwave frequency whereas the latter does. The field dependency appears through the Zeemann interaction that leads to a distribution of the g-values. In a frozen solution this relates to the microheterogeneity in the molecular ensemble and therefore causes different resonance frequencies for each molecule. Since at higher microwave frequencies, the different resonance frequencies will split apart, a broadening of the ALW is observable. This increase is believed to be linear with respect to the microwave frequency and the underlying phenomenon is referred to as "g-strain".[132–134, 234] Note that in the case of both field independent and field dependent line broadening being observable the ALW then is described as

$$ALW = \sqrt{lw_{findep}^2 + lw_{fdep}^2}. \tag{4.1}$$

Part II

Method development

5 Analytical second order derivatives of RI-MP2 and DHDFT for open shell systems

In this chapter we report – motivated by the success of DHDFT – the first implementation of analytic second derivatives for property calculations in the unrestricted formalism at the level of MP2 and DHDFT including RI approximation and the usage of GIAOs. This method is then applied to a set of small molecules for the computation of the g-tensor.

First the important working equations for the implementation of the perturbed (response) electron and spin-densities are derived based on the theoretical foundations given in chapters 2 and 3. Finally, numerical calculations are reported that demonstrate both the accuracy and the computational cost of the new methodology.

5.1 The unrestricted RI-MP2 response density

The relaxed perturbed/response MP2 density is obtained by taking the derivative of the stationary conditions of the Lagrangian 2.38 with respect to the magnetic field

$$\frac{d^2\mathcal{L}}{dBdU} = 0. \tag{5.1}$$

This results in the perturbed Z-vector equation, given here for the α-case, that needs to be solved according to

$$
\begin{aligned}
&\sum_{ia} Z^B_{ai}\left[\left(\epsilon_b-\epsilon_j\right)\delta_{ab}\delta_{ij}+(aj|bi)-(ab|ji)\right] \\
&\quad = 2\Bigg\{\sum_{aP}\left[\left(\overset{ssP,B}{\Gamma}_{ja}+\overset{osP,B}{\Gamma}_{ja}\right)B^P_{ba}+\left(\overset{ssP}{\Gamma}_{ja}+\overset{osP}{\Gamma}_{ja}\right)B^{P,B}_{ba}\right] \\
&\quad -\sum_{iP}\left[\left(\overset{ssP,B}{\Gamma}_{ib}+\overset{osP,B}{\Gamma}_{ib}\right)B^P_{ij}+\left(\overset{ssP}{\Gamma}_{ib}+\overset{osP}{\Gamma}_{ib}\right)B^{P,B}_{ij}\right] \\
&\quad -\sum_a\frac{1}{2}Z_{aj}F^B_{ab}+\sum_i\frac{1}{2}Z_{bi}F^B_{ji}-\sum_{pq}\left[D_{pq}\left(pq||jb\right)^{(B)}+D_{\overline{pq}}\left(\overline{pq}||jb\right)^{(B)}\right] \\
&\quad -\sum_r\frac{1}{2}U^B_{rb}\mathcal{R}\left[\mathbf{D}\right]_{jr}+\sum_r\frac{1}{2}U^B_{rj}\mathcal{R}\left[\mathbf{D}\right]_{rb}-\sum_r\frac{1}{2}U^B_{rb}\mathcal{R}\left[\overline{\mathbf{D}}\right]_{jr}+\sum_r\frac{1}{2}U^B_{rj}\mathcal{R}\left[\overline{\mathbf{D}}\right]_{rb} \\
&\quad +\frac{1}{2}\mathcal{R}\left[\mathbf{D}'^B\right]_{bj}+\frac{1}{2}\mathcal{R}^{XC,(B)}\left[\mathbf{D}\right]_{bj}-\overline{\mathcal{R}}\left[\mathbf{U}^B\mathbf{D}\right]_{bj}\Bigg\}
\end{aligned}
\tag{5.2}
$$

with the Fock response being

$$
\overline{\mathcal{R}}\left[\mathbf{D}^B\right]_{rs}=2\sum_{pq}D^B_{pq}\left(pr|sq\right)=-\overline{\mathcal{R}}\left[\mathbf{D}^B\right]_{sr}.
\tag{5.3}
$$

The necessary quantities for the calculation of the relaxed response density are given in the following.

For the unrelaxed perturbed density $\mathbf{D}'^B$ we need the perturbed amplitudes that are obtained by the field derivative of the residual equations 2.30 – 2.32

$$
\begin{aligned}
t^{ij,B}_{ab} &= \Bigg\{\sum_P\left[B^{P,B}_{ai}B^P_{bj}+B^P_{ai}B^{P,B}_{bj}-B^{P,B}_{aj}B^P_{bi}-B^P_{aj}B^{P,B}_{bi}\right] \\
&\quad -\sum_k\left[t^{ik}_{ab}F^B_{kj}+t^{kj}_{ab}F^B_{ki}\right]+\sum_c\left[t^{ij}_{ac}F^B_{cb}+t^{ij}_{cb}F^B_{ca}\right]\Bigg\}/\Delta_{ijab}=t^{ji,B}_{ba},
\end{aligned}
\tag{5.4}
$$

$$
\begin{aligned}
t^{\bar{i}j,B}_{\bar{a}b} &= \Bigg\{\sum_P\left[B^{P,B}_{\overline{ai}}B^P_{bj}+B^P_{\overline{ai}}B^{P,B}_{bj}\right] \\
&\quad -\sum_k\left[t^{\bar{i}k}_{\bar{a}b}F^B_{kj}+t^{\bar{k}j}_{\bar{a}b}F^B_{\overline{ki}}\right]+\sum_c\left[t^{\bar{i}j}_{\bar{a}c}F^B_{cb}+t^{\bar{i}j}_{\bar{c}b}F^B_{\overline{ca}}\right]\Bigg\}/\Delta_{\bar{i}j\bar{a}b}=t^{j\bar{i},B}_{b\bar{a}}.
\end{aligned}
\tag{5.5}
$$

The unrelaxed perturbed density then is

$$D'^{B}_{ij} = \sum_k \left[\frac{1}{2} \left(\left\langle \mathbf{T}^{jk,B} \mathbf{T}^{ki} \right\rangle - \left\langle \mathbf{T}^{jk} \mathbf{T}^{ki,B} \right\rangle \right) + \left\langle \mathbf{T}^{j\bar{k},B} \mathbf{T}^{\bar{k}i} \right\rangle - \left\langle \mathbf{T}^{j\bar{k}} \mathbf{T}^{\bar{k}i,B} \right\rangle \right] = -D'^{B}_{ji}, \tag{5.6}$$

$$D'^{B}_{ab} = \sum_{ij} \left[\frac{1}{2} \left(\mathbf{T}^{ji,B} \mathbf{T}^{ij} - \mathbf{T}^{ji} \mathbf{T}^{ij,B} \right) + \mathbf{T}^{j\bar{i},B} \mathbf{T}^{\bar{i}j} - \mathbf{T}^{j\bar{i}} \mathbf{T}^{\bar{i}j,B} \right]_{ab} = -D'^{B}_{ba}. \tag{5.7}$$

To obtain the relaxed perturbed density the field derivative of equation 2.40 is required

$$D^{B}_{ai} = \frac{1}{2} Z^{B}_{ai} = -D^{B}_{ia}. \tag{5.8}$$

The derivatives of the RI three-index integrals and of three-index density matrices are

$$B^{P,B}_{pq} = B^{P,(B)}_{pq} + \sum_k \left[U^{B}_{kq} B^{P}_{pk} - U^{B}_{kp} B^{P}_{kq} \right] + \sum_c \left[U^{B}_{cq} B^{P}_{pc} - U^{B}_{cp} B^{P}_{cq} \right] = -B^{B}_{qp}, \tag{5.9}$$

$$B^{P,(B)}_{pq} = \sum_Q (pq|Q)^{(B)} \left(V^{-\frac{1}{2}} \right)_{QP} = -B^{P,(B)}_{qp}, \tag{5.10}$$

$$\overset{ss}{\Gamma}{}^{P,B}_{ia} = \sum_{jb} \left[t^{ij,B}_{ab} B^{P}_{jb} + t^{ij}_{ab} B^{P,B}_{jb} \right], \tag{5.11}$$

$$\overset{os}{\Gamma}{}^{P,B}_{ia} = \sum_{jb} \left[t^{i\bar{j},B}_{ab} B^{P}_{\bar{j}\bar{b}} + t^{i\bar{j}}_{ab} B^{P,B}_{\bar{j}\bar{b}} \right]. \tag{5.12}$$

The final relaxed perturbed MP2 density is then completed as

$$\mathbf{D}^{B} = \mathbf{D}'^{B} + \mathbf{Z}^{B}. \tag{5.13}$$

5.2 Implementation details

The implementation of the RI-MP2 relaxed perturbed density in ORCA as shown in algorithm 1 using the unrestricted formalism is very similar to the closed shell case which is thoroughly described in reference [167]. Care has to be taken of the different spin cases, i.e., there exists an α- and a β-density which are coupled via mixed spin amplitudes (eq. 2.34,5.5) or Coulomb integral contributions of the Fock response (eq. 2.43). The loops over operators (*op1* and *op2*) takes care of this spin case distinction.

An important point to consider is the treatment of the two-electron integrals occurring on the *left-hand side* (*LHS*) and the RHS of the Z-vector and perturbed Z-vector equations (eq. 2.39 and 5.2, respectively) as well as in the perturbed Fock matrix $\mathbf{F}^B$ contributions to the perturbed amplitudes (eq. 5.4 and 5.5, respectively). Even though a same treatment of the two-electron integrals as in the SCF procedure would be most consistent, the terms on the LHS are treated with the so-called RIJ-DX approximation since the RI approximation for the exchange integrals does not improve the computational performance when they have to be contracted with the density matrix defined for the entire MO space. In the RIJ-DX method, the RI approximation is only applied to the Coulomb integrals whereas the exchange integrals are computed in an integral-direct fashion employing traditional four center repulsion integrals.

5.3 Computational details

All calculations were done using the current development version of ORCA 4.2 with the following tasks in mind [136]: (1) A benchmark study is conducted based on sets of small radicals since, to our knowledge, no data has been provided so far in literature concerning g-tensor calculations at the MP2 level with GIAOs. This benchmark study therefore includes basis set convergence, comparison to experimental values quoted from references [55, 235] and to highly accurate data at CC level [52]. (2) The timing and computational scaling with system size is investigated in order to determine the limits and the efficiency of the methodology.

The geometries of the small radical test sets were used from reference [47] and [52], respectively, whereas the geometries of the medium to large size molecules are provided in appendix A. Two DHDFs were chosen for this study: B2PLYP as representative of the "simple" DHDFT and DSD-PBEP86 as representative of the dispersion-corrected spin-component-scaled DHDFT.[74] `VeryTightSCF` convergence criteria were applied as well as a threshold of 10^{-8} for the convergence of the Z-vector solution. All calculations were done using GIAOs for the gauge origin treatment. Basis sets of the def2-family by Ahlrichs et al. [236] and aug-cc-family by Dunning et al. [237, 238] were used for the calculations.

```
begin
    preparation:
    · make and store all $B^P$ and $B^{P,B}$
    · read $\mathbf{D}$ and $U_{ai}^B$
    · complete $\mathbf{U}^B$ and $\mathbf{F}^B$
    for $op1 \in \{\alpha, \beta\}$ do
        for $batch \in \{number\ of\ batches\}$ do
            for $i \in batch$ do
                for $op2 \in \{\alpha, \beta\}$ do
                    for $j \in \{occupied\}$ do
                        · make amplitudes $t^{ij}$
                        · make $\Gamma$ integrals
                        · make derivative amplitudes $t^{ij,B}$
                        · make derivative $\Gamma^B$ integrals
                        · make contribution to virtual block of response density $D_{ab}^B$
                    end
                    for $j \in \{occupied\}$ do
                        · make contribution to occupied block of perturbed density
                          $D_{ij}^{\prime B}$
                    end
                end
                · make three-external $\Gamma^{P,B} B^P$ and $\Gamma^P B^{P,B}$ to RHS of perturbed
                  Z-vector
            end
        end
    end
    · Fock response contribution to RHS of perturbed Z-vector
    · solve perturbed Z-vector equations
    · complete relaxed response density $D^B$
end
```

Algorithm 1: Pseudocode of the unrestricted RI-MP2 response density implementation in ORCA.

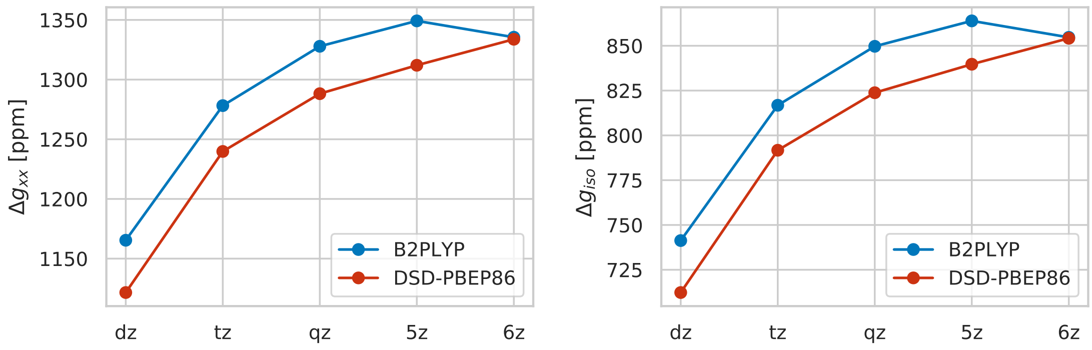

Figure 5.1: Basis set convergence for B2PLYP and DSD-PBEP86 DHDFT using the aug-cc-pVXZ (X=d,t,q,5,6) basis set family on the NH radical.

5.4 Results

5.4.1 Basis set convergence

The basis set convergence was tested using the NH radical. Only the g_{xx}-component is investigated, since the g_{zz}-component shows almost no effect as, for symmetry reasons, its main contribution is the isotropic relative mass correction term, which is not very challenging from a computational point of view. The basis set convergence for the g_{iso} value shows the same behavior as for the g_{xx} value since it is the main contribution to the isotropic value as shown in figure 5.1.

It can be seen that both tested DHDFT converge to almost the same value for a sextuple-ζ basis set with differences <10 ppm. Their convergence towards the complete basis set limit (CBS) is rather slow, which is characteristic for wave function based correlation theories. B2PLYP converges faster than DSD-PBEP86 up to the quintuple-ζ basis but the next step to the sextuple-ζ basis leads to a decrease of the g-tensor components. This behavior is presently not understood. The convergence data for the DSD-PBEP86 functional show a more regular trend. However, for both functionals the improvement by changing from double-ζ to triple-ζ is the most pronounced. Thus, the use of at least a triple-ζ basis set for the g-tensor calculation with double-hybrid functionals appears to be the minimum requirement. At this level, basis set incompleteness errors on the order of 50 ppm would need to be tolerated.

Table 5.1: Statistical evaluation of the calculated Δg-values for the set of seven small radicals ($H_2O^+, CO^+, HCO, C_3H_5, NO_2, NF_2$ and MgF) and the linear regression parameters of the fit depicted in figure 5.2.

	RI-MP2		B2PLYP		DSD-PBEP86	
	def2-TZVPP	aug-cc-pVTZ	def2-TZVPP	aug-cc-pVTZ	def2-TZVPP	aug-cc-pVTZ
R^2	0.983	0.983	0.988	0.988	0.988	0.988
slope	0.934	0.913	0.966	0.943	0.957	0.936
standard deviation [ppm]	551	579	445	469	443	484
maximum error [ppm]	1053	1128	962	948	861	970
mean unsigned error [ppm]	475	474	386	399	385	423
mean signed error [ppm]	158	157	12	56	12	75

5.4.2 Comparison with experiment

In the next step a set of small radicals was chosen for the comparison of the calculated with experimental principle g-shifts: H_2O^+, CO^+, HCO, C_3H_5, NO_2, NF_2 and MgF.[55, 235] This was done for two different triple-ζ basis sets, namely def2-TZVPP and aug-cc-pVTZ. Figure 5.2 shows the plot of the experimental vs. calculated g-shifts for both DHDFT including the corresponding linear regression plots (colored solid lines) as well as for the pure RI-MP2 method. The black solid line corresponds to the ideal match between experimental and computational data. It is evident, that the difference between both basis sets is very small. The computed values of both DHDFT are in good agreement with the experimental ones except for the Δg_{yy} value of H_2O^+, which was excluded from this data set since its deviation of about 3000 ppm would have distorted not only the visualization but also the statistical analysis. The data of the statistical analysis including the linear regression parameters are presented in table 5.1. They confirm the good agreement of the calculated values with the experimental ones with a slope of almost 1 for all tested cases. As expected for molecular properties, pure RI-MP2 performs less well than both tested DHDFT which show similarly good performance. According to the statistical evaluation the def2-TZVPP basis set gives slightly better results than the aug-cc-pVTZ.

5.4.3 Comparison to CCSD

In this section we compare the performance of the DHDFT to other methods with CCSD as the most accurate reference currently available. For consistency the same set of small radicals as in the reference [52] which is used for comparison was tested. Note that the values taken from the reference were all computed without using GIAOs. It was shown that the use of GIAOs do not lead to a very pronounced change for g-tensor

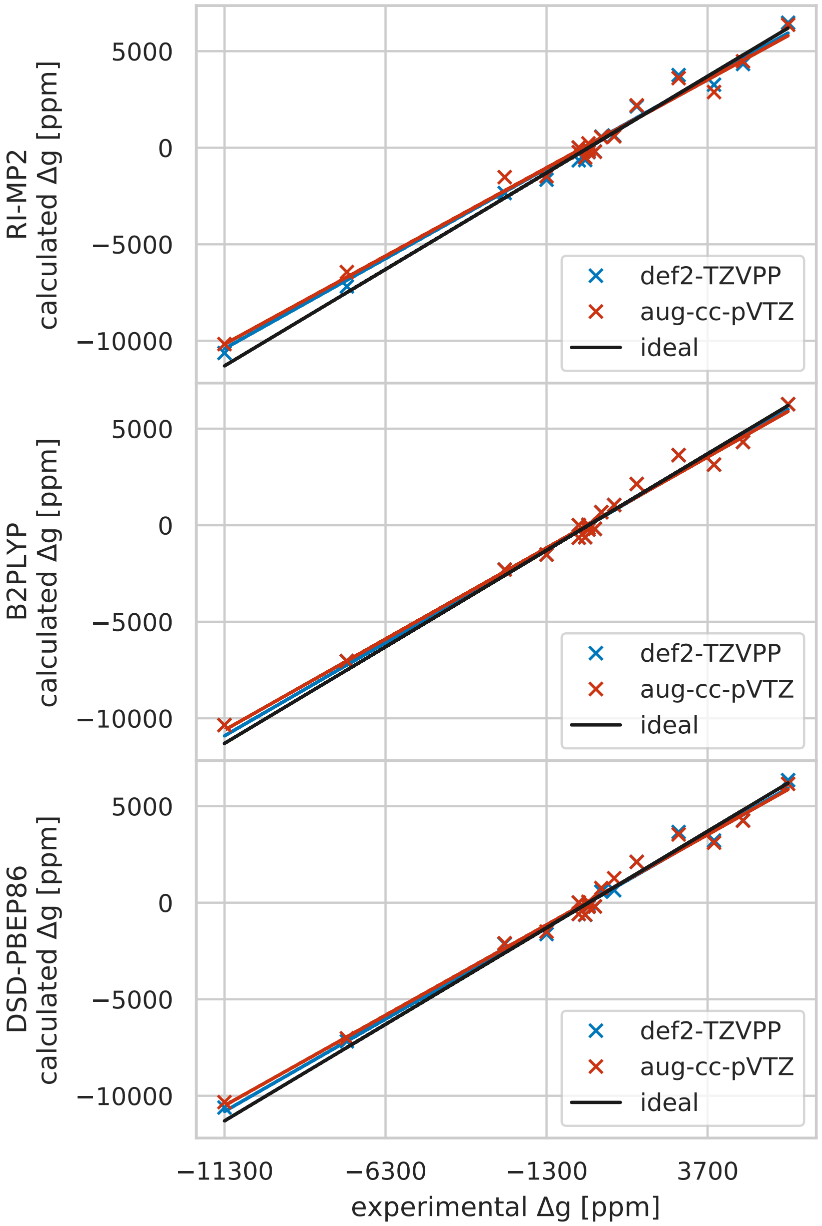

Figure 5.2: Plots of calculated versus experimental Δg-values including linear regression fit (depicted by the colored solid lines) for pure RI-MP2, the B2PLYP and DSD-PBEP86 DHDFs using different triple-ζ basis sets.

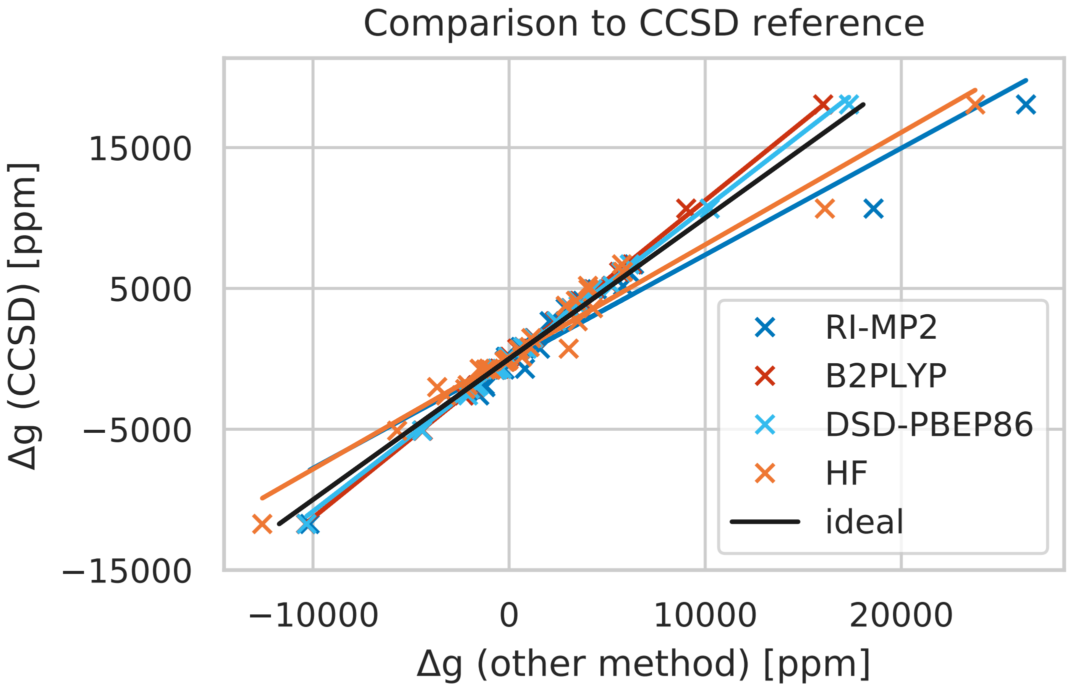

Figure 5.3: Plot of calculated Δg-values using different methods/functionals (RI-MP2, B2PLYP, DSD-PBEP86, HF) versus CCSD-based values including linear regression fit (depicted by the colored solid lines).

calculations (unlike NMR chemical shifts). On one hand this may be related to the fact that, in contrast to nuclear chemical shieldings, the g-tensor is a global property and on the other hand that g-shifts tend to be much larger than chemical shieldings while gauge non-invariance errors tend to be more comparable.[52]

Again, the Δg_{yy} component of H_2O^+ was removed from the data set for the statistical evaluation for the same reasons as before since all methods show difficulties in treating the H_2O^+ radical. Figure 5.3 shows the plots of the pure RI-MP2 and DHDF g-shifts vs. the CCSD g-shifts with the solid colored lines corresponding to a linear fit of the data sets. For comparison, values calculated with HF are also provided. A clear improvement to HF g-shifts with DHDFT is observed. This was expected as correlation effects are non-negligible for g-tensor calculations. However, pure RI-MP2 performs distinctly worse than both DHDFT and interestingly even worse than HF. This observation is quantified through a statistical analysis presented in table 5.2. The detailed data for each molecule in the test set are given in table 5.3.

One source for poor performances of unrestricted wave function approaches may be

Table 5.2: Statistical evaluation of the calculated Δg-values at different levels of theory for the set of 14 small radicals given in table 5.3 and the linear regression parameters of the fit depicted in figure 5.3.

	RI-MP2	B2PLYP	DSD-PBEP86	HF[52]	B3LYP[52]
R^2	0.927	0.998	0.998	0.960	0.998
slope	1.223	0.886	0.927	1.204	1.017
standard deviation [ppm]	1971	572	414	1539	236
maximum error [ppm]	8295	1376	1397	5708	736
mean unsigned error [ppm]	871	342	291	822	146
mean signed error [ppm]	643	-120	-25	140	22

spin contamination. Its measurement is the difference between the expectation value $\langle \hat{S}^2 \rangle$ and the ideal value computed by $S(S+1)$, where S is the total spin of the system. This difference is an indicator for the quality of the underlying wave function. The mean spin contamination values are 0.0617, 0.0617, 0.0146 and 0.0274 for pure RI-MP2, HF, B2PLYP and DSD-PBEP86, respectively. The values for RI-MP2 and HF are two to four times larger than for the DHDFT which supports the observation given in figure 5.3 and table 5.3. However, somewhat surprisingly, looking at the dependency of the g-shift component error with respect to the CCSD values on the corresponding spin contamination, no correlation can be observed (figure 5.4). In addition, the spin contamination for DSD-PBEP86 is intrinsically larger than for B2PLYP as by construction DSD-PBEP86 contains a higher fraction of HF exchange. Nonetheless, it shows a slightly better performance than B2PLYP. Hence, the good performance most likely relies on error cancellation. In any case, no clear correlation can be established between the amount of spin contamination of the corresponding error in g-shift calculations.

In addition to the methods so far discussed, some data for the popular hybrid functional B3LYP were taken into account for the statistical analysis, but not plotted in figure 5.3 in the interest of clarity. It is evident from the comparison that despite the improvement of the calculated g-shifts by using DHDFT over HF and pure RI-MP2, both DHDFT are still being outperformed by B3LYP with respect to both accuracy, at least for the hearin chosen test set, and efficiency. There are some isolated exceptions where one of the DHDFT performs better than B3LYP (B2PLYP: NF_2 Δg_{yy} and NF_3^+ Δg_{zz}; DSD-PBEP86: NH Δg_{zz}, OH^+ Δg_{zz} and H_2CO^+ Δg_{zz}). For pure RI-MP2 and the DSD-PBEP86 functional a sign error is however observed for the Δg_{yy} value of H_2CO^+. Thus, overall the hope that wave function correlation could 'repair' some of the shortcomings of DFT for this specific magnetic property have not materialized.

Table 5.3: Comparison of RI-MP2, the DHDFT B2PLYP and DSD-PBEP86 with CCSD, HF and B3LYP Δg-values given in ppm and taken from reference [52].

	component	CCSD[52]	RI-MP2	B2PLYP	DSD-PBEP86	HF[52]	B3LYP[52]
CN	Δg_{xx}	-2151	-1930	-1980	-1997	-2237	-2193
	Δg_{zz}	-124	-161	-141	-151	-81	-134
CO^+	Δg_{xx}	-2598	-1524	-2299	-2097	-3225	-2656
	Δg_{zz}	-125	-216	-142	-158	-63	-133
BO	Δg_{xx}	-1870	-1244	-1622	-1546	-2113	-1857
	Δg_{zz}	-60	-103	-70	-75	-27	-68
NH	Δg_{xx}	-105	-105	-106	-105	-109	-106
	Δg_{zz}	1465	1294	1278	1240	1133	1363
OH^+	Δg_{xx}	-173	-173	-174	-172	-178	-174
	Δg_{zz}	4119	3742	3586	3497	3405	3704
H_2O^+	Δg_{xx}	-188	-210	-189	-192	-155	-188
	Δg_{yy}	16667	14863	13469	13249	13123	13574
	Δg_{zz}	4940	4477	4312	4247	4052	4681
CH_3	Δg_{xx}	-84	-78	-76	-71	-84	-89
	Δg_{zz}	646	546	545	534	506	649
O_2	Δg_{xx}	-199	-187	-197	-196	-232	-199
	Δg_{zz}	2669	2066	2339	2401	3498	2677
$O_3{}^-$	Δg_{xx}	-706	810	-491	-371	-1502	-555
	Δg_{yy}	18062	26357	16016	17331	23770	18429
	Δg_{zz}	10668	18585	9031	10232	16103	11032
$CO_2{}^-$	Δg_{xx}	840	584	738	716	1048	932
	Δg_{yy}	-5104	-4436	-4400	-4432	-5709	-5122
	Δg_{zz}	-779	-694	-687	-684	-927	-716
H_2CO^+	Δg_{xx}	6172	6100	5613	5724	5806	5910
	Δg_{yy}	144	-168	22	-62	662	24
	Δg_{zz}	721	1573	417	910	3039	91
NO_2	Δg_{xx}	3596	2883	3138	3108	4278	3628
	Δg_{yy}	-11728	-10172	-10352	-10331	-12588	-11837
	Δg_{zz}	-762	-234	-647	-578	-1195	-695
NF_2	Δg_{xx}	-699	-504	-620	-612	-1038	-667
	Δg_{yy}	6704	6370	6270	6155	5757	6988
	Δg_{zz}	3766	3605	3631	3537	2889	4126
$NF_3{}^+$	Δg_{xx}	-2010	-1209	-1707	-1666	-3667	-1806
	Δg_{zz}	5178	5816	5221	5258	4020	5914

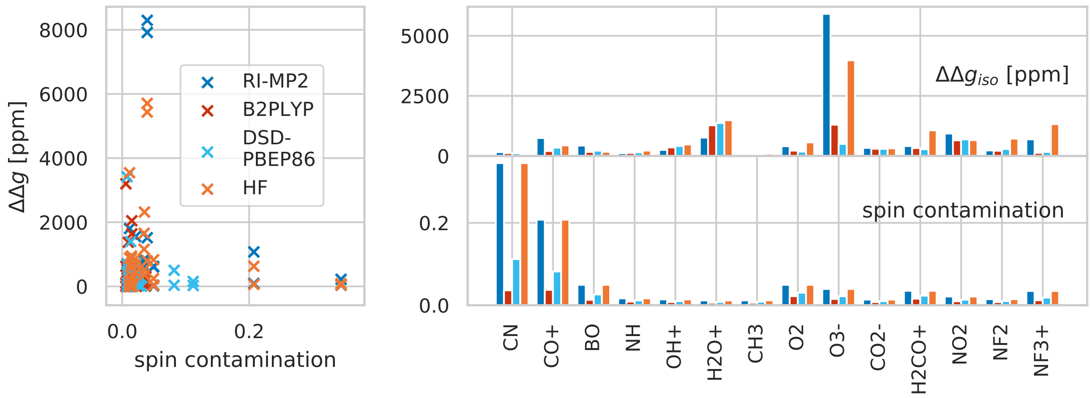

Figure 5.4: Study of the relation between spin contamination and g-shift errors of different methods (RI-MP2, B2PlYP, DSD-PBEP86, HF) with respect to CCSD. On the left column the principle g-shift values are plotted versus the spin contamination whereas the right column shows two bar plots of the isotropic g-shift error (top) and the spin contamination (bottom) for the respective methods for each molecule of the test set.

5.4.4 Computational costs

In the previous section the accuracy of using DHDFT for g-tensor calculations was discussed with regard to experimental and other available computational methods. In this section the computational costs of the implemented method are analyzed and discussed. Four medium to large size molecules were studied using the DSD-PBEP86 DHDF with the def2-TZVPP basis set. The detailed data are given in table 5.4 and visualized in figure 5.5. The total time is split into its main contributions: the SCF part, the CP-SCF part which includes both the assembling of the RHS and the solution of the CP-SCF equations, the computation of the SOC integrals, the formation of the relaxed MP2-density ($\mathbf{D}$) and the relaxed MP2 response density ($\mathbf{D}^B$). It is clearly visible that the computational effort is dominated by the calculation of the MP2 response density. It formally scales as $\mathcal{O}(N^5)$ and therefore can be 20-30 times more expensive than the evaluation of $\mathbf{D}$.[167]

Two different approximations for the two-electron integrals contributions to the Fock matrix are used here. In this section the integrals $(ia|jb)$ and $(ij|ab)$ (and the corresponding other spin integrals) are generated by an RI transformation and stored on disk, denoted RIJK.[165] The results then depend on the speed of disk I/O operations. Here, a RAID 0 hard disk configuration was used. The RIJCOSX notation refers to the RI approximation for the Coulomb integrals and the chain of spheres (COS) approxi-

Table 5.4: Computational timing data of DSD-PBEP86 given in minutes for four medium to large size radicals with N_{atoms}, N_{el}, N_{basis}, $N_{auxbasis}$ and *grid size* being the number of atoms, number of electrons, basis set dimension, auxiliary basis set dimension and grid size for the COSX approximation. The calculations were performed on 8 Intel(R) Xeon(R) CPU E5-2640 v3 2.60 GHz cores with 16 GB RAM per core.

	phenyl		tyrosyl		α-tocopheryl		α-chlorophyll	
N_{atoms}	11		23		80		73	
N_{el}	41		95		239		293	
N_{basis}	256		543		1647		1720	
$N_{auxbasis}$	531		1138		3091		3612	
grid size	11434		23521		68641		136669	
	RIJK	RIJCOSX	RIJK	RIJCOSX	RIJK	RIJCOSX	RIJK	RIJCOSX
SCF	0.1	0.1	0.8	0.5	10.6	4.0	16.4	11.6
CP-SCF	0.3	0.5	1.6	3.2	149.4	36.9	503.3	87.3
SOC	0.5	0.5	2.4	2.4	26.1	26.0	32.2	32.5
$\mathbf{D}$	0.2	0.4	3.6	4.0	654.8	177.4	1675.4	351.0
$\mathbf{D}^B$	2.1	2.0	27.3	24.3	3498.6	3135.4	7845.7	7154.6
total time	3.2	3.6	35.7	34.4	4339.5	3379.8	10073.1	7637.0

mation for the exchange integrals.[166] In this case the RI transformed integrals are not stored on disk but generated in an AO-direct fashion.

A quick overview is provided by comparing the final row in table 5.4 which denotes the total time of each calculation. For the two smaller systems, phenyl and tyrosyl, no distinct differences are observable between both approximations, but for the two larger examples, α-tocopheryl and α-chlorophyll, a clear difference between RIJK and RIJCOSX can be seen where the latter requires less time for the computation. The larger the molecule (with respect to the number of electrons and therefore the number of basis functions) the more distinct is the time difference between the two tested approximations.[76] Therefore, it can be stated that for smaller systems the choice of approximation is non-relevant whereas for larger systems with more than 100 electrons the RIJCOSX approximation is clearly more efficient. For instance, the α-chlorophyll g-tensor calculation with RIJCOSX took about 5 days whereas the RIJK option took 7 days.

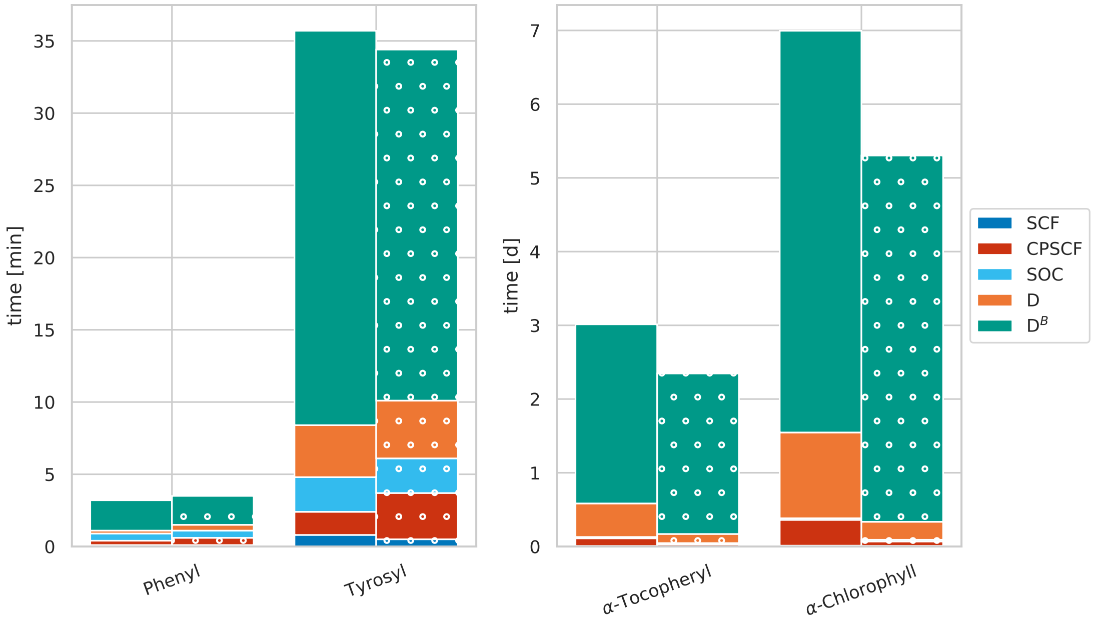

Figure 5.5: Computational performance of DSD-PBEP86 given in minutes for the phenyl and tyrosyl radical, in hours for the α-tocopheryl and α-chlorophyll radical. The timings are shown by stacked bar plots grouped into sets of two for each compound. The total height of each bar refers to the total time whereas each stack refers to corresponding contribution as decoded in the legend. For each compound the left bar (no pattern) refers to the RIJK treatment of the two-electron integrals whereas the right bar (dotted pattern) refers to the RIJ-COSX treatment.

5.5 Conclusion and Outlook

In this chapter we presented an efficient implementation of the electronic g-tensor at MP2 level using GIAOs. The working equations were derived from an unrestricted ansatz. With this scheme the usage of DHDFT was enabled for g-tensor calculations. Our computed g-shift values with pure RI-MP2, B2PLYP and DSD-PBEP86 are in overall reasonable to good agreement with the experimental data whereas pure RI-MP2 performs slightly less well than the DHDFT as is expected for molecular properties. The comparison to other available computational methods shows a clear improvement of DHDFT to pure RI-MP2. Both tested DHDFT, B2PLYP and DSD-PBEP86, give g-shifts close to the CCSD method which was taken as a reference being the up-to-now most accurate computational method available for g-tensor calculations. RI-MP2 performs even worse than HF, but the DHDFT are still outperformed by the hybrid DF B3LYP for the used test set of small radicals. Comparing both tested DHDFT to one another DSD-PBEP86 shows a better performance. The study of the computational costs show that for molecular systems with more than 100 electrons the choice of two-electron integral approximations becomes relevant. Indeed, for small systems RIJK and RIJCOSX marginally differ, but for large systems, e.g., the α-chlorophyll radical, RIJCOSX reduces the computational costs significantly.

We can conclude that DHDFT clearly improves the computational performance for the calculation of the electronic g-tensor compared to pure RI-MP2. Nonetheless, somewhat frustratingly, for the investigated set of small radicals the B3LYP functional still shows slightly better agreement with CCSD. However, it is well known that DFT, up to the hybrid functionals, is still failing in computing accurate g-shifts for transition metal compounds.[47] Therefore, it is of interest to study the performance of DHDFT for the latter group of molecules and make efficient higher level theoretical methods, e.g., CC, available for g-tensor calculations of large molecular systems by using linear scaling correlation approaches.

6 Analytical second order derivatives of OO-(RI-)MP2

The treatment of open shell systems is often not as straightforward as for closed shell systems.[239] The common approach is based on an unrestricted wave function with UHF being the simplest approximation to the SE. One problem that arises with unrestricted wave functions and holds as an indicator for poor performance is spin contamination. In the case of MP2 spin contaminated wave functions can significantly worsen the subsequent correlation correction.[240–245] However, the development of orbital optimized MP2 provides a solution to this problem.[171–173, 246, 247] Due to the improvements upon OO-MP2 for open shell systems and its availability to decent sized molecules it becomes evident to extend this method to higher order response properties for which response densities will be required.

Here, we present a derivation of the *coupled-perturbed orbital optimized MP2* (*CP-OO-MP2*) equations which can be considered as an extension of the CP-SCF equations including MP2 and give access to the OO-MP2 response density. Furthermore, a description of the preliminary implementation into ORCA is outlined.

6.1 The OO-(RI-)MP2 response density

According to the definition of the OO-MP2 density the OO-MP2 response density for a perturbation x becomes

$$\mathbf{D}^{OO,x} = \mathbf{P}^{ref,x} + \mathbf{D}^{MP2,x} \tag{6.1}$$

with the response reference density and response MP2-like density being defined as

$$P_{\mu\nu}^{ref,x} = \sum_i c_{\mu i}^{*x} c_{\nu i} + c_{\mu i}^{*} c_{\nu i}^{x}, \tag{6.2}$$

$$D_{ij}^{B} = \sum_k \left[\frac{1}{2} \left(\left\langle \mathbf{t}^{jk,x} \mathbf{t}^{ki} \right\rangle - \left\langle \mathbf{t}^{jk} \mathbf{t}^{ki,x} \right\rangle \right) + \left\langle \mathbf{t}^{j\bar{k},x} \mathbf{t}^{\bar{k}i} \right\rangle - \left\langle \mathbf{t}^{j\bar{k}} \mathbf{t}^{\bar{k}i,x} \right\rangle \right] = -D_{ji}^{x}, \tag{6.3}$$

$$D_{ab}^{x} = \sum_{ij} \left[\frac{1}{2} \left(\mathbf{t}^{ji,x} \mathbf{t}^{ij} - \mathbf{t}^{ji} \mathbf{t}^{ij,x} \right) + \mathbf{t}^{j\bar{i},x} \mathbf{t}^{\bar{i}j} - \mathbf{t}^{j\bar{i}} \mathbf{t}^{\bar{i}j,x} \right]_{ab} = -D_{ba}^{x}. \tag{6.4}$$

The perturbed MO coefficients $\mathbf{c}^x$, that again are expanded in terms of $\mathbf{U}^x$-coefficients, and the perturbed amplitudes $\mathbf{t}^x$ are both obtained iteratively as the response of the OO-MP2 Lagrangian. This results in a set of linear equations, known as the CP-OO-MP2 equations

$$\begin{pmatrix} \frac{\partial g_{ai}^{x}}{\partial \mathbf{U}^x} & \frac{\partial g_{ai}^{x}}{\partial \mathbf{t}^x} \\ \frac{\partial R_{ab}^{ij,x}}{\partial \mathbf{U}^x} & \frac{\partial R_{ab}^{ij,x}}{\partial \mathbf{t}^x} \end{pmatrix} \begin{pmatrix} \mathbf{U}^x \\ \mathbf{t}^x \end{pmatrix} = \begin{pmatrix} \mathbf{g}_o^x & \mathbf{g}_t^x \\ \mathbf{R}_o^x & \mathbf{R}_t^x \end{pmatrix} \begin{pmatrix} \mathbf{U}^x \\ \mathbf{t}^x \end{pmatrix} = \begin{pmatrix} \mathbf{b}_o^{(x)} \\ \mathbf{b}_t^{(x)} \end{pmatrix}. \tag{6.5}$$

The expressions for the LHS and RHS of equation 6.5 are obtained by taking the derivative of the two stationary conditions as follows

$$\frac{\mathrm{d}g_{ai}}{\mathrm{d}x} = 0, \tag{6.6}$$

$$\frac{\mathrm{d}R_{ab}^{ij}}{\mathrm{d}x} = 0. \tag{6.7}$$

The derivative of the orbital gradient then becomes

$$
\begin{aligned}
\frac{\mathrm{d}g^{\alpha}_{ai}}{\mathrm{d}x} =&2 \left\{ F^{(x)}_{ai} - S^{(x)}_{ai}\epsilon_i - \sum_{jk} S^{(x)}_{jk}(ai||kj) + U^{x}_{ai}(\epsilon_a - \epsilon_i) + \sum_{jb} U^{x}_{bj}\left[(ai||jb) \pm (ai||bj)\right] \right. \\
&+ \sum_{jbc}(ac|jb)t^{ij,x}_{cb} - \sum_{jkb}(ki|jb)t^{kj,x}_{ab} + \sum_{jbc}(ac|jb)^{(x)}t^{ij}_{cb} - \sum_{jkb}(ki|jb)^{(x)}t^{kj}_{ab} \\
&+ \sum_{jbcd}\left[U^{*x}_{da}(dc|jb)t^{ij}_{cb} + U^{x}_{dc}(ad||jb)t^{ij}_{cb}\right] \\
&- \sum_{jklb}\left[U^{x}_{li}(kl|jb)t^{kj}_{ab} + U^{*x}_{lk}(il||bj)t^{kj}_{ab} + S^{(x)}_{jb}(ki|lj)t^{kl}_{ab}\right] \\
&+ \sum_{jkbc}\left[U^{*x}_{kj}(ac|kb)t^{ij}_{cb} - U^{x}_{cb}(ik||jc)t^{kj}_{ab} - S^{(x)}_{ak}(kc|jb)t^{ij}_{cb} - S^{(x)}_{kc}(ak||jb)t^{ij}_{cb}\right] \\
&\pm \sum_{jb} U^{x}_{bj}\left[\sum_{cd}(ac|bd)t^{ij}_{cd} + \sum_{kl}(ik|lj)t^{kl}_{ab} - \sum_{ck}\Big((aj||kc)t^{ik}_{bc} + (ib||ck)t^{jk}_{ac}\Big)\right] \\
&- \sum_{jkbc}\left[U^{x}_{aj}(jc|kb)t^{ik}_{cb} + U^{x}_{bi}(kb|jc)t^{kj}_{ac}\right] \\
&+ \sum_{j} D_{ij}\left[F^{(x)}_{aj} - S^{(x)}_{aj}\epsilon_j - \sum_{kl} S^{(x)}_{kl}(aj||lk)\right] \\
&- \sum_{b} D_{ab}\left[F^{(x)}_{bi} - S^{(x)}_{bi}\epsilon_i - \sum_{kl} S^{(x)}_{kl}(bi||lk)\right] \\
&+ \sum_{j}\left[D^{x}_{ij}F_{aj} + D_{ij}\left(U^{x}_{aj}(\epsilon_a - \epsilon_j) + \sum_{ck} U^{x}_{ck}\left[(aj||kc) \pm (aj||ck)\right]\right)\right] \\
&\left. - \sum_{b}\left[D^{x}_{ab}F_{bi} + D_{ab}\left(U^{x}_{bi}(\epsilon_b - \epsilon_i) + \sum_{ck} U^{x}_{ck}\left[(bi||kc) \pm (bi||ck)\right]\right)\right] \right\} \\
&+ \mathcal{R}\left[\mathbf{D}^{x}\right]_{ai} + \sum_{pq} D_{pq}\left[(pq||ai)^{(x)} + (pq||ia)^{(x)}\right] \\
&- \sum_{j} S^{(x)}_{aj}\mathcal{R}\left[\mathbf{D}\right]_{aj} - \frac{1}{2}\sum_{j}\mathcal{R}\left[\mathbf{D}\right]_{aj} S^{(x)}_{ji} \pm \sum_{b} S^{(x)}_{ab}\mathcal{R}\left[\mathbf{D}\right]_{bi} \\
&\mp \sum_{jkl} S^{(x)}_{jk} D_{kl}[(ai||jl) \pm (ai||lj)] \mp \sum_{bcd} S^{(x)}_{bc} D_{cd}[(ai||bd) \pm (ai||db)] \\
&- 2\sum_{jcd} D_{cd}S^{(x)}_{jc}[(ai||dj) - (ai||jd)] - \sum_{j} U^{x}_{aj}\mathcal{R}\left[\mathbf{D}\right]_{ji} + \sum_{b} U^{x}_{bi}\mathcal{R}\left[\mathbf{D}\right]_{ab} \\
&\pm 2\sum_{bj}\left(\sum_{k} D_{kj}U^{x}_{bk} - \sum_{c} D_{bc}U^{x}_{cj}\right)\left[(ai||bj) \pm (ai||jb)\right].
\end{aligned}
\tag{6.8}
$$

Collecting all terms containing the virtual-occupied $\mathbf{U}^x$-coefficients and the perturbed amplitudes $\mathbf{t}^x$ results in the CP-OO-MP2 orbital LHS

$$\begin{aligned}
&2\Bigg\{U^x_{ai}(\epsilon_a-\epsilon_i)+\sum_{jb}U^x_{bj}\left[(ai||jb)\pm(ai||bj)\right] \\
&+\sum_{jbc}(ac|jb)t^{ij,x}_{cb}-\sum_{jkb}(ki|jb)t^{kj,x}_{ab} \\
&\pm\sum_{jb}U^x_{bj}\left[\sum_{cd}(ac|bd)t^{ij}_{cd}+\sum_{kl}(ik|lj)t^{kl}_{ab}-\sum_{ck}\left((kj|ac)t^{ik}_{bc}+(ik|cb)t^{jk}_{ac}\right)\right] \\
&-\sum_{jkbc}\left[U^x_{aj}(jc|kb)t^{ik}_{cb}+U^x_{bi}(kb|jc)t^{kj}_{ac}\pm U^x_{bj}\left((aj|kc)t^{ik}_{bc}+(bi|kc)t^{jk}_{ac}\right)\right] \\
&+\sum_{j}\left[D^x_{ij}F_{aj}+D_{ij}\left(U^x_{aj}(\epsilon_a-\epsilon_j)+\sum_{ck}U^x_{ck}\left[(aj||kc)\pm(aj||ck)\right]\right)\right] \\
&-\sum_{b}\left[D^x_{ab}F_{bi}+D_{ab}\left(U^x_{bi}(\epsilon_b-\epsilon_i)+\sum_{ck}U^x_{ck}\left[(bi||kc)\pm(bi||ck)\right]\right)\right]\Bigg\} \\
&+\mathcal{R}\left[\mathbf{D}^x\right]_{ai}-\sum_{j}U^x_{aj}\mathcal{R}\left[\mathbf{D}\right]_{ji}+\sum_{b}U^x_{bi}\mathcal{R}\left[\mathbf{D}\right]_{ab} \\
&\pm 2\sum_{bj}\left(\sum_{k}D_{kj}U^x_{bk}-\sum_{c}D_{bc}U^x_{cj}\right)\left[(ai||bj)\pm(ai||jb)\right],
\end{aligned} \tag{6.9}$$

and the RHS becomes

$$\begin{aligned}
\mathbf{b}^{(x)}_o = &-2\Bigg\{F^{(x)}_{ai}-S^{(x)}_{ai}\epsilon_i-\sum_{jk}S^{(x)}_{jk}(ai||kj)+\sum_{jbc}(ac|jb)^{(x)}t^{ij}_{cb}-\sum_{jkb}(ki|jb)^{(x)}t^{kj}_{ab} \\
&+\frac{1}{2}\sum_{jbkl}\left[S^{(x)}_{li}(kl|jb)t^{kj}_{ab}+S^{(x)}_{kl}(il||bj)t^{kj}_{ab}\right]-\frac{1}{2}\sum_{jbcd}\left[S^{(x)}_{ad}(dc|jb)t^{ij}_{cb}+S^{(x)}_{dc}(ad||jb)t^{ij}_{cb}\right] \\
&+\sum_{jbcd}S^{(x)}_{jb}(ki|lj)t^{kl}_{ab} \\
&-\sum_{jkbc}\left[\frac{1}{2}S^{(x)}_{jk}(ac|kb)t^{ij}_{cb}+\frac{1}{2}S^{(x)}_{cb}(ik|jc)t^{kj}_{ab}+S^{(x)}_{ak}(kc|jb)t^{ij}_{cb}+S^{(x)}_{kc}(ak||jb)t^{ij}_{cb}\right] \\
&+\sum_{j}D_{ij}\left[F^{(x)}_{aj}-S^{(x)}_{aj}\epsilon_j-\sum_{kl}S^{(x)}_{kl}(aj||lk)\right] \\
&-\sum_{b}D_{ab}\left[F^{(x)}_{bi}-S^{(x)}_{bi}\epsilon_i-\sum_{kl}S^{(x)}_{kl}(bi||lk)\right]\Bigg\}-\sum_{pq}D_{pq}\left[(pq||ai)^{(x)}+(pq||ia)^{(x)}\right].
\end{aligned} \tag{6.10}$$

Applying the same procedure to the amplitude residual results in the following derivative

$$
\begin{aligned}
\frac{\mathrm{d}R^{ij}_{ab}}{\mathrm{d}x} =& (ai||bj)^{(x)} - \frac{1}{2}\sum_{k}\left[S^{(x)}_{ki}(ak||bj) + S^{(x)}_{kj}(ai||bk)\right] + \frac{1}{2}\sum_{c}\left[S^{(x)}_{ac}(ci||bj) + S^{(x)}_{bc}(ai||cj)\right] \\
& - \sum_{p}\left[S^{(x)}_{ap}(pi||bj) + S^{(x)}_{bp}(ai||pj)\right] \\
& - \sum_{k}\left[U^{x}_{ak}(ki||bj) + U^{x}_{bk}(ai||kj)\right] + \sum_{c}\left[U^{x}_{ci}(ac||bj) + U^{x}_{cj}(ai||bc)\right] \\
& - \sum_{k}\left[t^{ik}_{ab}\left(F^{(x)}_{kj} - \sum_{lm}S^{(x)}_{lm}(kj||ml) - \frac{1}{2}S^{(x)}_{kj}(\epsilon_j + \epsilon_k)\right)\right. \\
& \qquad \left. + t^{kj}_{ab}\left(F^{(x)}_{ki} - \sum_{lm}S^{(x)}_{lm}(ki||ml) - \frac{1}{2}S^{(x)}_{ki}(\epsilon_i + \epsilon_k)\right)\right] \\
& - \sum_{k}\left[t^{ik,x}_{ab}F_{kj} + t^{kj,x}_{ab}F_{ki}\right. \\
& \qquad \left. + t^{ik}_{ab}\sum_{cl}U^{x}_{cl}\left[(kj||lc) \pm (kj||cl)\right] + t^{kj}_{ab}\sum_{cl}U^{x}_{cl}\left[(ki||lc) \pm (ki||cl)\right]\right] \\
& - \sum_{kc}\left[t^{ik}_{ab}\left(U^{x}_{cj}F_{kc} \pm U^{x}_{ck}F_{cj}\right) + t^{kj}_{ab}\left(U^{x}_{ci}F_{kc} \pm U^{x}_{ck}F_{ci}\right)\right] \\
& - \sum_{c}\left[t^{ij}_{ac}\left(F^{(x)}_{cb} - \sum_{lm}S^{(x)}_{lm}(cb||ml) - \frac{1}{2}S^{(x)}_{cb}(\epsilon_b + \epsilon_c)\right)\right. \\
& \qquad \left. + t^{ij}_{cb}\left(F^{(x)}_{ac} - \sum_{lm}S^{(x)}_{lm}(ac||ml) - \frac{1}{2}S^{(x)}_{ac}(\epsilon_c + \epsilon_a)\right)\right] \\
& - \sum_{kc}\left[t^{ij}_{ac}S^{(x)}_{ck}F_{kb} + t^{ij}_{cb}S^{(x)}_{ak}F_{kc} + t^{ij}_{ac}F_{ck}S^{(x)}_{kb} + t^{ij}_{cb}F_{ak}S^{(x)}_{kc}\right] \\
& - \sum_{c}\left[t^{ij,x}_{ac}F_{cb} + t^{ij,x}_{cb}F_{ac}\right. \\
& \qquad \left. + t^{ij}_{ac}\sum_{dl}U^{x}_{dl}\left[(cb||ld) \pm (cb||dl)\right] + t^{ij}_{cb}\sum_{dl}U^{x}_{dl}\left[(ac||ld) \pm (ac||dl)\right]\right] \\
& + \sum_{kc}\left[t^{ij}_{ac}\left(U^{x}_{ck}F_{kb} \pm F_{ck}U^{x}_{bk}\right) + t^{ij}_{cb}\left(U^{x}_{ak}F_{kc} \pm F_{ak}U^{x}_{ck}\right)\right].
\end{aligned}
\tag{6.11}
$$

The CP-OO-MP2 amplitude LHS can be then written as

$$
\begin{aligned}
&-\sum_k \left[U^x_{ak}(ki||bj) + U^x_{bk}(ai||kj)\right] + \sum_c \left[U^x_{ci}(ac||bj) + U^x_{cj}(ai||bc)\right] \\
&-\sum_k \left[t^{ik}_{ab}\mathcal{R}^{\pm}\left[\mathbf{U}^x\right]_{kj} + t^{kj}_{ab}\mathcal{R}^{\pm}\left[\mathbf{U}^x\right]_{ki}\right] + \sum_c \left[t^{ij}_{ac}\mathcal{R}^{\pm}\left[\mathbf{U}^x\right]_{cb} + t^{ij}_{cb}\mathcal{R}^{\pm}\left[\mathbf{U}^x\right]_{ac}\right] \\
&-\sum_{kc} \left[t^{ik}_{ab}\left(U^x_{cj}F_{kc} \pm U^x_{ck}F_{cj}\right) + t^{kj}_{ab}\left(U^x_{ci}F_{kc} \pm U^x_{ck}F_{ci}\right)\right] \\
&+\sum_{kc} \left[t^{ij}_{ac}\left(U^x_{ck}F_{kb} \pm F_{ck}U^x_{bk}\right) + t^{ij}_{cb}\left(U^x_{ak}F_{kc} \pm F_{ak}U^x_{ck}\right)\right] \\
&-\sum_k \left[t^{ik,x}_{ab}F_{kj} + t^{kj,x}_{ab}F_{ki}\right] - \sum_c \left[t^{ij,x}_{ac}F_{cb} + t^{ij,x}_{cb}F_{ac}\right],
\end{aligned}
\tag{6.12}
$$

and the RHS becomes

$$
\begin{aligned}
\mathbf{b}^{(x)}_t = &-(ai||bj)^{(x)} + \frac{1}{2}\sum_k \left[S^{(x)}_{ki}(ak||bj) + S^{(x)}_{kj}(ai||bk)\right] - \frac{1}{2}\sum_c \left[S^{(x)}_{ac}(ci||bj) + S^{(x)}_{bc}(ai||cj)\right] \\
&+\sum_p \left[S^{(x)}_{ap}(pi||bj) + S^{(x)}_{bp}(ai||pj)\right] \\
&+\sum_k \Bigg[t^{ik}_{ab}\left(F^{(x)}_{kj} - \overline{\mathcal{R}}\left[\mathbf{S}^{(x)}\right]_{kj} - \frac{1}{2}S^{(x)}_{kj}(\epsilon_j + \epsilon_k)\right) \\
&\qquad t^{kj}_{ab}\left(F^{(x)}_{ki} - \overline{\mathcal{R}}\left[\mathbf{S}^{(x)}\right]_{ki} - \frac{1}{2}S^{(x)}_{ki}(\epsilon_i + \epsilon_k)\right)\Bigg] \\
&-\sum_c \Bigg[t^{ij}_{ac}\left(F^{(x)}_{cb} - \overline{\mathcal{R}}\left[\mathbf{S}^{(x)}\right]_{cb} - \frac{1}{2}S^{(x)}_{cb}(\epsilon_b + \epsilon_c)\right) \\
&\qquad t^{jj}_{bc}\left(F^{(x)}_{ac} - \overline{\mathcal{R}}\left[\mathbf{S}^{(x)}\right]_{ac} - \frac{1}{2}S^{(x)}_{ac}(\epsilon_a + \epsilon_c)\right)\Bigg] \\
&-\sum_{ck} \left[t^{ij}_{ac}S^{(x)}_{ck}F_{kb} + t^{ij}_{cb}S^{(x)}_{ak}F_{kc} + t^{ij}_{ac}F_{ck}S^{(x)}_{kb} + t^{ij}_{cb}F_{ak}S^{(x)}_{kc}\right].
\end{aligned}
\tag{6.13}
$$

The response terms are defined as follows

$$\mathcal{R}\left[\mathbf{D}\right]_{pq} = \sum_{rs} D^{x}_{rs}\left[(pq||rs) + (pq||rs)\right], \tag{6.14}$$

$$\overline{\mathcal{R}}\left[\mathbf{S}^{(x)}\right]_{ij} = \sum_{kl} S_{kl}(ij||lk), \tag{6.15}$$

$$\mathcal{R}^{\pm}\left[\mathbf{U}^{x}\right]_{pq} = \sum_{ck} U^{x}_{ck}\left[(pq||kc) \pm (pq||ck)\right]. \tag{6.16}$$

In case of perturbation independent basis functions all terms including the perturbed overlap vanish. Thus, the equations 6.10 and 6.13 become

$$\mathbf{b}_{o}^{(x)} = 2\left\{h^{(x)}_{ai} + \sum_{j} D_{ij}h^{(x)}_{aj} - \sum_{b} D_{ab}h^{(x)}_{bi}\right\}, \tag{6.17}$$

$$\mathbf{b}_{t}^{(x)} = \sum_{c}\left[t^{ij}_{ac}h^{(x)}_{cb} + t^{ij}_{cb}h^{(x)}_{ac}\right] - \sum_{k}\left[t^{ik}_{ab}h^{(x)}_{kj} + t^{kj}_{ab}h^{(x)}_{ki}\right]. \tag{6.18}$$

Nonetheless it is apparent that the solution of the CP-OO-MP2 equations is significantly more expensive than the solution of the CP-SCF equations.

6.2 Implementation details

Equations 6.10, 6.13, 6.9 and 6.12 display the working equations for the CP-OO-MP2 routine. While the orbital and amplitude RHS is constructed similar to algorithm 1 the LHS is considerably more demanding than the CP-SCF LHS. Instead of computing and storing a full "Hessian" the *sigma vector* is calculated. This "sigma build" is separated into three subroutines, namely

- `calc_sigma_orborb()`: $\sigma_{oo} = \mathbf{g}_{o}^{x}\,\mathbf{U}^{x}$,
- `calc_sigma_orbamp()`: $\sigma_{ot} = \mathbf{g}_{t}^{x}\,\mathbf{t}^{x}$,
- `calc_sigma_amp()`: $\sigma_{t} = \mathbf{R}_{o}^{x}\,\mathbf{U}^{x} + \mathbf{R}_{t}^{x}\,\mathbf{t}^{x}$.

Collecting the related terms of equation 6.9 for `calc_sigma_orborb()` and applying the RI approximation results in

$$
\begin{aligned}
\sigma_{oo} =& 2\left\{U^x_{ai}(\epsilon_a - \epsilon_i) + \mathcal{R}^{\pm}\left[\mathbf{U}^x\right]_{ai}\right. \\
&+ \sum_j \left[D_{ij}\left(U^x_{aj}(\epsilon_a - \epsilon_j) + \mathcal{R}^{\pm}\left[\mathbf{U}^x\right]_{aj}\right)\right] - \sum_b \left[D_{ab}\left(U^x_{bi}(\epsilon_b - \epsilon_i) + \mathcal{R}^{\pm}\left[\mathbf{U}^x\right]_{bi}\right)\right] \\
&\pm \sum_{jb} U^x_{bj}\, \mathrm{MOIntT}_{ijab} \\
&\left. - \sum_{jkbcP}\left[U^x_{aj}B^P_{jb}\Gamma^P_{ib} + U^x_{bi}B^P_{jb}\Gamma^P_{ja} \pm U^x_{bj}\left(B^P_{ja}\Gamma^P_{ib} + B^P_{ib}\Gamma^P_{ja}\right)\right]\right\} \\
&- \sum_j U^x_{aj}\mathcal{R}\left[\mathbf{D}\right]_{ji} + \sum_b U^x_{bi}\mathcal{R}\left[\mathbf{D}\right]_{ab} \pm 2\mathcal{R}^{\pm}\left[\mathbf{U}^x\mathbf{D}_{OO} - \mathbf{D}_{VV}\mathbf{U}^x\right]_{ai},
\end{aligned}
\tag{6.19}
$$

with the amplitude contracted MO integrals being[1]

$$
\mathrm{MOIntT}_{ijab} = \left[\sum_{cd}(ac|bd)t^{ij}_{cd} + \sum_{kl}(ik|lj)t^{kl}_{ab} - \sum_{ck}\left((kj|ac)t^{ik}_{bc} + (ik|cb)t^{jk}_{ac}\right)\right]. \tag{6.20}
$$

The remaining terms of equation 6.9 contribute to the `calc_sigma_orbamp()` subroutine according to

$$
\sigma_{ot} = 2\left\{\sum_{jbc}(ac|jb)t^{ij,x}_{cb} - \sum_{jkb}(ki|jb)t^{kj,x}_{ab} + \sum_j D^x_{ij}F_{aj} - \sum_b D^x_{ab}F_{bi}\right\} + \mathcal{R}\left[\mathbf{D}^x\right]_{ai}, \tag{6.21}
$$

with $\mathbf{D}^x$ being rebuild in each iteration with the current perturbed amplitudes $\mathbf{t}^x$. For the `calc_sigma_amp()` subroutine equation 6.12 can be further simplified to

---

[1] Note that the MO integral containers are all calculated using the RI approximation. Notation is skipped here for clarity.

$$
\begin{aligned}
\sigma_t = & -\sum_k \left[U^x_{ak}\,\mathrm{MOInt}_{kibj} + U^x_{bk}\,\mathrm{MOInt}_{aikj}\right] + \sum_c \left[U^x_{ci}\,\mathrm{MOInt}_{acbj} + U^x_{cj}\,\mathrm{MOInt}_{aibc}\right] \\
& -\sum_k \left\{ t^{ik}_{ab} \left(\mathcal{R}^{\pm}\left[\mathbf{U}^x\right]_{kj} + \left[\mathbf{F}_{OV}\mathbf{U}^x \pm \mathbf{U}^{xT}\mathbf{F}_{VO}\right]_{kj} \right) \right. \\
& \qquad \left. t^{kj}_{ab} \left(\mathcal{R}^{\pm}\left[\mathbf{U}^x\right]_{ki} + \left[\mathbf{F}_{OV}\mathbf{U}^x \pm \mathbf{U}^{xT}\mathbf{F}_{VO}\right]_{ki} \right) \right\} \\
& +\sum_c \left\{ t^{ij}_{ac} \left(\mathcal{R}^{\pm}\left[\mathbf{U}^x\right]_{cb} + \left[\mathbf{U}^x\mathbf{F}_{VO} \pm \mathbf{F}_{VO}\mathbf{U}^{xT}\right]_{cb} \right) \right. \\
& \qquad \left. t^{ij}_{cb} \left(\mathcal{R}^{\pm}\left[\mathbf{U}^x\right]_{ac} + \left[\mathbf{U}^x\mathbf{F}_{VO} \pm \mathbf{F}_{VO}\mathbf{U}^{xT}\right]_{ac} \right) \right\} \\
& + t^{ij,x}_{ab}(\epsilon_a + \epsilon_b - \epsilon_i - \epsilon_j),
\end{aligned}
\tag{6.22}
$$

Algorithm 2 depicts the preliminary implemenation of the *coupled-perturbed orbital optimized RI-MP2* (*CP-OO-RI-MP2*) routine into ORCA with these considerations in mind.

```
begin
    prepare()
    · make or read $\mathbf{P}^{ref}, \mathbf{F}, \mathbf{D}, \mathcal{R}[\mathbf{D}]$
    · make and store all $B^P$ and $B^{P,x}$
    · make and store all amplitudes $\mathbf{t}$
    · make and store MOInt and MOIntT

    calc_RHS()
    · calc and store RHSs $\mathbf{b}_o^{(x)}$ and $\mathbf{b}_t^{(x)}$

    while not converged do
        solve_linear_equations()
        · make orbital and amplitude trial vectors $\mathbf{U}^x, \mathbf{t}^x$
        · calculate sigma vectors: calc_sigma_orborb(), calc_sigma_orbamp(),
          calc_sigma_amp()
        · iterate
    end

    · form perturbed reference density $\mathbf{P}^{(x)}$
    · form perturbed MP2-like density $\mathbf{D}^{(x)}$
    · complete response OO-RI-MP2 density $\mathbf{D}^{OO,(x)}$
end
```

Algorithm 2: Pseudocode of the CP-OO-RI-MP2 equations in ORCA.

Part III

Application studies

7 Effects of solvation on EPR parameters of nitroxides

7.1 Outline of collaboration

The studies within this chapter are part of an ongoing joint project within the RESOLV Excellence Cluster 2033. This project aims at the investigation of solvation effects on EPR properties of a specific nitroxide, called *(3R,4S)-2,2,3,4,5,5-hexamethylimidazolidin-1-oxyl* (*HMI*) and depicted in 7.1, in aqueous solution. The interdisciplinary team accounts for expertise of different fields within experiment and theory:

- experiment: Enrica Bordignon and Laura Galazzo from University of Geneva (prior Ruhr University Bochum), Alexander Schnegg and Markus Teucher from the Max-Planck-Institute for Chemical Energy Conversion,
- AIMD Dominik Marx and Bikramjit Sharma from Ruhr University Bochum,
- *embedded cluster reference interaction site model* (*EC-RISM*) Stefan M. Kast and Tim Pongratz from Technische Universität Dortmund,
- *quantum chemistry* (*QC*) Frank Neese and Van Anh Tran from the Max-Planck-Institut für Kohlenforschung.

Our part within this joint project were the accurate quantum chemical calculations of the EPR properties under investigation, i.e., the g- and A-tensor, applying state of the art *quantum mechanics* (*QM*) methods for which we developed a suitable *quantum mechanics/molecular mechanics* (*QM/MM*) protocol. All snapshots were provided by Bikramjit Sharma, who conducted the AIMD simulation for the studies presented within this chapter. The theoretical findings were gauged against the experiment which serves as the true reference. The experimental measurements were conducted, and their results were provided by Laura Galazzo and Markus Teucher.

This chapter covers the following topics: First, we report our careful investigation of the technical settings to accurately predict the EPR parameters in aqueous solution by focusing on the A-tensor of HMI in section 7.3. Subsequently, we compare our prediction of the full EPR spectrum for HMI to the experimental measurements, see section 7.4. In section 7.5 we fully focus on the g-tensor and present our investigation on the g-strain phenomenon of HMI.

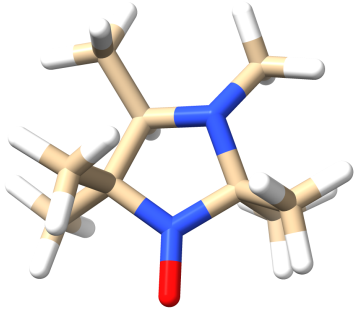

Figure 7.1: (3*R*,4*S*)-2,2,3,4,5,5-hexamethylimidazolidin-1-oxyl (HMI).

7.2 Computational and analysis details

7.2.1 Single point property calculations

All *single point* (*SP*) calculations were conducted using a development version of ORCA 4.2/ORCA 5.0 quantum chemistry program package[136–138]. A-tensors/HFCCs for the ^{14}N isotope were calculated at revPBE0[248]/def2-TZVPP-decontracted-s and DLPNO-CCSD/def2-TZVPP-decontracted-s level, where the s-functions of the used Ahlrichs basis set[236] are decontracted as denoted by "decontracted-s". Tight convergence thresholds, no frozen core approximation and the RIJK approximation for the two-electron integrals were applied. For the DLPNO-CCSD calculations, the correlation auxiliary basis set was chosen to be cc-PWCVTZ/C[249], and the parameters for a special treatment of the core region in the DLPNO scheme was set according to the "Default2" settings in reference [197]. These settings are based on the detailed study of generating accurate spin densities for first-order property calculations such as HFCCs at the DLPNO-CCSD level. G-tensors were computed at revPBE0/def2-TZVPP-decontracted-s level applying tight convergence thresholds, no frozen core approximation and the RIJK approximation for the two-electron integrals.

For the QM/MM approach, the full solvation structures as provided by the AIMD snapshots by Bikramjit Sharma were separated into a QM and *molecular mechanics* (*MM*) subsystem. The QM subsystem contains the whole nitroxide spin label HMI and all water molecules up to the second solvation shell and is therefore treated at revPBE0 and DLPNO-CCSD level, respectively. The MM subsystem contains all remaining water molecules of the snapshot which are included as point charges of the TIP3P water model[250] by placing the corresponding parameters at the position of the water oxygen and hydrogen sites. In this way, the MM region accounts for the electrostatic field of the solvent.

The vertically desolvated data were obtained by removing all water molecules prior to the SP calculation, whereas the vacuum data were used as obtained directly from the gas phase trajectory. An overview of the different data sets is given in table 7.1.

The computer timings provided are based on running the calculations on 8 Intel Xeon E5-2690v2 3.0 GHz cores with a 6 GB RAM per core.

Table 7.1: Overview of the different ensembles regarding the incorporation of the environment for the SP calculation (QM/MM = HMI including water molecules up to second solvation shell in QM region, remaining water molecules as point charges in MM region (see section 7.3 for a detailed analysis resulting in this scheme), vertically desolvated = removing all water molecules from each snapshot prior to the SP calculation, vacuum = no environment due to gas phase simulation), the total number of snapshots extracted from the AIMD and the methods used to compute the g- and A-values of the given ensembles. The prefixes "Solv" and "Vac" refer to the AIMD simulation of HMI in (explicit) water and gas phase respectively.

ensemble	environment	number of snapshots	method g-values	method A-values
Solv-Set400-QM/MM	QM/MM	400	revPBE0	DLPNO-CCSD
Solv-Set1000-QM/MM	QM/MM	1000	revPBE0	revPBE0
Solv-Set400-vd	vertically desolvated	400	revPBE0	DLPNO-CCSD
Solv-Set1000-vd	vertically desolvated	1000	revPBE0	revPBE0
Vac-Set1000	vacuum	1000	revPBE0	revPBE0

7.2.2 Workflow of data generation and spectrum simulation

The workflow for the whole study is depicted in figure 7.2. The generation of theoretical EPR data as shown by the first two boxes are based on the AIMD trajectories. A snapshot was extracted every 200 fs or 500 fs, i.e. giving two ensembles of either 400

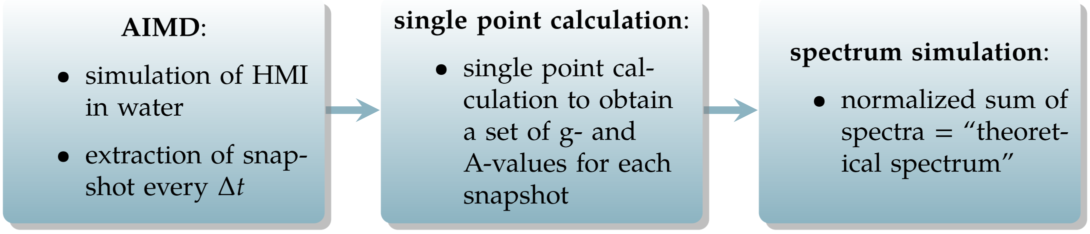

Figure 7.2: Visualization of the workflow that results in what is referred to as "theoretical spectrum" in the text with $\Delta t = 200$ fs for set1000 and $\Delta t = 500$ fs for set400.

snapshots or 1000 snapshots in total.[1] For each of these snapshots a SP property calculation as described in subsection 7.2.1 was conducted and gave a set of g- and A-values. An overview of the methods used for the different ensembles is given in table 7.1. For each snapshot an EPR spectrum was simulated using the "pepper" routine of EasySpin software[219] with an inhomogeneous Gaussian linewidth of 0.6 mT/17 MHz as estimated by the experimental X-band EPR spectrum. Multifrequency EPR spectra were calculated with the same microwave frequencies as used in the experimental measurements:

- X-band: 9.7671 GHz,
- Q-band: 33.6615 GHz,
- W-band: 93.993 GHz,
- J-band: 262.8436 GHz.

The normalized sum of all single spectra for a given ensemble resulted in the "theoretical spectrum" (last box of workflow).

7.2.3 Theoretical EPR data analysis

The theoretical multicomponent approach to simulate the EPR spectra is based on the H-bond analysis along the solvated AIMD trajectory. For this purpose the trajectory was separated into H-bond subensembles using the same H-bonding criterion as parameterized and used previously for pure bulk water[251] according to

---

[1] The AIMD trajectories were generated by Bikramjit Sharma for HMI in vacuum (Vac-SetXXX) and HMI in aqueous solution (Solv-SetXXX). He provided the snapshots for the described ensembles.

$$r_{O\cdots H} < 1.71\cos\theta + 1.37 \tag{7.1}$$

with $r_{O\cdots H}$ being the distance between HMI's nitroxy-oxygen and water hydrogen and θ being the angle formed between the nitroxy-oxygen, H-bonded water hydrogen and water oxygen as visualized in figure 7.3. This H-bond analysis of the solvated AIMD trajectory was performed by Bikramjit Sharma, who then provided the number of H-bonds formed for each snapshot for further investigation.

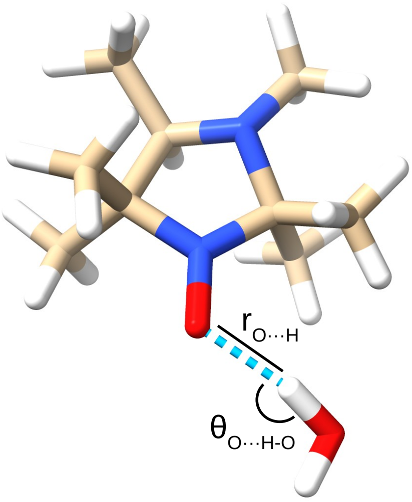

Figure 7.3: Visualization of HMI with one H-bonded water.

For each of the subensembles the mean g- and A-values, i.e., averaged over the snapshots of the corresponding H-bond subensemble, were determined to simulate a spectrum for each subensemble. Those spectra are denoted "***TComp#***" with the number # referring to the corresponding number of H-bonds in the respective subensemble. The simulated spectrum is the weighted sum of the ***TComp#*** spectra. The weights used in the simulations are derived from the population analysis of the different H-bond subensembles along the AIMD trajectory.

7.2.4 Theoretical g-strain analysis

For comparison with the experimentally obtained SH parameters and the g-strain analysis the obtained spectra based on the described workflow were subsequently treated completely analogously to the experimental spectra, i.e., simulations using the "pepper" routine in EasySpin[219] were performed based on a multicomponent ansatz to fit the theoretical spectrum and in this way extract the orientation dependent ALW as a function of the microwave frequency. The ALW was obtained by fitting the orientation dependent "H-Strain" parameter as specified in EasySpin.[219] According to equation 4.1 the field dependent component of the ALW was extracted using a field independent linewidth of 17 MHz as estimated by experiment and subjected to a linear regression fit through the origin. The slope of the linear regression serves as a quantification of the g-strain.

7.3 Accurate prediction of HMI's HFCCs in water

7.3.1 Electronic structure calibration in vacuum

One part of this study was to accurately compute EPR parameters with state-of-the-art-methods, i.e., using coupled cluster methods, in particular DLPNO-CCSD, for computing the HFCCs. Therefore, we first had to assess in how far chosen computational parameters have an impact on the DLPNO-CCSD calculations. We performed an extensive benchmark of these parameters on the HMI molecule which was optimized in vacuum at revPBE0/def2-TZVPP level. The evaluation of the technical setup was separated into three steps, focusing on one parameter at a time: (1) basis set, (2) auxiliary basis set, and (3) property settings. The data of this optimization study is compiled in tables 7.2, 7.3 and 7.4, respectively.

Distinct differences between the double-ζ and triple-ζ basis sets are shown by the values in table 7.2, whereas the change from triple-ζ to quadruple-ζ is rather small with a drop by only 1 MHz or less. This lies within the fundamental error of the method itself. The values obtained with the quadruple-ζ basis set can therefore be considered very close to the complete basis set limit. Furthermore, HFCCs are very sensitive to the description of the core region. This renders a full electron treatment, i.e. no frozen core approximation, crucial for the calculation of this property. Additionally, this leads to the observation of a distinct difference of the HFCCs between the contracted and decontracted-s scheme for the def2 basis sets, whereas the difference between decontracted-s and decontracted-b is fairly small. Note that the difference between the contracted and decontracted schemes is not as pronounced for the cc-PCVXZ basis sets since they already describe the core region more rigorously by including core polarization functions. This is also the reason for the small improvement when going from cc-PCVDZ to cc-PCVTZ compared to the analogous change of the def2-basis sets. In terms of balancing computational cost and accuracy most efficiently, it can be concluded that the def2-TZVPP basis set with decontracted s-functions in combination with the cc-PWCVTZ/C auxiliary basis set and an all electron treatment as well as the "Default2" property settings according to reference [197] gives the best results for the HFCCs computation (see table 7.4) using DLPNO-CCSD. It reproduces the most accurate results obtained with a very large, decontracted basis set including core polarization functions (decontracted-b cc-PCVQZ) with a remarkable accuracy of 0.1 MHz. Simultaneously, a speedup in timings is achieved that are about 20 times faster. This technical setting is thus used for all subsequent calculations at DLPNO-CCSD level reported in the following.

Table 7.2: Basis set convergence study for DLPNO-CCSD calculations of the nitroxy nitrogen A_{iso} parameter of HMI. A full electron treatment was applied, the auxiliary basis set was fixed while different contraction schemes of the basis functions were tested: contracted = contraction of the whole basis set, decontracted-s = decontracted s-functions of the basis set, decontracted-b = decontraction of the whole basis set.

basis set	contraction scheme	time		A_{iso}(N) [MHz]
def2-SVP	contracted	29	min	65.4
	decontracted-s	56	min	25.5
	decontracted-b	63	min	24.7
def2-TZVPP	contracted	4.8	h	27.1
	decontracted-s	7.1	h	29.6
	decontracted-b	12.4	h	29.5
def2-QZVPP	contracted	1.9	d	29.6
	decontracted-s	2.7	d	29.1
	decontracted-b	3.6	d	29.7
cc-PCVDZ	contracted	48	min	24.1
	decontracted-s	78	min	30.0
	decontracted-b	99	min	28.7
cc-PCVTZ	contracted	12.4	h	28.5
	decontracted-s	16.1	h	29.3
	decontracted-b	15.8	h	29.5
cc-PCVQZ	contracted	4.1	d	30.1
	decontracted-s	4.7	d	29.8
	decontracted-b	5.1	d	29.5

Table 7.3: Auxiliary basis set study of the nitroxy nitrogen A_{iso} parameter of HMI using def2-TZVPP with decontracted s-functions, full electron treatment and DLPNO-HFC1[a].

auxbasis	time [h]	A_{iso}(N) [MHz]
autoaux	9.7	29.6
cc-PWCVTZ/c	7.1	29.6
def2-TZVPP/c	7.1	29.4

[a] The DLPNO-HFC1 setting corresponds to the "Default1" DLPNO-CCSD settings for accurate spin densities of reference [197].

Table 7.4: Property setting study of the nitroxy nitrogen A_{iso} parameter of HMI using def2-TZVPP with decontracted s-functions, cc-PWCVTZ/c with DLPNO-HFC1 corresponding to the "Default1" setting and DLPNO-HFC2 to the "Default2" setting of reference [197].

property setting	time [h]	A_{iso}(N) [MHz]
DLPNO-HFC1	7.1	29.6
DLPNO-HFC2	15.6	30.1

7.3.2 Electronic structure calibration with explicit solvation

In order to calculate the EPR parameters of HMI in water for a large amount of configurations/snapshots that contain a large number of explicit water molecules an approximate model is required. Since the whole system of the AIMD simulation cell consists of the nitroxide and all solvating water molecules, it is simply not feasible to treat this full system at DLPNO-CCSD level for a production run. We have therefore decided to apply a QM/MM model where only the most relevant water molecules along with HMI are treated including the full electronic structure (QM), while all remaining solvent molecules are included as point charges (MM) of the TIP3P water model at the proper positions as given by the respective snapshot. However, some reference system was needed that allows the benchmark of the QM/MM approximation to decide a criterion for choosing water molecules to be included in the QM subsystem in the first place. Thus, two independent random snapshots of HMI in water were chosen from AIMD simulations as the reference systems which were fully treated at DLPNO-CCSD level. A sample snapshot of one reference system is shown in figure 7.4. Each of these reference systems contains 415 atoms in total, of which 31 belong to the nitroxide and the rest belongs to water, i.e. 128 water molecules. We denote these two reference systems as "reference system I" and "reference system II".[2] Calculations of the two A_{iso} parameters were conducted for both reference systems applying the resulting technical setup as worked out in section 7.3.1. Each calculation took 65 days on 8 Intel(R) Xeon(R) CPU E5-2687W v4 3.0 GHz cores with a 42 GB RAM per core. The resulting HFCC of the nitroxy nitrogen for this setup, called "HMI + full solvation", was 44.3 and 45.2 MHz for reference system I and reference system II, respectively. These are the reference values to be compared to in the following when assessing the QM/MM approximation. We note that such close agreements between the chosen random snapshots and the experimental value of (44.87 ± 0.14) MHz [1] is fortuitous. The realistic approach is to compare the ensemble averaged value of A_{iso} with that of the experimental result using a well-defined QM/MM treatment of the explicit solvent model as follows. With the reference systems available, we then varied the number of water molecules that are included in the QM subsystem. We anticipate that A_{iso} approaches the value obtained for the reference system in the asymptotic limit of including more and more water molecules in the QM subsystem. Hence, we extracted HMI together with a certain number of water molecules from the reference system to build systematically improvable approximations. In one setup the water molecules of the first solvation shell (HMI + first solvation shell) were included whereas in the other setup all water molecules up to the second solvation shell were included in the QM region (HMI + second solvation shell). All the remaining water molecules were treated in the MM region as electrostatic point charges of the TIP3P water model. For the sake of demonstration, a QM region consisting solely of bare HMI itself was considered as well, being fully embedded in the field of point charges (HMI + no solvation shell). Sample snapshots of these different QM/MM schemes are shown in figure 7.5. The computed HFCCs for the nitroxy nitrogen of HMI are presented in table 7.5 for three different QM/MM models compared to the "full solvation" reference model. Comparing the A_{iso} values obtained with the QM/MM model consisting of only HMI in the QM region versus using the optimized structure of HMI in vacuum, "gas phase" structure, clearly shows that the purely electrostatic embedding of the nitroxide in the solution already accounts for the majority of the shift of the nitroxy nitrogen when switching from vacuum to solvated conditions. Adding the explicit first and second solvation shell(s) to the QM region has less of an impact, but nonetheless is non-negligible

---

[2] Note that the reference systems were taken directly from the AIMD trajectory without resorting to spherical snapshots as has been done for the established workflow. The sole objective here was to chose two reference systems as a benchmark for the QM region for which the directly extracted snapshots already contain sufficient water molecules.

regarding the desired accuracy. Simultaneously, the computational effort is reduced from 65 days to roughly 1 day when going from the full DLPNO-CCSD calculation in the "full solvation" setup to the corresponding QM/MM approximation while not sacrificing any accuracy.

Table 7.5: Calculation of the A_{iso} parameter of the nitroxy N of HMI in water based on the reference snapshot configurations I and II. The QM/MM DLPNO-CCSD property calculations were conducted using different QM regions regarding the inclusion up to the nth solvation shell. The experimentally measured value is (44.87 ± 0.14) MHz.[1]

QM region	reference system	time [h]	$A_{iso}(^{14}N)$ [MHz]	$\Delta_{ref}(^{14}N)$ [MHz]	# H_2O
HMI + full solvation	reference system I	1560	44.3		128
	reference system II	1200	45.2		128
HMI + no solvation shell	reference system I	11*	42.4	1.9	0
	reference system II	16*	44.8	0.4	0
HMI + first solvation shell	reference system I	15*	44.1	0.2	2
	reference system II	19*	44.8	0.4	1
HMI + second solvation shell	reference system I	36**	44.3	0.0	12
	reference system II	39**	45.1	0.1	16

$\Delta_{ref} = |A_{iso}^{HMI+full\ solvation} - A_{iso}^{HMI+reduced\ solvation}|$ where "reduced solvation" refers to no, first and second solvations shell respectively; * calculated on 8 cores, ** calculated on 16 cores.

7.3.3 Summary of calibration studies

In summary, our calibration study has proven most reliable for the QM/MM scheme which contains the HMI molecule including all water molecules up to the second solvation shell around the nitroxy oxygen in the QM region, whereas all remaining water molecules of the corresponding snapshot are treated as TIP3P point charges. Thus, all calculations of the EPR parameters within the solvated data sets were conducted by using this QM/MM scheme combined with the def2-TZVPP/decontraced-s basis set and the electronic structure method as specified.

7.3.4 Statistical evaluation

The electronic structure calibration studies showed good agreement with the experimentally measured value of (44.87 ± 0.14) MHz [1] for the A_{iso} value of the nitroxy nitrogen. Despite testing for two randomly picked snapshots along the trajectory, we know that this good agreement can be serendipitous. The experiment[3] is conducted at ambient conditions and therefore gives an average value obtained from all the molecules

---

[3] A_{iso} obtained by means of X-band *continuous wave* (*cw*)-EPR measurement at 295 K. [1]

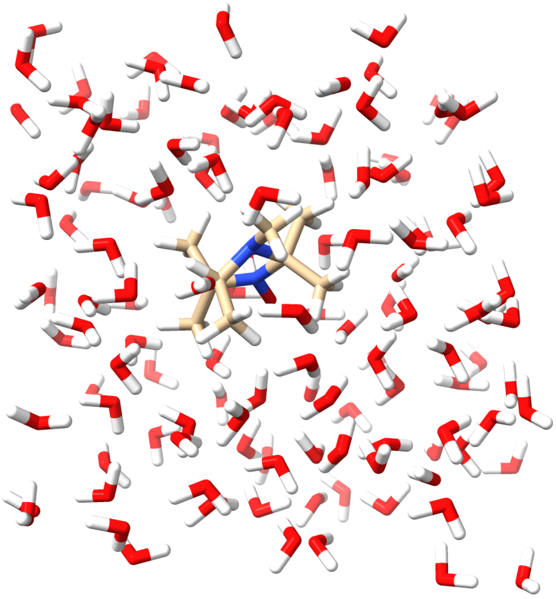

Figure 7.4: Snapshot of a reference system that is fully treated at DLPNO-CCSD level.

within the sample. Consequently, a fair comparison between experiment and theory is thermally averaged computed A_{iso} obtained from the ensembles of the AIMD trajectory. The distribution of the A_{iso} value for SolvSet400 and SolvSet1000 are shown in figure 7.6. The upper row compares the distributions obtained by the different levels of theories, namely revPBE0 and DLPNO-CCSD, applying the established QM/MM model on the snapshots of the solvated ensembles. Foremost it is noticeable that the distribution is fairly broad and does not represent a normal distribution. It arises from both the structural fluctuations of HMI itself and the water molecules of the environment. Comparing both methods however makes the improvement by using higher level theory, i.e., DLPNO-CCSD, for the HFCCs very clear. The deviation to the experimental values is decreased by 3.8 MHz from 8.2 MHz to 4.4 MHz, resulting in a thermally averaged A_{iso} for HMI in aqueous solution of 40.5 MHz. These numbers are visualized by the smaller gap between the vertical blue line (mean value of the underlying distribution) and the vertical red line (experimental value). The mean values of the distributions in figure 7.6 are summarized in table 7.6.

In addition to the solvated ensembles, we have investigated the so-called “vertically desolvated” ensembles. Here, we account for solely the thermal effects, meaning in-

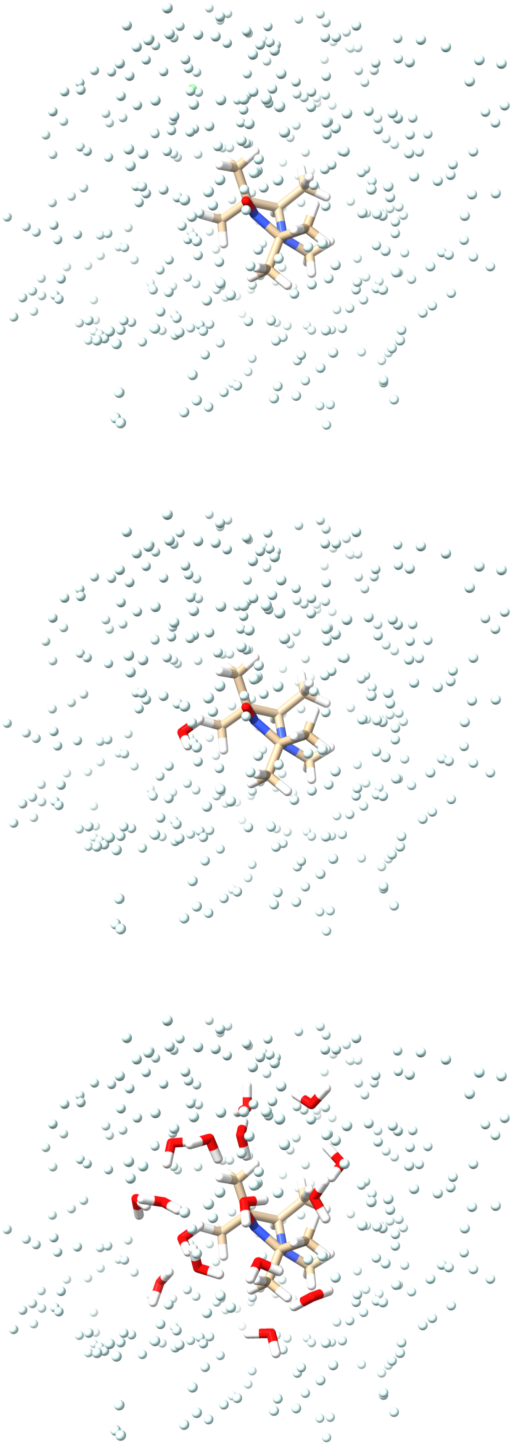

Figure 7.5: Sample snapshots of the tested QM/MM schemes with no solvation shell (top), first solvation shell (middle) and second solvation shell (bottom) in the QM region.

tramolecular vibrational motion, on the molecular skeleton of HMI in solution but neglect effects by solvation because all water molecules were removed from the solvated snapshots prior to the property calculation. The resulting distribution is shown in the bottom row of figure 7.6 and their mean values including the deviation to the experimental A_{iso} value are given in table 7.6. Besides the more narrow distribution a clear shift is observable upon solvation when comparing the mean values obtained at the same level of theory. For revPBE0 the shift is 5.5 MHz whereas DLPNO-CCSD give a shift of 7.1 MHz. Hence, this difference between the two mean values of the solvated and vertically desolvated ensembles quantifies the "solvation shift". Furthermore, the solvation effects are clearly larger (3.8 MHz), almost double, than the thermal effects (2.2 MHz) when comparing both levels of theory with each other. This emphasizes the importance of applying accurate electron correlation theory, i.e., DLPNO-CCSD, to calculate HFCCs in solution and the resulting improvement.

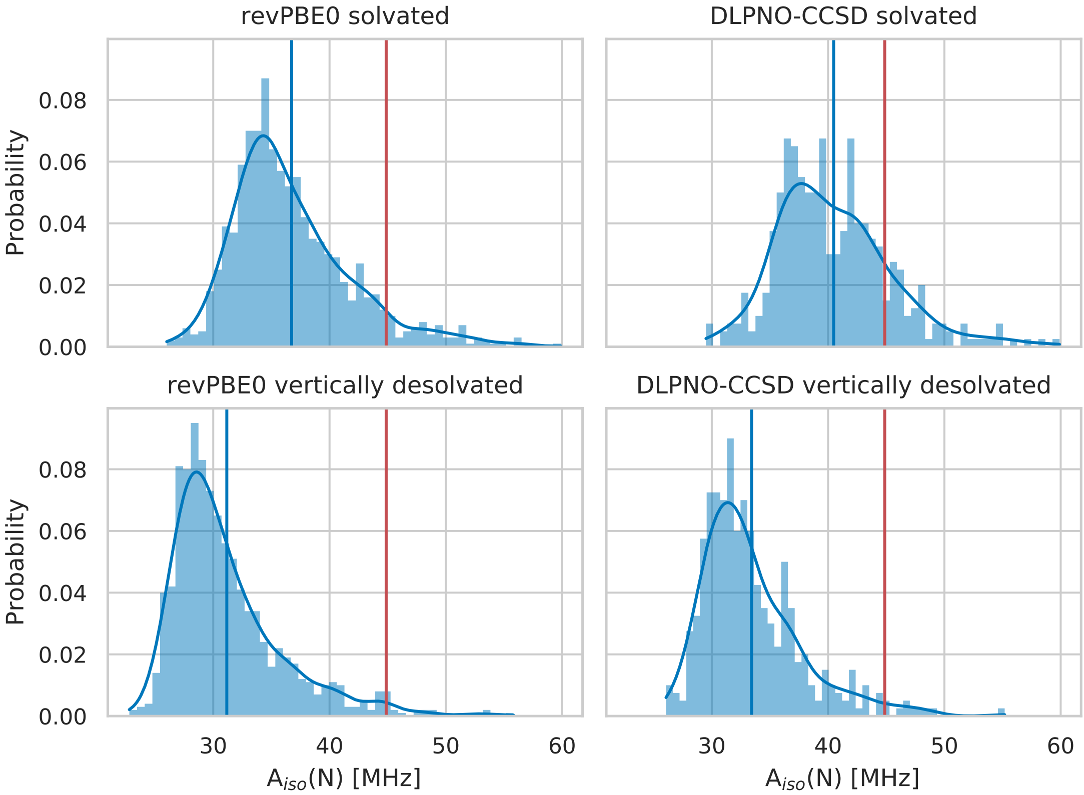

Figure 7.6: Distribution including KDE plot of A_{iso} of the nitroxy nitrogen computed at revPBE0 (left) and DLPNO-CCSD level of theory (right) using the solvation QM/MM scheme for the snapshots (top) and after vertically desolvating the snapshots (bottom). The vertical red line corresponds to the experimental value of 44.87 MHz, whereas the vertical blue line corresponds to the mean value of the displayed distribution as given in table 7.6. The bins are normalized such that they add up to 1.

Table 7.6: Average A_{iso} values [MHz] of the nitroxy nitrogen computed at different levels of theory and with different environments considered for the property calculation. The values in brackets refer to the absolute deviation from the experimental A_{iso} value of 44.87 MHz.

solvation scheme	revPBE0	DLPNO-CCSD
solvated	36.7 (8.2)	40.5 (4.4)
vertically desolvated	31.2 (13.7)	33.4 (11.5)

7.4 Accurate prediction of HMI's full EPR spectrum

In this and the following section the experimental measurements and analysis of the multifrequency cw EPR spectra serve as the reference point for the theoretical investigation. We will therefore give a short summary of the experimental findings. Afterward, we focus on the analysis of the computed EPR parameters, in particular the g-values and the HFCCs of the nitroxy ^{14}N-nucleus (for simplicity referred to as "A-values" in the following).

The experimentally measured cw EPR spectra are referred to as "experimental spectra" (**exp**) in the following whereas the "theoretical spectra" (**theo**) is the simulated spectra that results from the sum of all individual spectra based on the theoretically calculated g- and A-values. The spectra obtained through simulation and least-square fitting to the **exp** and **theo** traces are referred to as "simulated spectra" (**sim**), more precisely, "experimental simulated spectra" (**exp-sim**) and "theoretical simulated spectra" (**theo-sim**). A further specification on the underlying data set of **theo** and **theo-sim** is denoted by "_XX-SetYY-ZZ" (XX=environment of AIMD trajectory, YY=number of snapshots used for simulating **theo**, ZZ=treatment of environment) with the computational details given in table 7.1.

The difference between the **theo** and **theo-sim** spectra is important to point out: The **theo** spectra aim to reproduce the physics of the real-world experiment as closely as possible by investigating each member of the solvated ensemble and using proper statistics to integrate over them. Hence, we are treating explicitly the solvated ensemble of molecules. The simulated spectrum is then a phenomenological representation of that spectrum. In order to implicitly account for the fact that we are dealing with a complex ensemble strain parameters and effective SH parameters are thereby introduced. It is clear that the **theo** and **theo-sim** spectra will only coincide, if the phenomenological model is able to capture all critical effects of the ensemble in its parameterization. Hence, missing physics in the phenomenological modeling cause deviations between the two sets of spectra.

In contrast to the theoretical approach, the **exp-sim** spectrum is the result of the data reduction process leading from the primary observation, i.e., experimental measurement, to a set of SH and linewidth parameters. The small deviations from the **exp** trace result from the sum of all small interactions in the SH that were not modeled. Note that the theoretical spectra obtained by summing the simulated traces from each snapshot or subensemble thereof were treated in the same way. Consequently, this allows an unbiased comparison of the theory and experiment.

The comparison between the **theo** and **exp** spectra is another interesting and notable one. Here, deviations of these spectra from each other indicate deficiencies of the microscopic modeling in the theoretical treatment. These can come from deficiencies in the electronic structure treatment, deficiencies in the sampling or the molecular dynamics treatment itself. One important objective within this thesis is therefore to understand these deviations as cleanly as possible.

7.4.1 Summary of experimental results

All experimental multifrequency measurements were conducted by Markus Teucher, who as well did the analysis and fitting of the experimental spectra to obtain the EPR ($\mathbf{g}$, $\mathbf{A}$) and ALW parameters. Here, we will give a short summary of the experimental findings to provide reference and context for the subsequent theoretical investigations.
One key observation in the experiment was the heterogeneity in g_{xx} parameter which is indicated by a shoulder in the g_{xx} (low field) region. The main peak is characterized by a higher g_{xx} value while the shoulder is represented by a lower one. A satisfying simulation of the experimental data was obtained by a global fitting procedure that used two sets of EPR parameters differing in the g_{xx} value, denoted by ***Comp1*** and ***Comp2***. The best fit was hereby obtained for g_{xx} values of 2.00834 and 2.00795 with a ratio of 0.67:0.33. The difference (Δg_{xx}) between these two values amount to 4×10^{-4} which can be assigned to one additional H-bond formed towards the nitroxy group.[128, 129, 135]
The other key finding of the multifrequency experiment is encoded within the extracted orientation dependent ALW, denoted as alw_{xx}, alw_{yy} and alw_{zz}. While alw_{yy} and alw_{zz} barely vary with the microwave frequency alw_{xx} clearly increases from 24 MHz (W-band) to 52 MHz (J-band) due to an existing g-strain. Up to W-band the field independent line broadening of circa 20 MHz still dominates the spectra.
All experimentally obtained data are given in table 7.7 while the experimental spectra are presented in figure 7.11 that will be discussed in the following upon comparing the theoretical to the experimental spectra.

Table 7.7: Parameters used for the fitting of the experimental multifrequency spectra. Two g_{xx} components were used in the fit, denoted with the columns ***Comp1*** and ***Comp2***. An orientation dependent phenomenological Gaussian line broadening was considered (distinct linewidths $lw_{xx}, lw_{yy}, lw_{zz}$) as specified in EasySpin with the function HStrain. All parameters are obtained by simulation with EasySpin of the experimental spectra. All experimental data and analysis were provided by Markus Teucher.

		exp-sim	
		Comp1	***Comp2***
weights		0.67	0.33
g_{xx}		2.00834	2.00795
g_{yy}		2.00598	2.00598
g_{zz}		2.0023	
A_{xx}		14	
A_{yy}		14	
A_{zz}		100	
alw_{xx}	X	20	
	Q	24	
	W	24	
	J	52	
alw_{yy}	X	20	
	Q	22	
	W	21	
	J	28	
alw_{zz}	X	18	
	Q	18	
	W	18	
	J	25	

7.4.2 Theoretically calculated EPR parameters

In this subsection, we will discuss the calculated EPR parameters and compare them to the experimental quantities in an effort to assign the two species resolved in the experimental measurements.

For this purpose, both solvated ensembles, Solv-Set1000-QM/MM and Solv-Set400-QM/MM, were divided into the corresponding H-bond subensembles according to the analysis described in subsection 7.2.3. The larger Solv-Set1000-QM/MM was taken as reference to evaluate whether the obtained populations of H-bond subsets, g- and A-values respectively, have converged for the smaller Solv-Set400-QM/MM. The comparison revealed that the population of the most occurring H-bond situations, namely 1/2/3 H-bonds, has basically converged for Solv-Set400-QM/MM as depicted in figure 7.7. Considering that the g-values are computed at the same level of theory for both Solv-Set1000-QM/MM and Solv-Set400-QM/MM, it can furthermore be observed that the mean g-values of the subensembles have converged for Solv-Set400-QM/MM. Therefore, the computed mean A-values for Solv-Set400-QM/MM are most likely converged as well. This is important for the comparison of the theoretically determined subensembles to the experimentally resolved components.

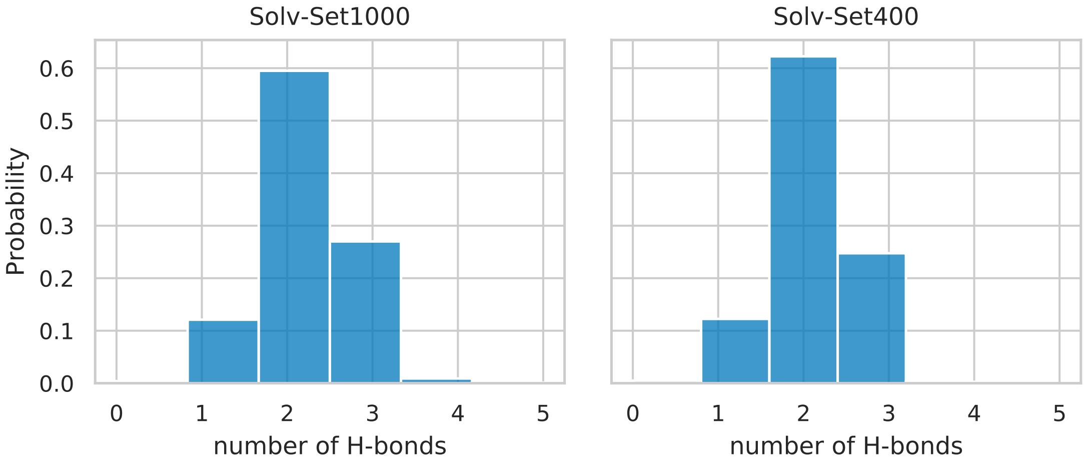

Figure 7.7: Distribution of numbers of H-bonds formed towards the nitroxy oxygen of HMI along the solvated AIMD trajectory.

While the experimental spectra clearly show two different components, the AIMD simulations have identified three distinct H-bond subensembles (see figure 7.7) based on analyzing the structure of the system along the calculated trajectory. These three subensembles correspond to structures featuring 1, 2 and 3 H-bonds to the nitroxy oxygen, respectively. Given that the population of the 1 H-bond contribution is fairly small compared to the 2- and 3 H-bonds subensembles, it is possible that the experiment simply does not resolve the 1 H-bond subensemble. The following analysis is conducted under this assumption and further evidence for its correctness is provided below.

Allowing for only 2 and 3 H-bond situations, the theoretical results are in good agreement with the experiment. While the experimental ratio of the two observed populations is 0.67:0.33 (see table 7.8), the theoretical ratio of the H-bond populations (2 H-bond:3 H-bond) is 0.72:0.28/0.69:0.31 (Solv-Set400-QM/MM/Solv-Set1000-QM/MM). In combination with the calculated SH parameters discussed in the following, this points to assigning the 2 and 3 H-bonding situations to the experimentally observed components, with 2 H-bonds being most frequent. Other investigations that observe mainly two H-bonds being formed between nitroxide and solvent molecules in aqueous solution support this assignment.[135, 252, 253] However, it should be noted that the population of the H-bond situation as well as the population of experimentally resolved components are very sensitive to the thermodynamic conditions under which either the experiment or the MD simulations were conducted.[129]

Although we have made every possible effort to ensure a proper comparison between theory and experiment, some differences remain that should be stated and cannot be avoided, at least at present. First of all, these include the thermodynamic conditions under which the experiments and simulations are performed and that most likely influence the resulting H-bond populations. On the one hand the temperature of the AIMD simulation (300 K) was different from the experimental one (100 K) and there is no control on the speed of freezing the sample in liquid nitrogen in different tube sizes. On the other hand, the experimental sample contained 10 % (v/v) glycerol. This is absolutely necessary as cryoprotectant to avoid clustering of HMIs in the ice. Only limited effects on $\mathbf{g}$ or $\mathbf{A}$ are expected since glycerol itself does not change the polarity of the solution, but the number of H-bonds formed might be affected by the presence of glycerol. However, it is beyond the scope of current state of the art AIMD methodology to sample at the experimental thermodynamic conditions. Therefore, the experimental findings will be quantitatively correlated with the theoretical description of the sample, bearing in mind that the thermodynamic properties reflected in the experimental data might not be fully represented by the theoretical ensemble.

The experimental analysis is anchored on the resolved shoulder of the g_{xx} region in the J-band measurement resulting in distinct g_{xx} values of the two observed components with a difference of $\Delta g_{xx} = 4 \times 10^{-4}$. Unfortunately, theory generally underestimates the g-value at the level of revPBE0 for HMIs. Furthermore, this underestimation is most pronounced for larger g-values and thus for the g_{xx} region. While a (weighted) mean g_{xx} value of 2.00821 is obtained from the experimental analysis, theory gives a mean g_{xx} value (weighted average of 1/2/3 H-bond situations, see appendix) of 2.00788. Therefore, a comparison of the absolute g-values is not reliable. Furthermore, no assignment of the experimentally resolved components can be made based on the difference of g_{xx} values. Neither the difference between 1 and 2 H-bonds ($\Delta g_{xx} = 3 \times 10^{-4}$) nor 2 and 3 H-bonds subensembles ($\Delta g_{xx} = 2 \times 10^{-4}$) give quantitatively accurate values. The decrease of the g_{xx} value and increase of A_{zz} value with increasing number of H-bonds as observed in experimental studies is nonetheless captured by theory.[127, 128, 135]

Despite the inconclusive analysis so far, additional insight can be derived from the computed hyperfine couplings which can add to a clearer comparison between experiment and theory. Although the experimentally observed g_{xx} heterogeneity fits two different H-bond situations, only one A_{zz} value of 100 MHz could be resolved in the experiment. Considering an error of only ±1 MHz for HFCCs in experiment and theory (for DLPNO-CCSD[197]), an assignment of 2 and 3 H-bonds to the experimentally resolved components is clearly supported by the A_{zz} values. Those values barely differ with 99 MHz (2 H-bonds) and 101 MHz (3 H-bonds) and thus excellently agree with the experimentally measured value. However, the A_{zz}-value for the 1 H-bond situation (93 MHz) clearly deviates from the experimental one. Note that the analysis relies on the DLPNO-CCSD A-values here since those are the most accurate numbers that can be achieved with the current theoretical methods at hand as demonstrated in section 7.3. There, very good agreement is observed for our approach to calculate the A_{iso} value and the experimentally measured one.

In summary, the joint analysis of calculated populations, calculated g- and A_{zz}-values indicates that the two populations identified experimentally are best represented by the 2 and 3 H-bonds configurations. A summary of the important parameters is given in table 7.8 and the detailed data of all ensembles and subensembles is given in the appendix.[4]

---

[4] This assignment is supported by the EC-RISM treatment of solvation that gave a mean g_{xx} value of 2.00796, which shows a similar deviation from the experiment as the calculation with explicit waters. Therefore, the underestimation of the g-values is independent of the chosen solvation modeling scheme. Furthermore, the EC-RISM calculations gave a mean A_{zz} value of 103 MHz is obtained, which also shows a very good agreement with the experimental reference. All EC-RISM calculations were conducted by Tim Pongratz, who provided these values.

Table 7.8: Calculated EPR parameters based on the QM/MM approach for the (explicit) solvation treatment in comparison to the experimentally determined values. The g- and A-values are obtained as the mean of the H-bond subensembles based on the H-bond analysis of the underlying data set Solv-Set1000-QM/MM and Solv-Set400-QM/MM with the computational details being summarized in table 7.1. All A-values are given in MHz.

	exp-sim		**theo-sim_Solv-Set1000-QM/MM**		**theo-sim_SolvSet400-QM/MM**	
	Comp1	***Comp2***	***TComp2*** 2 H-bonds	***TComp3*** 3 H-bonds	***TComp2*** 2 H-bonds	***TComp3*** 3 H-bonds
weights	0.67	0.33	0.69	0.31	0.72	0.28
g_{xx}	2.00834	2.00795	2.00791	2.00767	2.00788	2.00769
g_{yy}	2.00598	2.00598	2.00578	2.00572	2.00575	2.00571
g_{zz}	2.0023	2.0023	2.00214	2.00214	2.00214	2.00214
A_{xx}	14	14	7	7	12	11
A_{yy}	14	14	7	8	12	12
A_{zz}	100	100	95	98	99	101

7.4.3 Overall accuracy of theoretically predicted EPR spectra

The main result of subsection 7.4.2 enabled assigning the experimentally resolved components to 2 and 3 H-bonds subensembles, respectively, with 2 H-bonds being the predominant component. In this subsection, the overall accuracy of theoretically predicted EPR spectrum based on the identified components will be evaluated.

For this purpose, spectra were simulated for the 2 and 3 H-bond subensembles based on the EPR parameters given in table 7.8. Their weighted sum (**theo-sim**) was subjected to the comparison with the experimental simulated spectrum (**exp-sim**).

In figure 7.8 the theoretical simulated spectra (**theo-sim**, blue) is plotted alongside the experimental simulated spectra (**exp-sim**, red). Here, the focus was set on the W- and J-band since they best resolve the principal g-values as well as the A_{zz} splitting. To align the g_{zz} signal the **theo-sim** spectra are shifted. Figure 7.8a shows the simulation with all EPR parameters based on the theoretical calculations whereas the linewidths were taken from the experimental analysis. Very good agreement of the A_{zz} value is observable by directly comparing the **exp** and **theo-sim** spectra whereas a clear underestimation of the g_{xx} value is visible in the **theo-sim** spectra. Furthermore, the **theo-sim** spectra does not reproduce the experimentally resolved shoulder in the g_{xx} region as visible in figure 7.9. This is attributed to the underestimation of the g_{xx}-differences between ***TComp2*** and ***TComp3***. Simulating ***TComp2*** with a g_{xx} value of 2.00806 instead of 2.00791 (all other parameters unchanged) to adjust this difference yields very good agreement between theory and experiment as shown in figure 7.9b. This shift by 150 ppm of a single parameter which equals to 2.7 % of $\Delta g_{xx}(\boldsymbol{TComp2})$ results in a visible shoulder in the g_{xx} region in the J-band spectrum. Of course, shifting only one g_{xx} value to fix the g_{xx} difference does not overcome the overall underestimation of the g-values as can be seen. The achieved agreement here, nevertheless, is fairly satisfying, given that the deviation between theory and experiment mainly originates from the level of theory used for the g-tensor calculation.

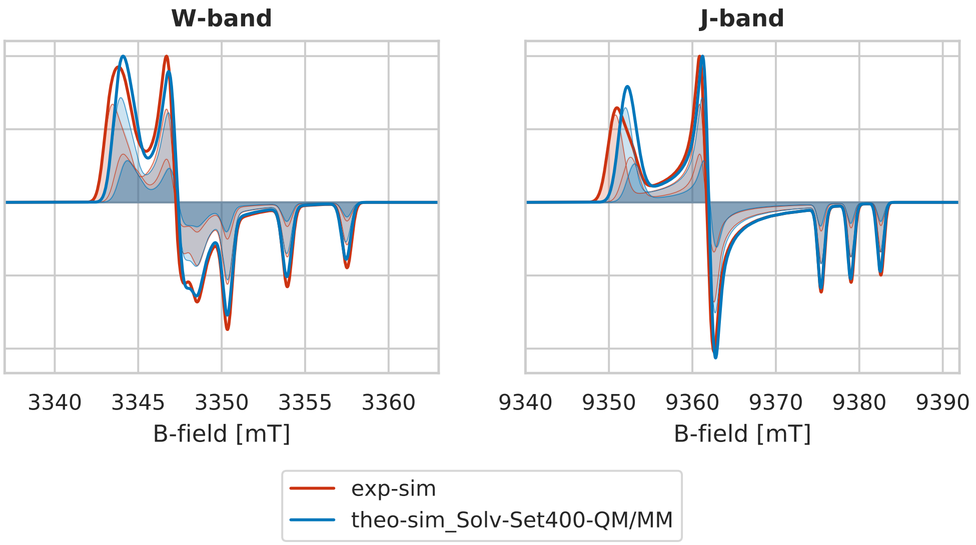

(a) All EPR parameters from calculation, linewidth taken from experimental analysis.

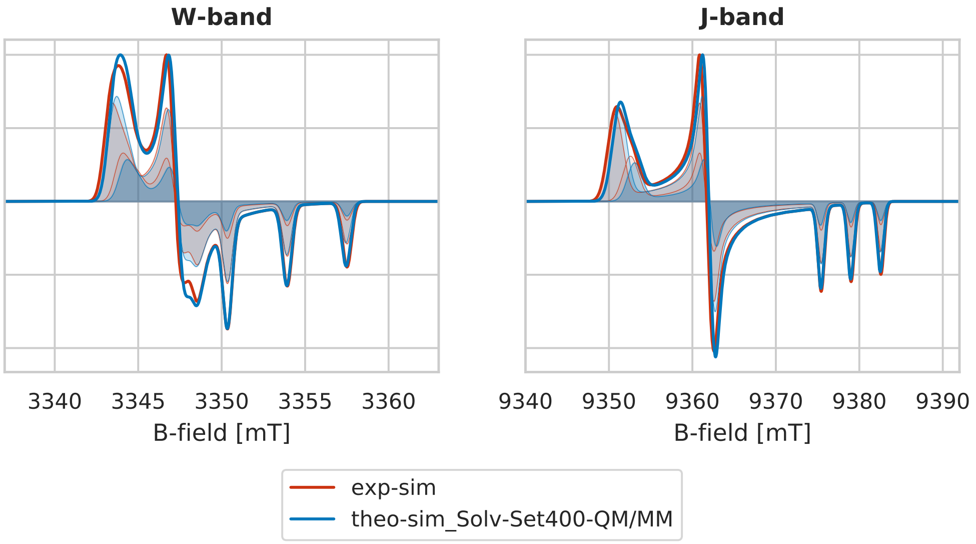

(b) All EPR parameters from calculation except for g_{xx} of ***TComp2***, which was adjusted to 2.00806 to achieve the experimental Δg_{xx} between the spectral components, linewidth taken from experimental analysis.

Figure 7.8: Comparison of **theo-sim** spectra (blue) based on a multicomponent ansatz to **exp-sim** spectra (red). The underlying components of the theoretical simulation are the filled blue curves. The parameters used for the simulation can be found in 7.8. Note that the DLPNO-CCSD A-values were used, hence based on the Solv-Set400-QM/MM data set. The theoretical spectra were shifted by 0.3 mT (W) and 0.8 mT (J), respectively, to align the **exp-sim** and **theo-sim** spectra at the g_{zz} signal.

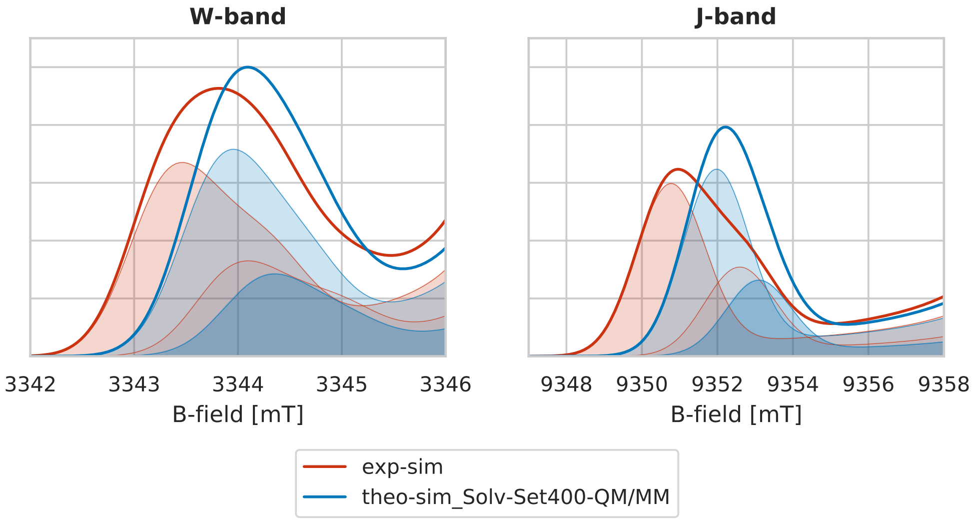

(a) All EPR parameters from calculation, linewidth taken from experimental analysis.

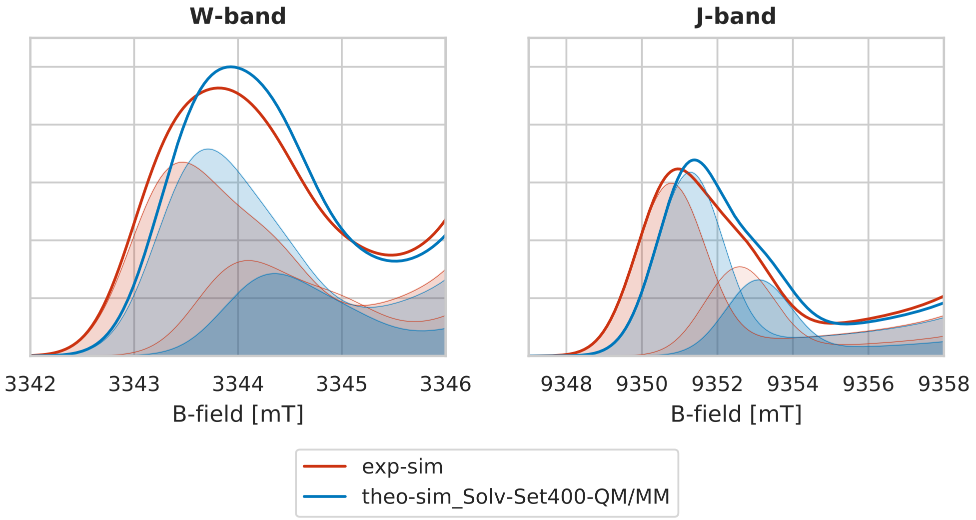

(b) All EPR parameters from calculation except for g_{xx} of ***TComp2***, which was adjusted to 2.00806 to achieve the experimental Δg_{xx} between the spectral components, linewidth taken from experimental analysis.

Figure 7.9: Zoom onto the g_{xx} region of figure 7.8.

7.5 Investigation of the molecular origin of the g-strain

7.5.1 Theoretical multifrequency cw EPR spectra for HMI in solution

Having accomplished a fairly comprehensive comparison of experimental and theoretical simulated spectra, we will now investigate the linewidth and strain parameters. The first step to analyze the g-strain from a purely theoretical perspective is to generate a theoretical reference spectrum which is the normalized sum of spectra of all snapshots along the AIMD trajectory of the given ensemble. Since the distribution of g-values is the crucial quantity here, our analysis is based on the larger ensemble (Solv-)Set1000. Figure 7.10 shows an unconverged g_{xx} region for the smaller ensemble by comparing the theoretical spectra of Solv-Set1000-QM/MM and Solv-Set400-QM/MM.

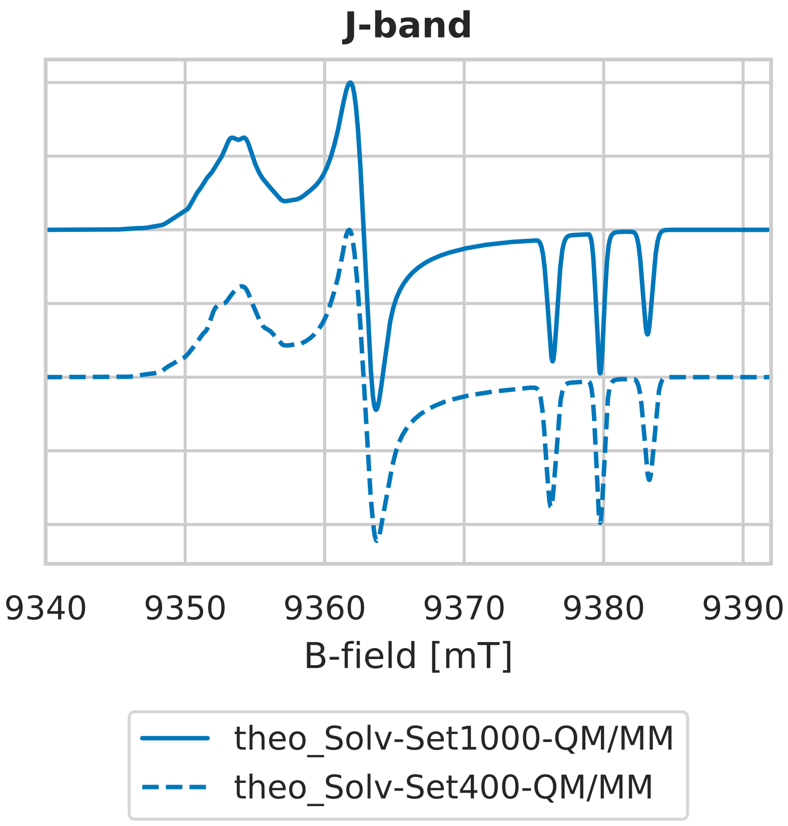

Figure 7.10: Comparison of the theoretical spectra obtained from the Solv-Set1000-QM/MM and Solv-Set400-QM/MM ensembles.

Figure 7.11 depicts the theoretical spectra (**theo_Solv-Set1000-QM/MM**) alongside the experimental spectra (**exp**)[5]. The spectra are characterized by two main interactions, hyperfine (**A**) and Zeeman (**g**). They agree qualitatively well with the experimental measurements and show the typical pattern as observable for nitroxides. The hyperfine interaction dominates the X-band whereas an intermediate regime is depicted for the Q-band with the Zeeman and hyperfine interactions contributing comparably. In these cases, deviations to the experimental spectra can be attributed to an underestimation of the hyperfine interaction.

Starting from the W-band the Zeeman interaction clearly dominates the spectrum. This leads to the resolution of the principle g-values. Compared to g_{yy} and g_{zz} a clearly broader g_{xx} signal is observable additionally, hinting at a significant g-strain. The theoretical J-band improves the resolution of the g_{xx} region, so that a splitting starts evolving and indicates different underlying components. This characteristic agrees with the shoulder at the g_{xx} signal of the J-band experiment. While the principal g-values are well resolved at higher frequencies, the hyperfine couplings are never fully resolved. Here, deviations to the experimental spectra are clearly dominated by the underestimation of the g-tensor components.

7.5.2 Simulation of theoretical multifrequency cw EPR spectra

Having established a common starting point with the theoretical spectra as pendant to the experimental spectra, the g-strain phenomenon will now be quantitatively investigated from the theoretical point of view.

To this end, the theoretical multifrequency cw EPR spectra were analyzed analogously to the experimental procedure based on a multicomponent ansatz as shown in figure 7.12. Building upon the assignment of the experimentally resolved spectral components from the previous analysis, two components were used here as well. Those correspond to the 2 H-bonds (***TComp2***) and 3 H-bonds (***TComp3***) subensembles.

The theoretical simulated spectrum (**theo-sim_Solv-Set1000-QM/MM**) and the theoretical (**theo_Solv-Set1000-QM/MM**) spectrum show good agreement for the X-band and Q-band spectra in figure 7.12. For the W and J-band spectra a slightly more pronounced deviation is visible. First, a difference of intensity pattern for the triplet peak of the A_{zz} splitting is observable in the g_{zz} region. While the **theo-sim_Solv-Set1000-QM/MM** spectrum produces a triplet with decreasing absolute intensity, the **theo_Solv-Set1000-QM/MM** spectrum depicts a splitting pattern with the middle peak of the triplet being most intense. This indicates a stronger variation of A_{zz} among the whole en-

---

[5] Experimental data were provided by Markus Teucher.

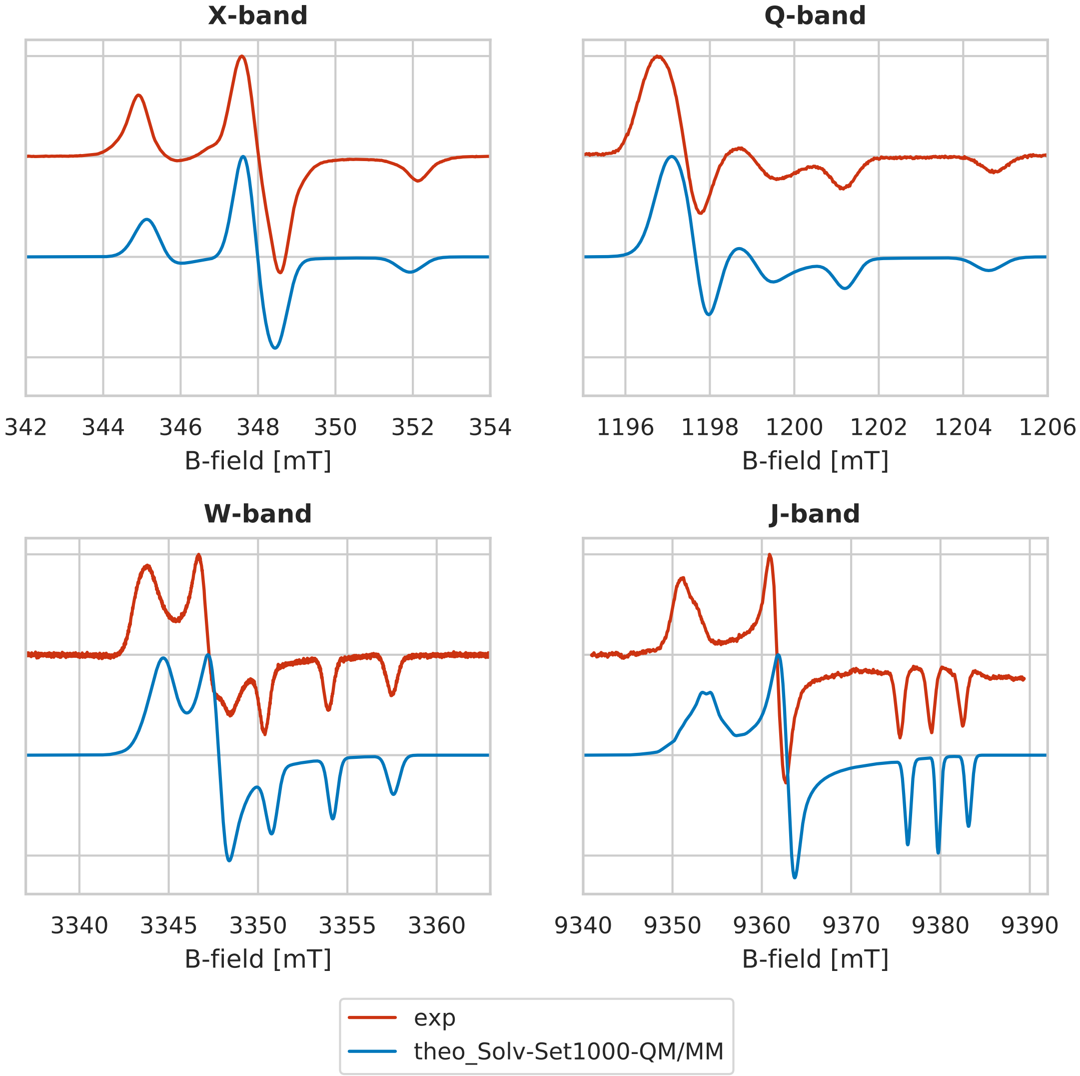

Figure 7.11: Theoretical multifrequency cw spectra of HMI in water based on the calculated g- and A-values using the QM/MM approach (**theo_Solv-Set1000-QM/MM**) for the treatment of solvation plotted alongside the experimental spectra (**exp**, data provided by Markus Teucher).

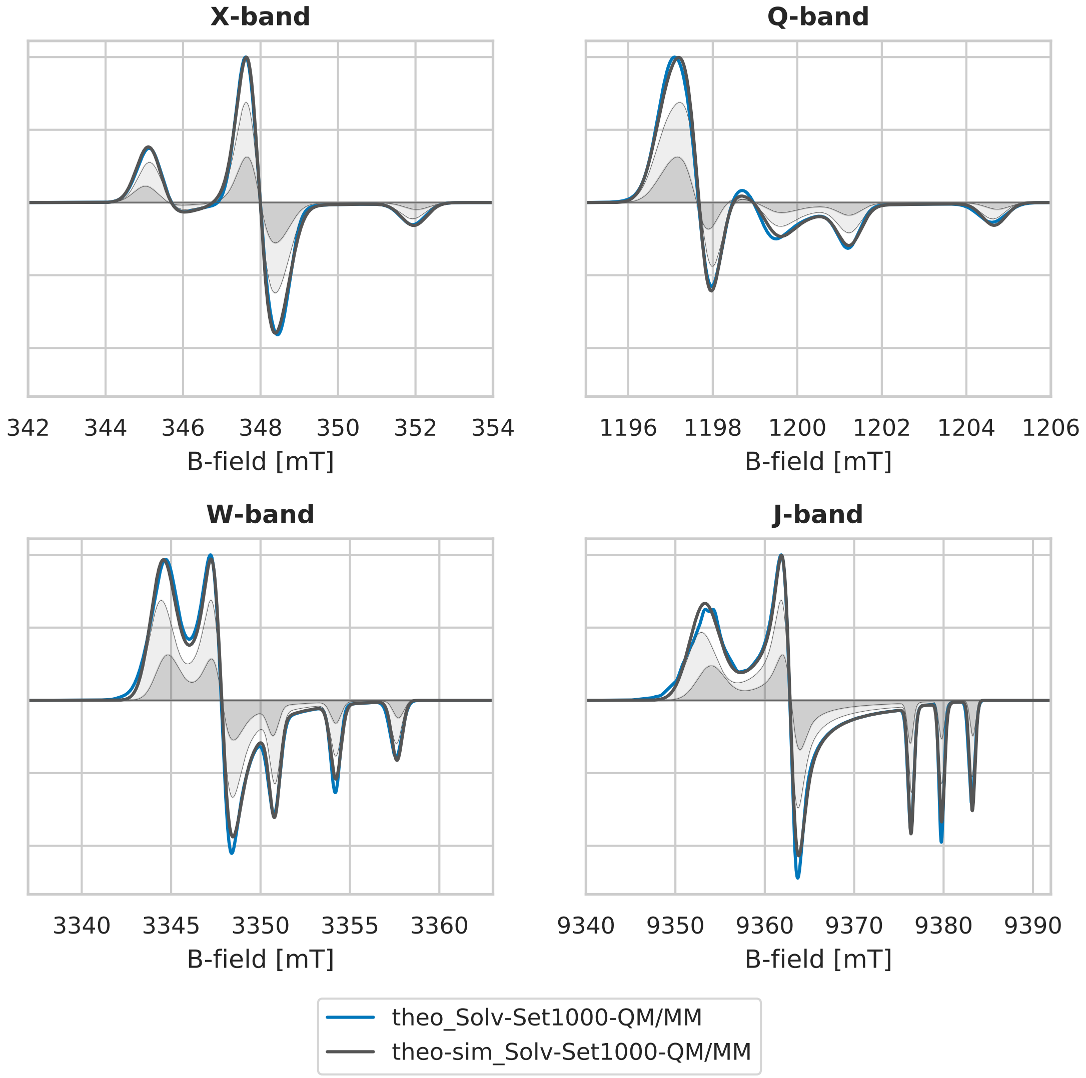

Figure 7.12: Theoretical multifrequency cw spectra of HMI (**theo_Solv-Set1000-QM/MM**, blue trace) and simulated spectra (**theo-sim_Solv-Set1000-QM/MM**, grey trace). The **theo-sim_Solv-Set1000-QM/MM** spectra are obtained as a sum of two spectral components (grey filled areas) in a ratio of 0.69:0.31 (***TComp2***:***TComp3***). The components and corresponding ratios are obtained from sorting the Solv-Set1000 AIMD trajectory into different H-bond situations around the nitroxy group, i.e. ***TComp2*** = 2 H-bonds, ***TComp3*** = 3 H-bonds.

semble of snapshots than recovered by the simulation, i.e., the two different components of the simulation with their two different A_{zz} value do not capture the real variation. Second, the g_{xx} region is not properly reproduced by **theo-sim_Solv-Set1000-QM/MM**. For the J-band spectrum this deviation is pronounced since the higher frequency leads to a better resolution of different g-values. The onset of a splitting at the g_{xx} signal is shown by the **theo_Solv-Set1000-QM/MM** spectrum. Additionally, the g_{xx} signal is not smoothly shaped like a Gaussian. This clearly hints at different components of which the total spectrum consists. However, those components are not well reproduced by the H-bond classified components of the simulation of HMI.

Despite these deviations, an ALW could be extracted for each orientation (alw_{xx}, alw_{yy}, alw_{zz}) from the simulated spectra. The data is provided in table 7.9. The linewidth of the g_{zz} signal is nearly constant across all frequencies and components whereas the linewidth of the g_{yy} signal varies slightly with increasing frequency, thus showing a small strain. The fitted ALW for the g_{xx} signal behaves clearly differently. As already indicated by the strongly broadened g_{xx} signal in the J-band compared to the W-band a clear strain is observable. As shown and discussed in the following in more detail, a linear correlation exists between the ALW and the frequency, i.e., showing an underlying g-strain that dominates the theoretical spectra. Furthermore, the strain barely varies with the number of hydrogen bonds as indicated by very similar slopes of a linear regression for each component. The corresponding figure B.1 is given in the appendix.

Table 7.9: Parameters used for the fitting of the theoretical multifrequency spectra in solution and in vacuum (**theo-sim**) compared to the parameters obtained by the fitting of the experimental data (**exp-sim**, data provided by Markus Teucher). The distinct g_{xx} components are denoted with the columns ***TComp#*** (for the solvated theoretical spectra) and ***Comp#***. An orientation dependent phenomenological Gaussian line broadening was considered (distinct linewidths $alw_{xx}, alw_{yy}, alw_{zz}$) as specified in EasySpin with the function HStrain. All A- and alw-values are given in MHz.

		exp-sim*		**theo-sim_Solv-Set1000-QM/MM****		**theo-sim_Solv-Set1000-vd****		**theo-sim_Vac-Set1000****
		Comp1	***Comp2***	***TComp2***	***TComp3***			
				2 H-bonds	3 H-bonds	2 H-bonds	3 H-bonds	
weights		0.67	0.33	0.69	0.31	0.69	0.31	
g_{xx}		2.00834	2.00795	2.00791	2.00767	2.00891	2.00893	2.00886
g_{yy}		2.00598	2.00598	2.00578	2.00572	2.00606	2.00608	2.00604
g_{zz}		2.0023		2.00214		2.00214		2.00214
A_{xx}		14		7		5		6
A_{yy}		14		7	8	5	6	6
A_{zz}		100		95	98	83	83	83
alw_{xx}	X	20		18		17		17
	Q	24		24		24		16
	W	24		40	37	48	52	53
	J	52		102	97	121	125	140
alw_{yy}	X	20		16		17		15
	Q	22		21		20		20
	W	21		23		23		25
	J	28		45	47	41	42	42
alw_{zz}	X	18		21		20		19
	Q	18		18		18		19
	W	18		19		18		19
	J	25		20		20		19

*All parameters are obtained by simulation with EasySpin of the experimental spectra. **The g- and A-values are obtained from calculations at revPBE0 level as mean of the H-bond subensembles if applicable. The weights result from the analysis of H-bond situations along the AIMD trajectory whereas the linewidths were obtained by simulation of the corresponding theoretical spectrum.

7.5.3 Theoretical multifrequency cw EPR spectra for HMI in vacuum

In order to gain more insight into the origin of the strain, we compared the theoretical multifrequency spectra of solvated HMI (**theo_Solv-Set1000-QM/MM**) to spectra of isolated HMI in the gas phase (**theo_Vac-Set1000**). Those were subjected to the exact same simulation procedures as the solvated HMI considered so far. The objective is to differentiate between strain effects that arise from the interaction of the solute with the solvent and strain effects that originate from the internal dynamics of the HMI solute itself. Changes in SH parameters are caused by both intermolecular interactions and internal dynamics, but it is not self-evident which part is dominating over the other. In figure 7.13 the theoretical multifrequency cw EPR spectra of HMI in water is plotted alongside the theoretical spectra for HMI in vacuum.

Besides the expected differences in the g- and A-values, a decrease of g_{xx} and increase of A_{zz} upon solvation, figure 7.13 shows an even broader spectrum for the vacuum data compared to the spectrum calculated in solution. For the g_{xx} signal in the J-band spectra this is especially evident. Analyzing the ALW of the vacuum data shows a stronger increase of linewidth with frequency than for the solvated data ensemble. This indicates that the g-strain origin lies in the conformational variation of the molecule itself as visualized in figure 7.14. The data for the simulation of the theoretical spectra in vacuum and the obtained ALWs are given in table 7.9 next to the experimental and theoretical data in solution.

7.5.4 Discussion of the size and origin of g-strain

Theory and experiment both indicate that the field dependent line broadening originates from two effects – distinct H-bond subensembles and the strain associated for each subensemble. The two subensembles that correspond to 2 and 3 H-bonds situations formed around the nitroxy group of HMI show distinct g_{xx} values which can only be resolved in the J-band measurement. In fact, a two component ansatz is necessary for a matching simulation of the experimental spectrum. However, the effect of unresolved g_{xx} values of the subensembles is rather small for low fields/frequencies as shown in figure 7.14.

Additionally, each subensemble is characterized by its own g-strain which could be quantified by a linear regression through the origin and the field dependent linewidth components extracted from the fitted ALWs according to equation 4.1.[6] For the regres-

---

[6] Note, that this equation is valid in our case since the intrinsic line broadening related to the relaxation time of nitroxides is smaller than 1 MHz and therefore negligible.[131]

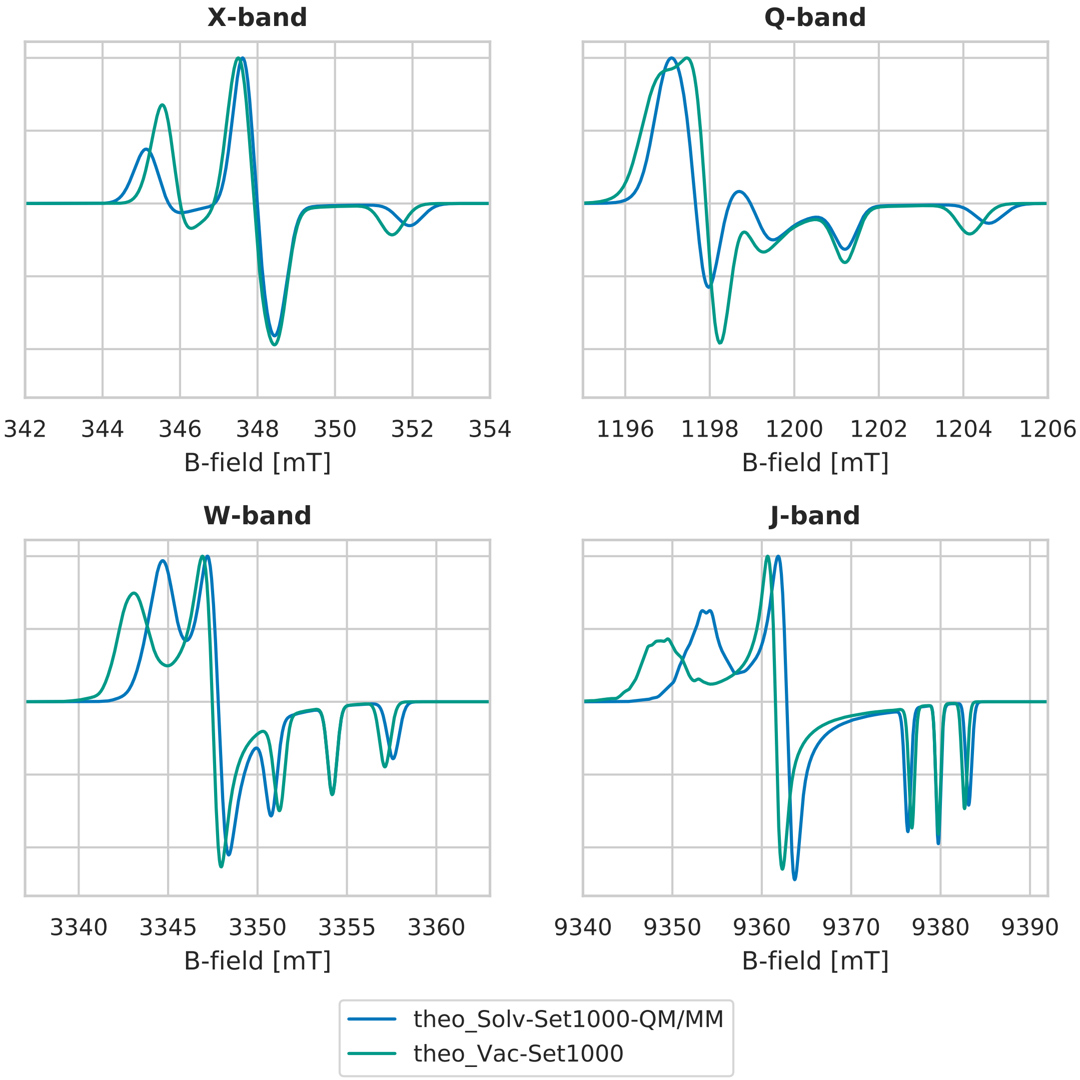

Figure 7.13: Theoretical spectra of HMI in water (**theo_Solv-Set1000-QM/MM**, blue) and HMI in vacuum (**theo_Vac-Set1000**, green) from calculated g- and A-values. The final spectrum is the normalized sum of spectra simulated for each snapshot along the corresponding AIMD trajectory.

sion fit, we only used the W- and J-band values (in addition to the origin) since the field dependent line broadening becomes visible only at higher spectrometer frequencies as shown in figure 7.14. The data used for the regression fit and the obtained slopes are given in table 7.10. The comparison of the experimental strain (186 ppm) with the theoretical strain (376 ppm, theo_Solv-Set1000-QM/MM) shows that theory clearly overestimates the g-strain by roughly a factor of two.

Despite the overestimation, a dissection of the origin of the strain seems highly instructive. The aim is to better understand the effects on the strain arising from the solvation shell or the structural distortion of HMI itself. While the vacuum data (theo_Vac-Set1000) allows the analysis solely based on the conformational distortion of HMI itself since no solvent molecules are present during the AIMD simulation and thus the property calculations, the vertically desolvated (theo_Solv-Set1000-vd) and solvated (theo_Solv-Set1000-QM/MM) allows the distinction between the effects of solvation in general and explicit H-bond formation. Since all solvent molecules are removed prior to the property calculation for the vertically desolvated data, only implicit effects of solvation on the conformation of HMI and therefore on the electronic structure is considered.

Most likely, EPR spectroscopists would intuitively ascribe the bulk of strain to the heterogeneous intermolecular interactions, i.e., HMI with solvent molecules, over the ensemble of molecules in frozen solution.[132, 254] However, this investigation here shows a different picture. Both experiment and theory (theo_Solv-Set1000-QM/MM) show that the g-strain is not affected by the distinct number of H-bonds. While the experimental analysis only requires one set of ALW parameters for both **Comp1** and **Comp2**, the theoretical ALW parameters for **TComp2** and **TComp3** barely differ. In fact, a separate g-strain analysis of **TComp2** and **TComp3** gives slope values that are very close to each other. This observation is furthermore supported by the same analysis based on 2 and 3 H-bonded clusters that were vertically desolvated as given in the appendix.

The in silico desolvation of HMI (theo_Solv-Set1000-vd) even increases the g-strain effects to 464 ppm. We can therefore conclude that the solvation environment of HMI (including the H-bond networks), despite being highly heterogeneous, overall decreases the g-strain. This is furthermore supported by the analysis of the 2 and 3 H-bond subensembles that were partially vertically desolvated by keeping HMI and the solvent molecules that form H-bonds towards the nitroxy group. These additional data, "theo_solv-set1000-hb2vd" and "theo_solv-set1000-hb3vd", follow the observed trend, thus positioning themselves in between theo_solv-set1000-QM/MM and theo_solv-set 1000-vd. In fact, these vertically desolvated H-bond clusters lie very close to theo_solv-set1000-QM/MM. This highlights that explicit formation of H-bonds alone contributes distinctly to the decrease of the g-strain in addition to the indirect effects of solvation on the electronic structure as depicted by theo_solv-set1000-vd (see appendix for the additional data).

Interestingly, HMI in vacuum provides the largest slope (529 ppm) and shows that the strain already exists in the unsolvated system (theo_Vac-Set1000), thus originating from the conformational flexibility of HMI itself.

This implies that the *intra*molecular strain dominates over the *inter*molecular strain for a given H-bond subensemble, at least in the case of HMI and in the way it was theoretically treated. However, in the experimentally resolved subensembles of the J-band, it is clearly visible that $\Delta g_{xx} \approx 400\,\text{ppm}$ due to the presence of 2 and 3 H-bonds exceeds the g-strain of each subensemble, quantified by a slope of $\approx 200\,\text{ppm}$.

Even though the effective number of H-bonds in a subensemble does not affect the strain, H-bonding or generally solvation of the nitroxide has a theoretically calculated effect. Upon solvation of HMI the spectra become *narrower* which leads to a smaller slope obtained by linear fitting the field dependent component of the fitted ALW as presented in table 7.10 and figure 7.14. This is in line with the experimental finding that radical cofactors in confined protein binding pockets, which may potentially restrict the structural flexibility, show strongly reduced g-strain as compared to the same radicals in frozen solutions.[255, 256]

Table 7.10: Summary of data used for the linear regression shown in figure 7.14 including the obtained slope of the linear fit as quantification of the g-strain. The field dependent linewidth (lw_{xx}^{B-dep}) was extracted from the fitted ALW according to equation 4.1 for W- and J-band. The linewidth parameters are given in MHz whereas the slope is given in ppm.

		exp	**theo_Solv-Set1000-QM/MM**	**theo_Solv-Set1000-vd**	**theo_Vac-Set1000**
lw_{xx}^{B-dep}	0 GHz	0	0	0	0
	W	17	35	46	59
	J	49	99	121	139
slope		186	376	464	529
R^2		1.0000	0.9995	1.0000	0.9999

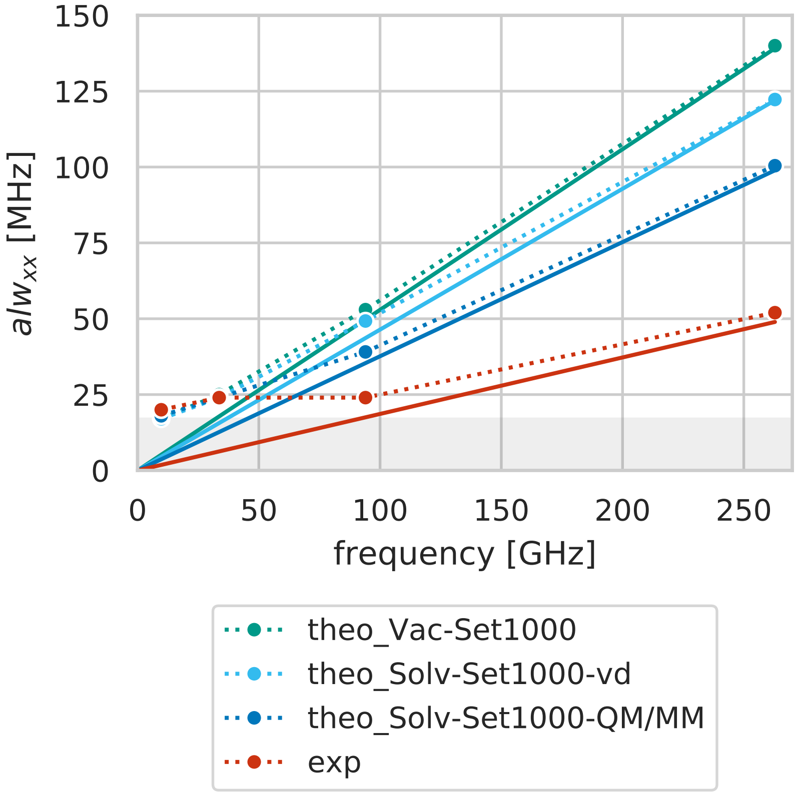

Figure 7.14: Plot of ALW (alw_{xx}) versus measuring frequency as obtained by the fits of the experimental spectra (exp, data provided by Markus Teucher), theoretical spectra of HMI in solution (**theo_Solv-Set1000-QM/MM**), vertically desolvated (**theo_Solv-Set1000-vd**) and in gas phase (**theo_Vac-Set1000**). All linewidth values are given in table 7.9 and if applicable the weighted mean was taken for the W- and J-band linewidths. The solid lines show a linear regression of the extracted field dependent component of the ALW through the origin, W- and J-band linewidths. The data of the linear regression are given in table 7.10. The grey filled area marks the field-independent linewidth which is estimated to 17 MHz from experiment.

7.6 Conclusion

In this chapter we first demonstrated a global approach to compute accurate A-tensors (see section 7.3), in particular focusing on the isotropic A-value, by combining AIMD with high level electronic structure methods, namely DLPNO-CCSD. The resulted thermally averaged A_{iso} values serve as a fair comparison to the experimental value that as well gives an averaged picture of the measured sample. Our theoretical investigation including an elaborate calibration study showed that both adequate solvation modeling and thermal averaging over solute degrees of freedom are equally important to achieve high accuracy in predicting the A_{iso} value. A question that remains is how to further push the accuracy limits. From an electronic structure perspective it appears desirable to include triple excitations, but then the question arises how much accuracy is needed to compare theory to experiment. An error of 1 MHz in the HFCCs is barely visible in a cw-EPR spectrum. Only high resolution pulse experiments can achieve such an intrinsic accuracy. Furthermore, a cw-EPR spectrum is not only characterized by the A-tensor, but also by the g-tensor. In fact, the principal g-values primarily characterize high frequency cw-EPR spectra. As a second order property though, it cannot yet be computed at DLPNO-CCSD level and is therefore subject to method development. Regarding the computational effort, it is noteworthy that this whole study was not possible without the advances made in local correlation methods.

Next, we extended our approach to compute accurate EPR parameters of HMI, g- and A-tensors, that allowed the simulation of EPR spectra to be directly compared with the experimental ones. The analysis of the AIMD trajectory enabled the division of the full g- and A-values set into subsets of different H-bond subensembles. The mean g_{xx} and A_{zz} values of the subensembles show the expected correlation for nitroxides, i.e., a decrease of g_{xx} and increase of A_{zz} upon increasing number of H-bonds. Furthermore, the underlying spectral components as observed in experiment could be identified to correspond to 2 and 3 H-bonds by this analysis. The simulated spectra based on the theoretical components are in good agreement with the experiment. The A_{zz} value agrees with the experimental one within the error margin of ± 1 MHz whereas the g-values are slightly underestimated. This effect is especially pronounced for the largest g_{xx} values.

To take a step further, we then investigated the g-strain from a purely theoretical approach at an unprecedented level of detail. The comparison to the experimental findings reveals that theory strongly overestimates the g-strain. Interestingly, our results indicate that the g-strain is barely affected by the actual number of H-bonds but rather originates from the conformational fluctuation of the molecule itself as a strain is already visible in the analysis of the vacuum trajectory. This is additionally supported by the experimental analysis that used only one set of linewidth parameters for both spectral components that exhibit distinct g_{xx}-values. Although the number of H-bonds has no effect on the g-strain, a change of the solvation environment does. The theoretical analysis show that the g-strain decreases upon solvation, likely due to restricted degrees of freedom caused by the solute solvent interactions. Comparing the fully vertically desolvated data to the explicitly solvated data furthermore shows that the implicit effects of solvation onto the electronic structure of HMI already lead to a decrease of the g-strain. The inclusion of explicit H-bonds distinctly decrease the g-strain in addition. Despite this being maybe slightly counter-intuitive, it is nonetheless supported by experimental findings that show strongly reduced g-strain of radical cofactors in confined protein binding pockets compared to the same radicals in frozen solutions.[255, 256]

8 Overall conclusion and outlook

The two projects presented in this thesis cover method development and application. Both contribute to the theoretical toolbox for efficient and accurate calculations of open shell response properties as well as illustrate the powerful synergy of combined experimental and theoretical study.

The efficient implementation of the unrestricted RI-MP2 response density was presented for the calculation of the electronic g-tensors including the use of GIAOs. This scheme further enabled the use of DHDFT. For our investigations we applied the B2PLYP and DSD-PBE86 double-hybrid functionals. The results revealed a clear improvement of DHDFT upon pure RI-MP2 and good agreement with experimental data for the tested set of small radicals. Furthermore, the computational effort was evaluated for medium to large size radicals. The focus was the choice of approximation for the calculation of the two-electron integrals, more specifically RIJK compared to RIJCOSX. While no preference was observed for medium size radicals, the computational time decreases distinctly for large molecules by using the RIJCOSX scheme.
In comparison to other methods and taking CCSD as a reference both double-hybrid functionals however are outperformed by B3LYP for the given set of small radicals. Nonetheless, further effort to enable open shell response properties using highly correlated methods, e.g., CC theory, remains highly desirable since hybrid DFT still fails for transition metal complexes and other more complicated open shell species. In this context local correlation approaches are favorable to gain efficiency. As an intermediate step towards CC level theory, we have derived the working equations in an unrestricted framework for the CP-OO-MP2 method which provides response densities at the level of OO-MP2. The CP-OO-MP2 equations can be considered as an extension of the CP-SCF equations where the response of the perturbed orbital coefficients includes MP2 correlation. A preliminary implementation for real and imaginary perturbations of open shell systems is described in this thesis. However, further work is required regarding benchmark tests and improvement of efficiency.

The asset of computing molecular response properties accurately is demonstrated by our joint project where we have investigated effects of solvation on the EPR parameters of the nitroxide HMI. Here, we pushed the limits of state-of-the-art computational chemistry by combining high level molecular dynamics, AIMD, with high level quantum chemical calculations, DLPNO-CCSD, to encounter for both dynamical and environmental effects. An extensive benchmark allowed us to build a reliable QM/MM model to compute g- and A-values for a large ensemble of configuration (snapshots). By this means, we did not only predict the isotropic HFCC of the nitroxy ^{14}N of HMI accurately, but also extended this approach to the prediction of the full EPR spectrum, thus bridging theory and experimental reality by calculations of full g- and A-tensors. The combination of AIMD and DLPNO-CCSD HFCC calculations allowed us to assign experimentally observed spectral components which exhibit distinct g_{xx} values to corresponding H-bond subensembles, namely 2 and 3 H-bonds. Furthermore, this study showed the intrinsic underestimation of the g-values for the chosen DFT functional (revPBE0) that failed to reproduce the heterogeneity of the g_{xx} region despite the overall good agreement with experimental data. This again highlights the need of correlated methods for higher order response properties, such as g-tensors, in order to capture the fine details.

In addition, we investigated the g-strain effect from a purely theoretical approach for the first time to the best of our knowledge. The g-strain is the effect of increasing line broadening with spectrometer frequency and associated to the distribution of g-values. Although theory clearly overestimates the g-strain compared to experiment further insight on a molecular level was provided. According to the theoretical investigations of HMI in vacuum the g-strain mainly originates from the conformational flexibility of the molecules itself. Moreover and slightly counterintuitively, the g-strain is independent of the explicit number of H-bonds as supported by experiment. It is rather influenced by solvation as such including the H-bond networks and despite the heterogeneity of a solvated environment. In fact, the g-strain decreases upon solvation which can be explained by restricted degrees of freedom due to the surrounding solvent molecules. A detailed investigation of different solvation approaches furthermore disentangled the effects of solvation on the g-strain. Although the implicit effects of the solvent molecules on the electronic structure of the solute HMI already leads to a decrease of the g-strain, explicit formation of H-bonds significantly decreases the strain. By uniting expertise in experimental measurements and theoretical methodology, we shone more light onto the phenomenological line broadening effect caused by the g-strain.

In the following steps this investigation will be extended to the protonated form of HMI, namely HMIH^{+}, since this spin label is pH-sensitive. Therefore, it is of great interest to understand the effects of solvation on HMI in a protic environment as well. The charge of HMIH$^+$ imposes further challenges on modeling this system appropriately. Nonetheless, it will be insightful to apply the methodological framework established in the extensive studies on the neutral form of HMI as presented here to evaluate the current state of the toolbox for computational spectroscopy and stimulate further effort in the field of method development.

A Supporting data to chapter 5

A.1 Detailed data of comparison with experiment

Table A.1: The experimental values are quoted from references [55] and [235]. All Δg-values are given in ppm.

	experiment	RI-MP2		B2PLYP		DSD-PBEP86	
		def2-TZVPP	aug-cc-pVTZ	def2-TZVPP	aug-cc-pVTZ	def2-TZVPP	aug-cc-pVTZ
H2O+	200	-210	-210	-192	-189	-196	-191
	4800	4497	4477	4336	4312	4270	4248
	18800	15082	14863	13663	13469	13447	13249
CO+	-2600	-1547	-1524	-2348	-2299	-2141	-2097
	0	-217	-216	-142	-142	-159	-158
HCO	-7500	-6556	-6441	-7186	-7036	-7178	-7023
	0	236	225	-228	-223	-212	-206
	1500	2202	2196	2142	2135	2116	2112
C3H5	0	-88	-96	-90	21	-82	47
	400	582	547	573	676	573	758
	800	596	589	634	1046	647	1268
NO2	-11300	-10400	-10172	-10632	-10352	-10608	-10330
	-300	-221	-234	-653	-647	-588	-578
	3900	3005	2883	3265	3138	3220	3109
NF2	-100	-526	-504	-638	-620	-631	-612
	2800	3731	3605	3762	3631	3661	3537
	6200	6562	6370	6474	6270	6347	6155
MgF	-1300	-1605	-1476	-1656	-1520	-1625	-1496
	-300	11	14	3	5	8	10

A.2 Geometries of medium and large size molecules

```
Phenyl

       11

       H     1.22452741590118  -0.16569123199633   2.16590248326982
       C     0.68988966842277  -0.09273772275524   1.21657336203163
       C    -0.70682377004905  -0.03516633667191   1.19624967671414
```

H	-1.26167693522269	-0.06307003219746	2.13491516333244
C	-1.40005040404904	0.05759550936041	-0.01436804600502
H	-2.49141255952405	0.10279782580574	-0.02187250398734
C	-0.69478735656642	0.09379997061429	-1.23127417223617
H	-1.22288741228558	0.16690211316038	-2.18351715382821
C	0.67767887490593	0.03354430480690	-1.14676949585840
C	1.41533292435136	-0.05807310854667	0.01164379289110
H	2.50606955411559	-0.10274129158011	0.01197689367603

Tyrosyl

23

N	1.22791685183297	-2.02606609669862	0.49514963753435
C	1.51266970494313	-1.00863002283874	-0.50475738938634
C	2.96540666734071	-1.03225058205889	-0.98355115049098
O	3.89335531788443	-1.50196261167089	-0.35676297654376
O	3.11400991254623	-0.42618111306367	-2.19418649240596
C	1.22227610086426	0.41660718324633	0.06764422870592
H	1.75137891782911	0.49616896542777	1.02959513414384
H	1.64328097571574	1.16717950014829	-0.61595920303869
C	-0.24721384662228	0.64906343701994	0.24224439796819
C	-0.98279374033321	1.30954727879981	-0.77380485624186
H	-0.44861383942471	1.67669899653126	-1.65410189150694
C	-2.34159169965575	1.49636490937142	-0.66414882390099
H	-2.91788309386407	2.00794802734812	-1.43614047848654
C	-3.07135672018629	1.02018298741642	0.50205163832964
C	-2.28826746219121	0.34465341968111	1.52622830742006
H	-2.82752000613339	-0.01766324524463	2.40240092481571
C	-0.93036514611721	0.17041721785734	1.38783995646168
H	-0.35748013169572	-0.35345293497086	2.15332727523697
O	-4.31407521504375	1.18561908070182	0.61709284100512
H	0.86111793953707	-1.15936784787322	-1.37769849950499
H	4.07244770972434	-0.45119475377011	-2.40182648153457
H	2.05096301031616	-2.13520005876015	1.09604154478312
H	1.07537779273344	-2.93151173659983	0.04901235663703

α-tocopheryl

80

C	2.32220647042194	0.66879740880987	2.20466609079949
C	3.44061656946966	1.48618443430876	1.73348170674028
C	4.08382935428576	1.18060861255765	0.54416088911108
C	3.66298195684208	0.04585517024249	-0.19708086607900
C	2.57531387742241	-0.77879213588601	0.21456084113265
C	1.90591686237670	-0.47299388829005	1.38593331039344
O	1.72984516085520	0.94566465954671	3.28246519903739
C	3.84895911561149	2.66106258976835	2.56841390448918
H	3.22894869707279	2.69756447097169	3.47064985586254
H	3.72846702262648	3.60992549830560	2.01896234371296
H	4.90892119209783	2.59942901071036	2.86267267076500
C	0.74486859694222	-1.28607226261414	1.87733950902142
H	-0.05140152322858	-1.35380321596667	1.12005486209112
H	0.34000847433483	-0.82662343498435	2.78572867451668
H	1.04730058864006	-2.31859994985055	2.11545108954537
C	2.18495966782829	-1.95487917145611	-0.64138416665447
H	3.05305492910219	-2.36762732584115	-1.16822085955868
H	1.45184605598229	-1.65990667913881	-1.40987141741058
H	1.72584474460698	-2.74687320142469	-0.03751314596133
C	5.20634117281237	2.04415049727381	0.02052685501497
O	4.25212298804706	-0.32567134041111	-1.36313602540949
C	5.55518376768905	0.25544648359534	-1.71653809859851
C	5.49279689883692	1.75958079098909	-1.45137275272417
H	4.69164084833892	2.17802381545049	-2.08059827438853
H	6.43223842101957	2.23199400840152	-1.77031967859150
H	6.11669477954075	1.88406359850176	0.62434302537410
H	4.94839478431897	3.10488954709259	0.15629375610477
C	6.60518661380086	-0.47851457648440	-0.86347718073227
C	5.70397861510090	-0.04790805677033	-3.20067769551253
H	4.89130505101054	0.42327336588537	-3.76908098499543
H	5.67202412030236	-1.13194923156883	-3.37620178965343
H	6.65934147239844	0.33872396318425	-3.57858506026269

C	8.04355269844536	0.01735091354904	-1.02061273487752
H	6.54655707682945	-1.54924781278987	-1.11701390257937
H	6.31102315166774	-0.40055054801657	0.19552833050752
C	9.01161047066275	-0.74008427508128	-0.10835911489039
H	8.08871574343021	1.09415114958703	-0.79332208447863
H	8.37159768069431	-0.09086610811811	-2.06853536324151
C	10.48939445038890	-0.34195860442504	-0.25169925444895
H	8.91561140314833	-1.82183248288600	-0.30599078550231
H	8.70527943696686	-0.59629531157511	0.94439500946407
C	11.36597662783030	-1.26362745705668	0.61223837778247
C	12.87248185255140	-1.13599875899256	0.37552677776090
H	11.06734429543950	-2.31055290005765	0.42771860711795
H	11.14468032416100	-1.06914162051415	1.67781146993161
C	13.68864014403750	-2.11346933613713	1.22399246409774
H	13.19515529296830	-0.10440420440222	0.58408107092965
H	13.08804186788990	-1.31540064419377	-0.69328964965528
C	15.20897434466680	-2.06122751660080	0.99581659799076
H	13.33669469016010	-3.13978989422603	1.01890930240759
H	13.48174516289640	-1.93123650117196	2.29487637910961
C	15.89148145356390	-3.24490666228468	1.70142772758712
C	17.38303499652210	-3.41030339892944	1.39883477977539
H	15.36818846727180	-4.17312401677511	1.41115597511694
H	15.74689538456910	-3.14409771488668	2.79296145463015
C	17.97913246687070	-4.66282910927888	2.04614023316275
H	17.94205977907770	-2.52759596700619	1.75191547665209
H	17.52097980057240	-3.44585785096768	0.30525263117308
C	19.49488990434050	-4.83784204137853	1.85882916646102
H	17.46676071777200	-5.55940180785380	1.65028494300539
H	17.75850668229100	-4.64061566579088	3.12777438971408
C	20.00330029425680	-6.02401670491584	2.68545725994922
H	19.75616425241820	-5.90638119142380	3.75103592824604
H	21.09466441016980	-6.13490069137523	2.60036213843267
H	19.54506920195080	-6.96364369181789	2.33752348326568
C	19.87992506528760	-5.00486503774761	0.38395180060870
H	19.98574742048750	-3.92197786885478	2.23772706223231
H	19.60636347540510	-4.12782944622898	-0.21893855062754

H	19.37340719808720	-5.88230583262838	-0.04975432082591
H	20.96400344432300	-5.15701305516514	0.27409536062989
C	15.80081963369400	-0.71859077270478	1.44169949087599
H	15.38795868977350	-2.17225947291303	-0.09108452695633
H	15.31224769045520	0.12798900048500	0.94033812833846
H	16.87509282121930	-0.65140039881062	1.22040664746210
H	15.67158350720290	-0.58604620677073	2.52845227977765
C	10.71296028404140	1.13570945804433	0.09301484042821
H	10.77757649836190	-0.49698146738469	-1.30925197627926
H	10.13855598991760	1.80172981741077	-0.56496402651334
H	11.76979262021000	1.41948352614605	0.00014598953848
H	10.40232378854450	1.33744273000759	1.13150812953324

α-Chlorophyll

73

C	-6.94855526943992	35.861772098	8.07785636779911
C	-3.94860105191036	34.649377406	-0.70564966511195
C	2.45464059246072	37.110783603	3.41612669288321
C	-2.26084759470309	35.881739442	9.97409859997136
N	-4.58243662196812	34.896077801	5.84502372260758
H	-6.96086611068839	36.632668610	7.29395647061134
C	-4.86205691476210	34.672975575	-1.69658965845190
C	2.50040788739034	38.638071612	3.59581046395530
C	-3.73311145145957	35.412222614	9.58304709254251
N	-3.76092437576758	34.966778504	2.97786070537636
O	-1.88499885531334	36.061391285	11.12033344080930
C	-4.03600782546934	34.089318946	10.26584918086840
N	-1.86131862949319	35.828144156	6.43966649034840
C	-4.74416678712488	33.093946636	12.28995642470350
C	-3.72802296659876	35.334714306	8.06607518851559
C	-5.92392824241774	34.241976894	3.88687187374812
C	-1.91007551050183	35.506966691	1.45612247496471
C	0.34974820817972	36.487403581	5.65363656699779
C	-6.93013534821095	32.498691361	6.35153629020336

C	-6.63377997965205	33.770260523	0.87612440168862
C	0.95591407903764	36.437282531	0.63443311005602
C	0.92946677393327	36.821374174	8.77392337734698
C	-4.75916059270189	34.962791255	7.21221446760301
C	-5.05058417773514	34.496452607	2.82990440281382
C	-0.92861742600141	35.892562757	2.37249829797543
C	-0.56389807794288	36.249077069	6.67956818793283
O	-3.85409348239226	32.992016383	9.76558299682804
C	-6.17429026344936	34.619271807	7.60203881231183
C	-5.35178795123259	34.299015925	1.41503423090895
C	0.42838362132706	36.325744993	2.02278721469025
C	-0.33684790164767	36.392417227	8.13296855535392
O	-4.49855706303789	34.293032822	11.51096846156950
C	-6.74622660425314	34.024712437	6.29569437660936
C	-4.21313299672830	34.664527233	0.71938963421344
C	1.06651289908048	36.598305644	3.20773059364581
C	-1.54563281908597	36.035645807	8.71053049408794
C	-5.70900600294446	34.415028942	5.26832389324234
C	-3.22062271612656	35.070246890	1.73151677490451
C	0.09363993646096	36.335335142	4.27396955319515
C	-2.44003484752702	35.702168963	7.64173407234111
N	-1.09581370826696	35.913944374	3.73814280304445
Mg	-2.83696605264959	35.406195682	4.72714700640911
H	-6.50245353105776	36.294313776	8.98278722566552
H	-7.98575141133230	35.581426184	8.30720210679062
H	-2.89274502123784	34.625796625	-0.99233537582081
H	3.07839039841256	36.826658360	2.55565312487213
H	2.90231381880673	36.625173726	4.29777225151205
H	-5.93315687889961	34.744588469	-1.51030972154285
H	-4.54219969573578	34.649233076	-2.73887420419595
H	3.53440274244960	38.977126446	3.74997048803402
H	1.90319547725301	38.953359396	4.46355162196688
H	2.09895555357728	39.145416619	2.70707118019510
H	-4.41682085495970	36.177321312	9.98157945075313
H	-5.10756963741824	33.449141196	13.25850560388390
H	-3.81391071710872	32.524247582	12.40814642216080

H	-5.49998918021546	32.471600794	11.79457700543100
H	-6.90841970781808	33.856326786	3.61944105883767
H	-1.62257234481425	35.546892635	0.40533433450466
H	1.34851787281598	36.819935558	5.93840856413086
H	-7.27999691915223	32.106747750	5.38691780036358
H	-7.67321986942933	32.243810470	7.11953318080824
H	-5.98143211397450	32.004344051	6.60615348672106
H	-6.45197788515741	33.131396783	-0.00077309333639
H	-7.29721130809325	34.585820560	0.54456659248714
H	-7.18050427223117	33.184378261	1.62595431378577
H	2.02102808421553	36.700051463	0.63317181825897
H	0.41610091903090	37.211595201	0.06647594787569
H	0.83336471504235	35.492844177	0.08221685548880
H	0.81750891394865	36.897285768	9.86111960019779
H	1.25889089160802	37.795318164	8.37904357633114
H	1.73780954114030	36.105748628	8.55227859612343
H	-6.17306221094150	33.869796617	8.40859318848612
H	-7.71302869338922	34.486748229	6.03987502611457

B Supporting data to chapter 7

B.1 Linewidth analysis

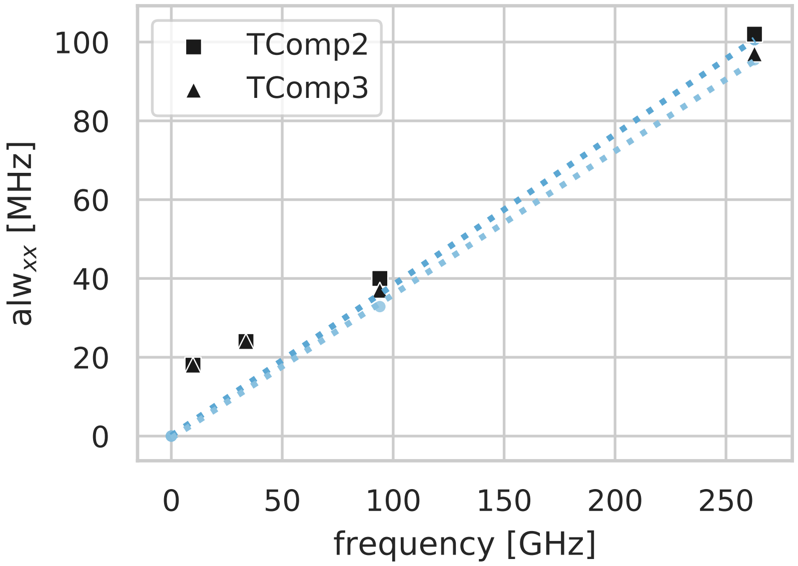

Figure B.1: Plot of ALW (alw_{xx}) versus measuring frequency as obtained by the fits of the theoretical spectra for each component (***TComp2*** and ***TComp3***) separately. As can be seen the explicit number of H-bonds barely influences increase of ALW, thus the g-strain.

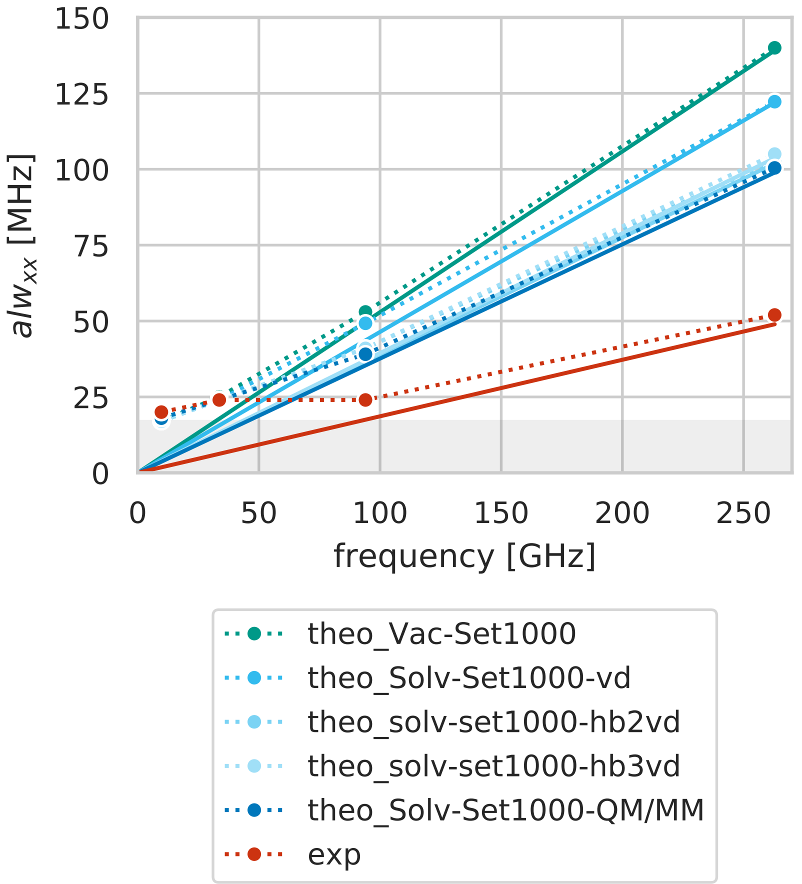

Figure B.2: Plot of ALW (alw_{xx}) versus measuring frequency as obtained by the fits of the experimental spectra (exp, data provided by Markus Teucher), theoretical spectra of HMI in solution (**theo_Solv-Set1000-QM/MM**), partially vertically desolvated (**theo_Solv-Set1000-hb2vd** and **theo_Solv-Set1000-hb3vd**), vertically desolvated (**theo_Solv-Set1000-vd**) and in gas phase (**theo_Vac-Set1000**). All linewidth values are given in table B.2 and if applicable the weighted mean was taken for the W- and J-band linewidths. The solid lines show a linear regression of the extracted field dependent component of the ALW through the origin, W- and J-band linewidths. The data of the linear regression are given in table B.1. The grey filled area marks the field-independent linewidth which is estimated to 17 MHz from experiment.

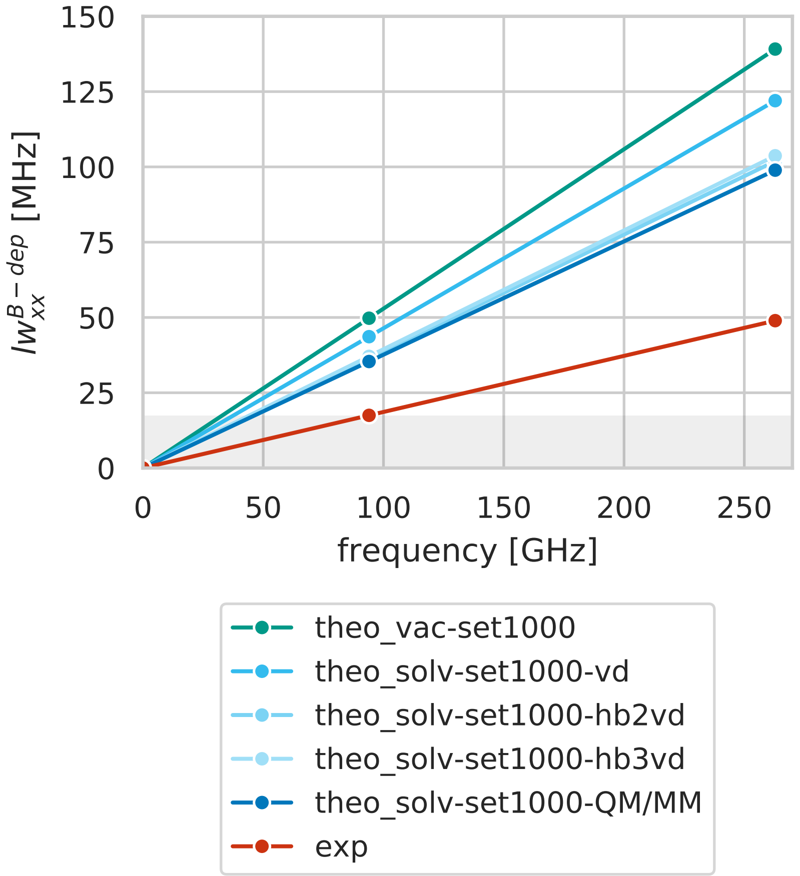

Figure B.3: Plot of field dependent linewidth component (alw_{xx}^{B-dep}) extracted from alw_{xx} according to equation 4.1 versus measuring frequency including the corresponding linear regression. The data plotted here and obtained from the linear regression are given in table B.1.

Table B.1: Summary of all data used for the analysis of the g-strain by means of a linear regression through the field dependent linewidth component (lw_{xx}^{B-dep}) that was extracted from alw_{xx} accoring to equation 4.1.

		exp-sim	**theo_SolvSet1000-**				**theo_Vac-Set1000**
			QM/MM	**hb2vd**	**hb3vd**	**vd**	
lw_{xx}^{B-dep}	0 GHz	0	0	0	0	0	0
	W	17	35	37	37	46	50
	J	49	99	102	104	121	139
slope		186	376	388	395	464	529
R^2		0.9999	1	0.9999	1	0.9995	1

Table B.2: A summary of all investigated ensembles and subensembles alongside the experimental data. The calculated g- and A-values are provided as mean of the corresponding subensemble. The ALW are obtained from fitting the multifrequency spectra. All A- and ALW-values are given in MHz. The experimental data were provided by Markus Teucher.

		exp-sim*		**theo_SolvSet1000-****				**theo_SolvSet400-****				**theo_Solv-Set1000-****					**theo_Vac-Set1000****
				QM/MM				**QM/MM**				**hb2-vd**	**hb3vd**	**vd**			
		Comp1	***Comp2***		***TComp1***	***TComp2***	***TComp3***		***TComp1***	***TComp2***	***TComp3***						
subensembles					1 H-bond	2 H-bond	3 H-bond		1 H-bond	2 H-bond	3 H-bond	2 H-bonds	3 H-bonds		2 H-bonds	3 H-bonds	
# snapshots				1000	121	595	270	400	49	249	99	595	270	1000	595	270	1000
g_{xx}		2.00834	2.00795	2.00788	2.00820	2.00791	2.00767	2.00788	2.00822	2.00788	2.00769	2.00814	2.00789	2.00891	2.00891	2.00893	2.00886
g_{yy}		2.00598	2.00598	2.00576	2.00584	2.00578	2.00572	2.00576	2.00585	2.00575	2.00571	2.00585	2.00580	2.00607	2.00606	2.00608	2.00604
g_{zz}		2.00230	2.00230	2.00214	2.00214	2.00214	2.00214	2.00214	2.00214	2.00214	2.00214	2.00214	2.00214	2.00215	2.00215	2.00214	2.00214
A_{xx}		14	14	7	7	7	7	11	10	12	11	7	7	5	5	5	6
A_{yy}		14	14	8	7	8	8	12	10	12	12	7	7	6	6	5	6
A_{zz}		100	100	96	91	95	98	99	93	99	101	92	95	83	83	83	83
alw_{xx}	X	20	20		18	18	18					17	17		17	17	17
	Q	24	24		24	24	24					24	24		24	24	26
	W	24	24		43	40	37					41	41		48	52	53
	J	52	52		105	102	97					103	105		121	125	140
alw_{yy}	X	20	20		16	16	16					17	17		17	17	15
	Q	22	22		21	21	21					21	21		20	20	20
	W	21	21		23	23	23					24	24		23	23	25
	J	28	28		42	45	47					45	47		41	42	42
alw_{zz}	X	18	18		21	21	21					21	21		20	20	19
	Q	18	18		18	18	18					20	20		18	18	19
	W	18	18		19	19	19					20	20		18	18	19
	J	25	25		20	20	20					20	20		20	20	19

*All parameters are obtained by simulation with EasySpin of the experimental spectra. **The g- and A-values are obtained from calculations at revPBE0 level as mean of the H-bond subensembles if applicable. The weights result from the analysis of H-bond situations along the AIMD trajectory whereas the linewidths were obtained by simulation of the corresponding theoretical spectrum.

B.2 Experimental spectra

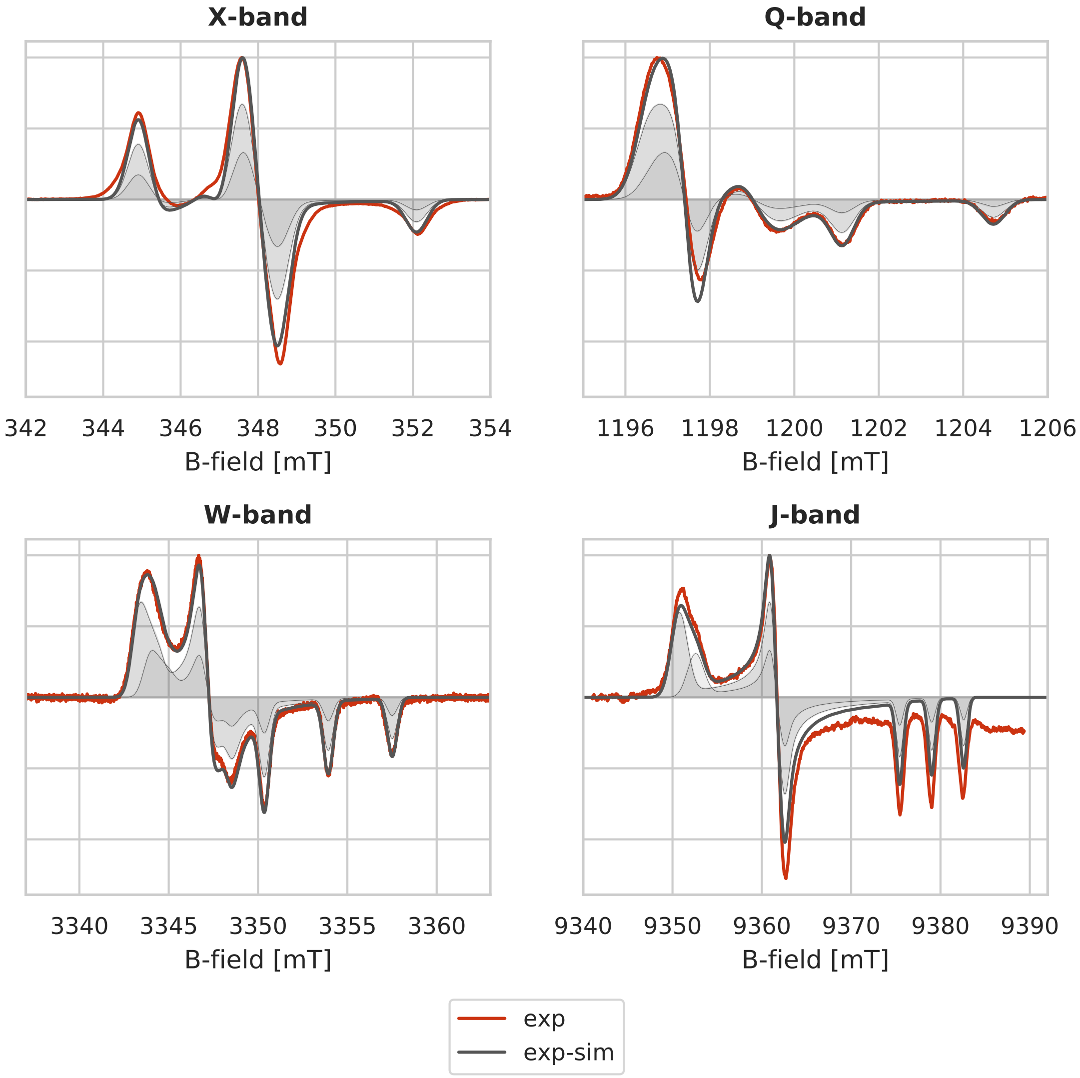

Figure B.4: Experimental multifrequency EPR spectra (red) including the simulation using EasySpin[219] (grey) constructed by two spectral components that correspond to different g_{xx} values. An orientation dependent phenomenological Gaussian line broadening was considered as specified by EasySpin with the function "HStrain". The experimental data are given in table 7.7. All experimental data of the measurement and simulation were provided by Markus Teucher.

B.3 Sample ORCA inputs

```
! revpbe0 d3zero def2/j tightscf g-tensor pal8
%maxcore 4000
%basis
  gtoname = "gus_def2-tzvpp-deconS.bas";
end
%pointcharges "pointc.pc" # remove if no point charges included
%eprnmr
  tol 1e-8
  ori centerofspindens
end
*xyzfile 0 2 qm.xyz
```

Code B.1: Sample input for g-tensor calculation at revPBE0 level.

```
! dlpno-ccsd cc-pwcvtz/c nofrozencore tightscf dlpno-hfc2 keepdens
%pal
  nprocs 16
end
%maxcore 15000
%pointcharges "pointc.pc" # to be commente
%basis
  gtoname = "gus_def2-tzvpp-deconS.bas";
  newauxcgto H "def2-tzvpp/c" remove if no point charges included
end
%mdci
  density unrelaxed
end
*xyzfile 0 2 qm.xyz
%eprnmr
  nuclei = all C { aiso, adip }
  nuclei = all H { aiso, adip }
  nuclei = all N { aiso, adip }
```

```
  nuclei = all O { aiso, adip }
end
```

Code B.2: Sample input for HFCC calculation at DLPNO-CCSD level.

B.4 Sample Matlab scripts

```
%%

clear all

addpath('/path/to/where/project/shall/be/saved');
datNhfc = readmatrix('/path/to/dat_hfc_N.csv');
datg = readmatrix('/path/to/dat_gtensor.csv');

frames = 6000:200:205800;

% ------------------------------------------------
% EasySpin simulation
% ------------------------------------------------
Sys.Nucs = '14N';
Sys.lw = [0.6]; % mT FWHM [Gaussian, Lorentzian] = Voigtian

npoints = 4*1024;
ExpX.mwFreq = 9.7671;
ExpX.Range = [300 400];
ExpX.nPoints = npoints;
ExpQ.mwFreq = 33.6615;
ExpQ.Range = [1100 1400];
ExpQ.nPoints = npoints;
ExpW.mwFreq = 93.993;
ExpW.Range = [3300 3600];
ExpW.nPoints = npoints;
ExpJ.mwFreq = 262.8436;
ExpJ.Range = [9300 9500];
ExpJ.nPoints = npoints;
```

```

sim_all_S = zeros(npoints,1000);
sim_all_X = zeros(npoints,1000);
sim_all_Q = zeros(npoints,1000);
sim_all_W = zeros(npoints,1000);
sim_all_J = zeros(npoints,1000);

% generate the spectrum for each frame -----------
for i = 1:1000
    Sys.A = [datNhfc(i,1),datNhfc(i,2),datNhfc(i,3)];
    Sys.g = [datg(i,1),datg(i,2),datg(i,3)];
    spcnameX = 'spc_sim_X_'+string(frames(i));
    spcnameQ = 'spc_sim_Q_'+string(frames(i));
    spcnameW = 'spc_sim_W_'+string(frames(i));
    spcnameJ = 'spc_sim_J_'+string(frames(i));
    [B_simX,spcnameX] = pepper(Sys,ExpX);
    sim_all_X(:,i) = spcnameX;
    [B_simQ,spcnameQ] = pepper(Sys,ExpQ);
    sim_all_Q(:,i) = spcnameQ;
    [B_simW,spcnameW] = pepper(Sys,ExpW);
    sim_all_W(:,i) = spcnameW;
    [B_simJ,spcnameJ] = pepper(Sys,ExpJ);
    sim_all_J(:,i) = spcnameJ;
end

norm_sim_ave_X = mean(sim_all_X,2)/max(mean(sim_all_X,2));
data_simX = [transpose(B_simX),norm_sim_ave_X];
writematrix(data_simX,'nameXband.csv');

norm_sim_ave_Q = mean(sim_all_Q,2)/max(mean(sim_all_Q,2));
data_simQ = [transpose(B_simQ),norm_sim_ave_Q];
writematrix(data_simQ,'nameQband.csv');

norm_sim_ave_W = mean(sim_all_W,2)/max(mean(sim_all_W,2));
data_simW = [transpose(B_simW),norm_sim_ave_W];
writematrix(data_simW,'nameWband.csv');
```

```

norm_sim_ave_J = mean(sim_all_J,2)/max(mean(sim_all_J,2));
data_simJ = [transpose(B_simJ),norm_sim_ave_J];
writematrix(data_simJ,'nameJband.csv');
```

Code B.3: Sample Matlab script to generate the theoretical spectra.

B.5 Additional data: HMIH$^+$

Table B.3: A summary of all investigated ensembles and subensembles for HMIH$^+$, i.e. HMI in a protic environment. The calculated g- and A-values are provided as mean of the corresponding subensemble. All A-values are given in MHz.

	theo_Solv-Set1000-QM/MM			**theo_Solv-Set400-QM/MM**			**theo_Solv-Set1000-vd**			**theo_Solv-Set400-vd**		
subensembles		1 H-bond	2 H-bond		1 H-bond	2 H-bond		1 H-bond	2 H-bond		1 H-bond	2 H-bond
# snapshots	1000	410	467	400	164	179	1000	410	467	400	164	179
g_{xx}	2.00845	2.00858	2.00832	2.00842	2.00857	2.00831	2.00940	2.00939	2.00944	2.00938	2.00941	2.00941
g_{yy}	2.00586	2.00589	2.00584	2.00585	2.00589	2.00583	2.00593	2.00609	2.00611	2.00594	2.00610	2.00610
g_{zz}	2.00214	2.00214	2.00214	2.00213	2.00213	2.00214	2.00210	2.00216	2.00216	2.00210	2.00216	2.00216
A_{xx}	6	6	7	10	10	10	4	4	4	6	7	6
A_{yy}	7	6	7	10	10	10	5	5	5	7	7	6
A_{zz}	87	85	89	89	87	90	74	74	74	74	74	74

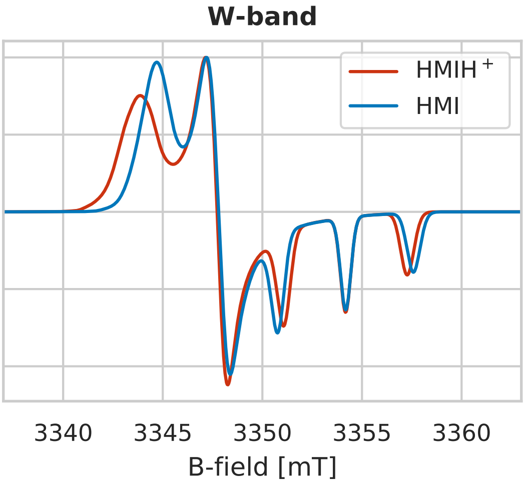

Figure B.5: Theoretical W-band spectrum of HMI and HMIH$^+$ in comparison based on the **theo_Solv-Set1000-QM/MM** ensemble.

List of Figures

List of Tables

List of Acronyms

AIMD	ab-initio molecular dynamics
ALW	apparent linewidth
AO	atomic orbital
CC	coupled cluster
CCD	coupled cluster doubles
CCSD	coupled cluster singles doubles
CCSDT	coupled cluster singles doubles triples
CCSD(T)	coupled cluster singles doubles and perturbative triples
CISD	configuration interaction singles doubles
CP-OO-MP2	coupled-perturbed orbital optimized MP2
CP-OO-RI-MP2	coupled-perturbed orbital optimized RI-MP2
CP-SCF	coupled-perturbed self-consistent field
cw	continuous wave
DFT	density functional theory
DHDF	double-hybrid density functional
DHDFT	double-hybrid density functional theory
DLPNO	domain based local pair natural orbital
DSD-DFT	spin-component scaled double-hybrid density functional theory
ECP	effective core potential
EC-RISM	embedded cluster reference interaction site model
EPR	electron paramagnetic resonance
FCI	full configuration interaction
FWHM	full width at half maximum

GGA	generalized gradient approximation
GIAO	gauge including atomic orbital
H-bond	hydrogen bond
HF	Hartree-Fock
HFC	hyperfine coupling
HFCC	hyperfine coupling constant
HF-SCF	Hartree-Fock self-consistent field
HMI	(3*R*,4*S*)-2,2,3,4,5,5-hexamethylimidazolidin-1-oxyl
KS	Kohn-Sham
LCAO	linear combination of atomic orbitals
LDA	local density approximation
LHS	left-hand side
MD	molecular dynamics
mGGA	meta-generalized gradient approximation
MM	molecular mechanics
MO	molecular orbital
MP2	second order Møller-Plesset perturbation theory
MPPT	Møller-Plesset perturbation theory
MR-CI	multi-reference configuration interaction
NMR	nuclear magnetic resonance
OEC	oxygen evolving complex
OO-MP2	orbital optimized MP2
PAO	pair atomic orbital
PNO	pair natural orbital
PT	perturbation theory
QC	quantum chemistry
QM	quantum mechanics
QM/MM	quantum mechanics/molecular mechanics
RSPT	Rayleigh Schrödinger perturbation theory

RHF	restricted Hartree-Fock
RHS	right-hand side
RI	resolution of the identity
SCF	self-consistent field
SE	Schrödinger equation
SH	Spin-Hamiltonian
SO	spin-orbit
SOC	spin-orbit coupling
SOMF(1X)	spin-orbit mean field one-center approximation
SORCI	spectroscopy oriented multi-reference configuration interaction
SOS	sum-over-states
SP	single point
UHF	unrestricted Hartree-Fock
XC	exchange correlation
ZORA	zeroth-order regular approximation

Bibliography

[1] Sharma, B.; Tran, V. A.; Pongratz, T.; Galazzo, L.; Zhurko, I.; Bordignon, E.; Kast, S. M.; Neese, F.; Marx, D. *Journal of Chemical Theory and Computation* **2021**, 6366, DOI: `10.1021/acs.jctc.1c00582`.

[2] Tran, V. A.; Neese, F. *The Journal of Chemical Physics* **2020**, *153*, 054105, DOI: `10.1063/5.0013799`.

[3] Tran, V. A.; Teucher, M.; Galazzo, L.; Sharma, B.; Pongratz, T.; Kast, S. M.; Marx, D.; Bordignon, E.; Schnegg, A.; Neese, F. *The Journal of Physical Chemistry A* **2023**, *127*, 6447, DOI: `10.1021/acs.jpca.3c02879`.

[4] Auer, A. A.; Tran, V. A.; Sharma, B.; Stoychev, G. L.; Marx, D.; Neese, F. *Molecular Physics* **2020**, *118*, e1797916, DOI: `10.1080/00268976.2020.1797916`.

[5] Tran, V. A.; Pernpointner, M. *Chemical Physics* **2018**, *509*, 151, DOI: `10.1016/j.chemphys.2017.10.001`.

[6] Neese, F. *Angewandte Chemie International Edition* **2017**, *56*, 11003, DOI: `10.1002/anie.201701163`.

[7] Neese, F.; Atanasov, M.; Bistoni, G.; Maganas, D.; Ye, S. *Journal of the American Chemical Society* **2019**, *141*, 2814, DOI: `10.1021/jacs.8b13313`.

[8] Barone, V.; Alessandrini, S.; Biczysko, M.; Cheeseman, J. R.; Clary, D. C.; McCoy, A. B.; DiRisio, R. J.; Neese, F.; Melosso, M.; Puzzarini, C. *Nature Reviews Methods Primers* **2021**, *1*, 38, DOI: `10.1038/s43586-021-00034-1`.

[9] Pantazis, D. A.; Ames, W.; Cox, N.; Lubitz, W.; Neese, F. *Angewandte Chemie* **2012**, *124*, 10074, DOI: `10.1002/ange.201204705`.

[10] Pantazis, D. A.; Ames, W.; Cox, N.; Lubitz, W.; Neese, F. *Angewandte Chemie International Edition* **2012**, *51*, 9935, DOI: `10.1002/anie.201204705`.

[11] Kanady, J. S.; Tsui, E. Y.; Day, M. W.; Agapie, T. *Science* **2011**, *333*, 733, DOI: `10.1126/science.1206036`.

[12] Mukherjee, S.; Stull, J. A.; Yano, J.; Stamatatos, T. C.; Pringouri, K.; Stich, T. A.; Abboud, K. A.; Britt, R. D.; Yachandra, V. K.; Christou, G. *Proceedings of the National Academy of Sciences* **2012**, *109*, 2257, DOI: `10.1073/pnas.1115290109`.

[13] Cox, N.; Retegan, M.; Neese, F.; Pantazis, D. A.; Boussac, A.; Lubitz, W. *Science* **2014**, *345*, 804, DOI: `10.1126/science.1254910`.

[14] Krewald, V.; Retegan, M.; Neese, F.; Lubitz, W.; Pantazis, D. A.; Cox, N. *Inorganic Chemistry* **2016**, *55*, 488, DOI: `10.1021/acs.inorgchem.5b02578`.

[15] Einsle, O.; Tezcan, F. A.; Andrade, S. L. A.; Schmid, B.; Yoshida, M.; Howard, J. B.; Rees, D. C. *Science* **2002**, *297*, 1696, DOI: `10.1126/science.1073877`.

[16] Lee, N.; Petrenko, T.; Bergmann, U.; Neese, F.; DeBeer, S. *Journal of the American Chemical Society* **2010**, *132*, 9715, DOI: `10.1021/ja101281e`.

[17] Lancaster, K. M.; Roemelt, M.; Ettenhuber, P.; Hu, Y.; Ribbe, M. W.; Neese, F.; Bergmann, U.; DeBeer, S. *Science* **2011**, *334*, 974, DOI: `10.1126/science.1206445`.

[18] Spatzal, T.; Aksoyoglu, M.; Zhang, L.; Andrade, S. L. A.; Schleicher, E.; Weber, S.; Rees, D. C.; Einsle, O. *Science* **2011**, *334*, 940, DOI: `10.1126/science.1214025`.

[19] Wiig, J. A.; Hu, Y.; Lee, C. C.; Ribbe, M. W. *Science* **2012**, *337*, 1672, DOI: `10.1126/science.1224603`.

[20] Neugebauer, J.; Scheffler, M. *Physical Review B* **1992**, *46*, 16067, DOI: `10.1103/PhysRevB.46.16067`.

[21] Wang, X.-G.; Weiss, W.; Shaikhutdinov, S.; Ritter, M.; Petersen, M.; Wagner, F.; Schlögl, R.; Scheffler, M. *Physical Review Letters* **1998**, *81*, 1038, DOI: `10.1103/PhysRevLett.81.1038`.

[22] Sauer, J. *Chemical Reviews* **1989**, *89*, 199, DOI: `10.1021/cr00091a006`.

[23] Golibrzuch, K.; Shirhatti, P. R.; Geweke, J.; Werdecker, J.; Kandratsenka, A.; Auerbach, D. J.; Wodtke, A. M.; Bartels, C. *Journal of the American Chemical Society* **2015**, *137*, 1465, DOI: `10.1021/ja509530k`.

[24] Wachs, I. E.; Weckhuysen, B. M. *Applied Catalysis A: General* **1997**, *157*, 67, DOI: `10.1016/S0926-860X(97)00021-5`.

[25] Maganas, D.; Trunschke, A.; Schlögl, R.; Neese, F. *Faraday Discussions* **2016**, *188*, 181, DOI: `10.1039/C5FD00193E`.

[26] Rozanska, X.; Fortrie, R.; Sauer, J. *Journal of the American Chemical Society* **2014**, *136*, 7751, DOI: `10.1021/ja503130z`.

[27] Kubas, A.; Berger, D.; Oberhofer, H.; Maganas, D.; Reuter, K.; Neese, F. *The Journal of Physical Chemistry Letters* **2016**, *7*, 4207, DOI: `10.1021/acs.jpclett.6b01845`.

[28] Dittmer, A.; Izsák, R.; Neese, F.; Maganas, D. *Inorganic Chemistry* **2019**, *58*, 9303, DOI: `10.1021/acs.inorgchem.9b00994`.

[29] Dittmer, A.; Stoychev, G. L.; Maganas, D.; Auer, A. A.; Neese, F. *Journal of Chemical Theory and Computation* **2020**, *16*, 6950, DOI: `10.1021/acs.jctc.0c00067`.

[30] Grimme, S.; Schreiner, P. R. *Angewandte Chemie International Edition* **2018**, *57*, 4170, DOI: `10.1002/anie.201709943`.

[31] Weil, J. A.; Bolton, J. R.; Wertz, J. E., *Electron Paramagnetic Resonance: Elementary Theory and Application*; Wiley-Interscience: New York, NY, 1994.

[32] Atherton, N. M., *Principles of Electron Spin Resonance*; Ellis Horwood Limited: New York, NY, 1993.

[33] Schweiger, A.; Jeschke, G., *Principles of Pulse Electron Paramagnetic Resonance*; Press, O. U., Ed., Oxford, 2005.

[34] Neese, F. In *eMagRes*; John Wiley & Sons, Ltd: Chichester, UK, 2017; Vol. 6, pp 1–22, DOI: `10.1002/9780470034590.emrstm1505`.

[35] Harriman, J. E., *Theoretical Foundations of Electron Spin Resonance*; Academic: New York, 1978.

[36] McWeeny, R. *The Journal of Chemical Physics* **1965**, *42*, 1717, DOI: `10.1063/1.1696183`.

[37] McWeeny, R., *Spins in Chemistry*; Academic Press: New York, NY, 1970.

[38] McWeeny, R., *Methods of Molecular Quantum Mechanics*; Academic Press: 1992, p 573.

[39] Gast, P.; Groenen, E. J. In *eMagRes*, Harris, R. K., Wasylishen, R. L., Eds.; John Wiley & Sons, Ltd: Chichester, UK, 2016, pp 1435–1444, DOI: `10.1002/9780470034590.emrstm1500`.

[40] Lushington, G. H.; Bündgen, P.; Grein, F. *International Journal of Quantum Chemistry* **1995**, *55*, 377, DOI: `10.1002/qua.560550503`.

[41] Lushington, G. H.; Grein, F. *Theoretica Chimica Acta* **1996**, *93*, 259.

[42] Angstl, R. *Chemical Physics* **1990**, *145*, 413, DOI: `10.1016/0301-0104(90)87050-L`.

[43] Ishii, M.; Morihashi, K.; Kikuchi, O. *Journal of Molecular Structure: THEOCHEM* **1991**, DOI: `10.1016/0166-1280(91)85083-J`.

[44] Moores, W. H.; McWeeny, R. *Proceedings of the Royal Society A: Mathematical, Physical and Engineering Sciences* **1973**, *332*, 365, DOI: `10.1098/rspa.1973.0031`.

[45] Geurts, P. J. M.; Bouten, P. C. P.; van der Avoird, A. *The Journal of Chemical Physics* **1980**, *73*, 1306, DOI: `10.1063/1.440243`.

[46] Ding, Z.; Gullá, A. F.; Budil, D. E. *The Journal of Chemical Physics* **2001**, *115*, 10685, DOI: `10.1063/1.1416177`.

[47] Neese, F. *The Journal of Chemical Physics* **2001**, *115*, 11080, DOI: `10.1063/1.1419058`.

[48] Lushington, G. H.; Grein, F. *International Journal of Quantum Chemistry* **1996**, *60*, 1679, DOI: `10.1002/(SICI)1097-461X(1996)60:7<1679::AID-QUA50>3.0.CO;2-T`.

[49] Lushington, G. H.; Grein, F. *Journal of Chemical Physics* **1997**, *106*, 3292, DOI: `10.1063/1.473077`.

[50] Neese, F. *Magnetic Resonance in Chemistry* **2004**, *42*, S187, DOI: `10.1002/mrc.1456`.

[51] van Gastel, M.; Lubitz, W.; Lassmann, G.; Neese, F. *Journal of the American Chemical Society* **2004**, *126*, 2237, DOI: `10.1021/ja038813l`.

[52] Gauss, J.; Kállay, M.; Neese, F. *The Journal of Physical Chemistry A* **2009**, *113*, 11541, DOI: `10.1021/jp9028535`.

[53] Perera, A.; Gauss, J.; Verma, P.; Morales, J. A. *The Journal of Chemical Physics* **2017**, *146*, 164104, DOI: `10.1063/1.4979680`.

[54] London, F. *Journal de Physique et le Radium* **1937**, *8*, 397, DOI: `10.1051/jphysrad:01937008010039700`.

[55] Schreckenbach, G.; Ziegler, T. *The Journal of Physical Chemistry A* **1997**, *101*, 3388, DOI: `10.1021/JP963060T`.

[56] Schreckenbach, G.; Ziegler, T. *International Journal of Quantum Chemistry* **1997**, *61*, 899, DOI: `10.1002/(SICI)1097-461X(1997)61:6<899::AID-QUA3>3.0.CO;2-R`.

[57] Schreckenbach, G.; Ziegler, T. *Theoretical Chemistry Accounts: Theory, Computation, and Modeling (Theoretica Chimica Acta)* **1998**, *99*, 71, DOI: `10.1007/s002140050306`.

[58] Neese, F.; Solomon, E. I. *Inorganic Chemistry* **1998**, *37*, 6568, DOI: `10.1021/IC980948I`.

[59] Patchkovskii, S.; Ziegler, T. *The Journal of Chemical Physics* **1999**, *111*, 5730, DOI: `10.1063/1.479869`.

[60] Patchkovskii, S.; Ziegler, T. *Journal of the American Chemical Society* **2000**, *122*, 3506, DOI: `10.1021/ja994041a`.

[61] Pople, J. A.; Krishnan, R.; Schlegel, H. B.; Binkley, J. S. *International Journal of Quantum Chemistry* **1979**, *16*, 225, DOI: `10.1002/qua.560160825`.

[62] Glasbrenner, M.; Vogler, S.; Ochsenfeld, C. *The Journal of Chemical Physics* **2018**, *148*, 214101, DOI: `10.1063/1.5028454`.

[63] Glasbrenner, M.; Vogler, S.; Ochsenfeld, C. *The Journal of Chemical Physics* **2019**, *150*, 024104, DOI: `10.1063/1.5066266`.

[64] Cherry, P. J.; Komorovsky, S.; Malkin, V. G.; Malkina, O. L. *Molecular Physics* **2017**, *115*, 75, DOI: `10.1080/00268976.2016.1191688`.

[65] van Lenthe, E.; Wormer, P. E. S.; van der Avoird, A. *The Journal of Chemical Physics* **1997**, *107*, 2488, DOI: `10.1063/1.474590`.

[66] Malkina, O. L.; Vaara, J.; Schimmelpfennig, B.; Munzarová, M.; Malkin, V. G.; Kaupp, M. *Journal of the American Chemical Society* **2000**, *122*, 9206, DOI: `10.1021/JA000984S`.

[67] Neese, F. *The Journal of Chemical Physics* **2005**, *122*, 034107, DOI: `10.1063/1.1829047`.

[68] Perdew, J. P.; Schmidt, K. In *AIP Conference Proceedings*, AIP: 2001; Vol. 577, pp 1–20, DOI: `10.1063/1.1390175`.

[69] Kaupp, M.; Reviakine, R.; Malkina, O. L.; Arbuznikov, A.; Schimmelpfennig, B.; Malkin, V. G. *Journal of Computational Chemistry* **2002**, *23*, 794, DOI: `10.1002/jcc.10049`.

[70] Frantz, S.; Hartmann, H.; Doslik, N.; Wanner, M.; Kaim, W.; Kümmerer, H.-J.; Denninger, G.; Barra, A.-L.; Duboc-Toia, C.; Fiedler, J.; Ciofini, I.; Urban, C.; Kaupp, M. *Journal of the American Chemical Society* **2002**, *124*, 10563, DOI: `10.1021/ja025829n`.

[71] Kaupp, M.; Gress, T.; Reviakine, R.; Malkina, O. L.; Malkin, V. G. *The Journal of Physical Chemistry B* **2003**, *107*, 331, DOI: `10.1021/jp026596p`.

[72] Komorovský, S.; Repiský, M.; Malkina, O. L.; Malkin, V. G.; Malkin, I.; Kaupp, M. *The Journal of Chemical Physics* **2006**, *124*, 084108, DOI: `10.1063/1.2173995`.

[73] Grimme, S. *The Journal of Chemical Physics* **2006**, *124*, 034108, DOI: `10.1063/1.2148954`.

[74] Goerigk, L.; Grimme, S. *Wiley Interdisciplinary Reviews: Computational Molecular Science* **2014**, *4*, 576, DOI: `10.1002/wcms.1193`.

[75] Neese, F.; Schwabe, T.; Grimme, S. *The Journal of Chemical Physics* **2007**, *126*, 124115, DOI: `10.1063/1.2712433`.

[76] Kossmann, S.; Neese, F. *Journal of Chemical Theory and Computation* **2010**, *6*, 2325, DOI: `10.1021/ct100199k`.

[77] Johnson, B. G.; Fisch, M. J. *The Journal of Chemical Physics* **1994**, *100*, 7429, DOI: `10.1063/1.466887`.

[78] Stanton, J. F.; Gauss, J.; Bartlett, R. J. *Chemical Physics Letters* **1992**, *195*, 194, DOI: `10.1016/0009-2614(92)86135-5`.

[79] Stoychev, G. L.; Auer, A. A.; Izsák, R.; Neese, F. *Journal of Chemical Theory and Computation* **2018**, *14*, 619, DOI: `10.1021/acs.jctc.7b01006`.

[80] Goldfarb, D. *Physical Chemistry Chemical Physics* **2006**, *8*, 2325, DOI: `10.1039/b601513c`.

[81] Le Breton, N.; Wright, J. J.; Jones, A. J. Y.; Salvadori, E.; Bridges, H. R.; Hirst, J.; Roessler, M. M. *Journal of the American Chemical Society* **2017**, *139*, 16319, DOI: `10.1021/jacs.7b09261`.

[82] Roessler, M. M.; Salvadori, E. *Chemical Society Reviews* **2018**, *47*, 2534, DOI: `10.1039/C6CS00565A`.

[83] Neese, F. *The Journal of Physical Chemistry A* **2001**, *105*, 4290, DOI: `10.1021/JP003254F`.

[84] Neese, F. *The Journal of Chemical Physics* **2003**, *118*, 3939, DOI: `10.1063/1.1540619`.

[85] Neese, F. *Coordination Chemistry Reviews* **2009**, *253*, 526, DOI: `10.1016/J.CCR.2008.05.014`.

[86] Chipman, D. M. *Theoretica Chimica Acta* **1992**, *82*, 93, DOI: `10.1007/BF01113132`.

[87] Feller, D.; Davidson, E. R. *Theoretica Chimica Acta* **1985**, *68*, 57, DOI: `10.1007/BF00698751`.

[88] Engels, B.; Peyerimhoff, S. D.; Davidson, E. *Molecular Physics* **1987**, *62*, 109, DOI: `10.1080/00268978700102091`.

[89] Bauschlicher, C. W.; Langhoff, S. R.; Partridge, H.; Chong, D. P. *The Journal of Chemical Physics* **1988**, *89*, 2985, DOI: `10.1063/1.455004`.

[90] Carmichael, I. *The Journal of Chemical Physics* **1989**, *91*, 1072, DOI: `10.1063/1.457179`.

[91] Chipman, D. M. In *Quantum Mechanical Electronic Structure Calculations with Chemical Accuracy*, Langhoff, S. R., Ed.; Springer Netherlands: Dordrecht, 1995, pp 109–138, DOI: `10.1007/978-94-011-0193-6_3`.

[92] Chipman, D. M. *The Journal of Chemical Physics* **1979**, *71*, 761, DOI: `10.1063/1.438364`.

[93] Chipman, D. M. *The Journal of Chemical Physics* **1983**, *78*, 4785, DOI: `10.1063/1.445283`.

[94] Hameka, H. F.; Turner, A. G. *Journal of Magnetic Resonance (1969)* **1985**, *64*, 66, DOI: `10.1016/0022-2364(85)90031-9`.

[95] Barone, V.; Adamo, C.; Russo, N. *Chemical Physics Letters* **1993**, *212*, 5, DOI: `10.1016/0009-2614(93)87099-O`.

[96] Ishii, N.; Shimizu, T. *Physical Review A* **1993**, *48*, 1691, DOI: `10.1103/PhysRevA.48.1691`.

[97] Kossmann, S.; Kirchner, B.; Neese, F. *Molecular Physics* **2007**, *105*, 2049, DOI: `10.1080/00268970701604655`.

[98] Improta, R.; Barone, V. *Chemical Reviews* **2004**, *104*, 1231, DOI: `10.1021/cr960085f`.

[99] Hermosilla, L.; Calle, P.; García de la Vega, J. M.; Sieiro, C. *The Journal of Physical Chemistry A* **2005**, *109*, 1114, DOI: `10.1021/jp0466901`.

[100] Barone, V.; Cimino, P. *Chemical Physics Letters* **2008**, *454*, 139, DOI: `10.1016/j.cplett.2008.01.080`.

[101] Ciofini, I.; Adamo, C.; Barone, V. *The Journal of Chemical Physics* **2004**, *121*, 6710, DOI: `10.1063/1.1791031`.

[102] Adamo, C.; Cossi, M.; Barone, V. *Journal of Molecular Structure: THEOCHEM* **1999**, *493*, 145, DOI: `10.1016/S0166-1280(99)00235-3`.

[103] Engels, B.; Peyerimhoff, S.; Karna, S.; Grein, F. *Chemical Physics Letters* **1988**, *152*, 397, DOI: `10.1016/0009-2614(88)80113-1`.

[104] Engels, B.; Eriksson, L. A.; Lunell, S. In *Advances in Quantum Chemistry*; Elsevier: 1996; Vol. 27, pp 297–369, DOI: `10.1016/S0065-3276(08)60254-3`.

[105] Saitow, M.; Becker, U.; Riplinger, C.; Valeev, E. F.; Neese, F. *The Journal of Chemical Physics* **2017**, *146*, 164105, DOI: `10.1063/1.4981521`.

[106] Cossi, M.; Rega, N.; Scalmani, G.; Barone, V. *Journal of Computational Chemistry* **2003**, *24*, 669, DOI: `10.1002/jcc.10189`.

[107] Tomasi, J.; Mennucci, B.; Cammi, R. *Chemical Reviews* **2005**, *105*, 2999, DOI: `10.1021/cr9904009`.

[108] *Continuum Solvation Models in Chemical Physics*; Mennucci, B., Cammi, R., Eds.; John Wiley & Sons, Ltd: Chichester, UK, 2007, DOI: `10.1002/9780470515235`.

[109] Cramer, C. J.; Truhlar, D. G. *Accounts of Chemical Research* **2008**, *41*, 760, DOI: `10.1021/ar800019z`.

[110] Fennell, C. J.; Dill, K. A. *Journal of Statistical Physics* **2011**, *145*, 209, DOI: `10.1007/s10955-011-0232-9`.

[111] Asher, J. R.; Kaupp, M. *ChemPhysChem* **2007**, *8*, 69, DOI: `10.1002/cphc.200600325`.

[112] Pavone, M.; Benzi, C.; De Angelis, F.; Barone, V. *Chemical Physics Letters* **2004**, *395*, 120, DOI: `10.1016/j.cplett.2004.07.054`.

[113] Marx, D.; Hutter, J., *Ab Initio Molecular Dynamics: Basic Theory and Advanced Methods*; Cambridge University Press: 2009.

[114] Cimino, P.; Neese, F.; Barone, V. In *Computational Spectroscopy*, Grunenberg, J., Ed., First; Wiley: 2010, pp 63–104, DOI: `10.1002/9783527633272.ch3`.

[115] Zerbetto, M.; Carlotto, S.; Polimeno, A.; Corvaja, C.; Franco, L.; Toniolo, C.; Formaggio, F.; Barone, V.; Cimino, P. *The Journal of Physical Chemistry B* **2007**, *111*, 2668, DOI: `10.1021/jp066908e`.

[116] Barone, V.; Polimeno, A. *Physical Chemistry Chemical Physics* **2006**, *8*, 4609, DOI: `10.1039/b607998a`.

[117] Bordignon, E. In *eMagRes*; John Wiley & Sons, Ltd: Chichester, UK, 2017, pp 235–254, DOI: `10.1002/9780470034590.emrstm1513`.

[118] *Nitroxides: Synthesis, Properties and Applications*; Ouari, O., Gigmes, D., Eds.; Royal Society of Chemistry: Cambridge, 2021.

[119] Haywood, R. In *Encyclopedia of Biophysics*, Roberts, G. C. K., Ed.; Springer Berlin Heidelberg: Berlin, Heidelberg, 2013, pp 2447–2453, DOI: `10.1007/978-3-642-16712-6_579`.

[120] Eaton, S. S.; Eaton, G. R. In *Distance Measurements in Biological Systems by EPR*, Berliner, L. J., Eaton, G. R., Eaton, S. S., Eds.; Springer US: Boston, MA, 2002; Vol. 19, pp 1–27, DOI: `10.1007/0-306-47109-4_1`.

[121] Jeschke, G. In *eMagRes*, Harris, R. K., Wasylishen, R. L., Eds.; John Wiley & Sons, Ltd: Chichester, UK, 2016, pp 1459–1476, DOI: `10.1002/9780470034590.emrstm1518`.

[122] Eaton, S. S.; Eaton, G. R. *Journal of Magnetic Resonance* **2012**, *223*, 151, DOI: `10.1016/j.jmr.2012.07.025`.

[123] Plato, M.; Steinhoff, H.-J.; Wegener, C.; Törring, J. T.; Savitsky, A.; Möbius, K. *Molecular Physics* **2002**, *100*, 3711, DOI: `10.1080/00268970210166246`.

[124] Owenius, R.; Engström, M.; Lindgren, M.; Huber, M. *The Journal of Physical Chemistry A* **2001**, *105*, 10967, DOI: `10.1021/jp0116914`.

[125] Bordignon, E.; Brutlach, H.; Urban, L.; Hideg, K.; Savitsky, A.; Schnegg, A.; Gast, P.; Engelhard, M.; Groenen, E. J. J.; Möbius, K.; Steinhoff, H.-J. *Applied Magnetic Resonance* **2010**, *37*, 391, DOI: `10.1007/s00723-009-0072-9`.

[126] Haugland, M. M.; Anderson, E. A.; Lovett, J. E. In 2016, pp 1–34, DOI: `10.1039/9781782629436-00001`.

[127] Gast, P.; Herbonnet, R. T. L.; Klare, J.; Nalepa, A.; Rickert, C.; Stellinga, D.; Urban, L.; Möbius, K.; Savitsky, A.; Steinhoff, H.-J.; Groenen, E. J. J. *Phys. Chem. Chem. Phys.* **2014**, *16*, 15910, DOI: `10.1039/C4CP01741B`.

[128] Nalepa, A.; Möbius, K.; Plato, M.; Lubitz, W.; Savitsky, A. *Applied Magnetic Resonance* **2019**, *50*, 1, DOI: `10.1007/s00723-018-1073-3`.

[129] Bordignon, E.; Nalepa, A. I.; Savitsky, A.; Braun, L.; Jeschke, G. *The Journal of Physical Chemistry B* **2015**, *119*, 13797, DOI: `10.1021/acs.jpcb.5b04104`.

[130] Hagen, W. R., *Biomolecular EPR Spectroscopy*; CRC Press, Taylor & Francis Group: Boca Raton London New York, 2009.

[131] Jeschke, G.; Polyhach, Y. *Physical Chemistry Chemical Physics* **2007**, *9*, 1895, DOI: `10.1039/b614920k`.

[132] Hagen, W. R. In *Advances in Inorganic Chemistry*; Academic Press: 1992; Vol. 38, pp 165–222, DOI: `10.1016/S0898-8838(08)60064-1`.

[133] Hagen, W.; Hearshen, D.; Harding, L.; Dunham, W. *Journal of Magnetic Resonance* **1985**, *61*, 233, DOI: `10.1016/0022-2364(85)90078-2`.

[134] Pilbrow, J. *Journal of Magnetic Resonance (1969)* **1984**, *58*, 186, DOI: `10.1016/0022-2364(84)90209-9`.

[135] Savitsky, A.; Nalepa, A.; Petrenko, T.; Plato, M.; Möbius, K.; Lubitz, W. *Applied Magnetic Resonance* **2021**, DOI: `10.1007/s00723-021-01442-y`.

[136] Neese, F. *Wiley Interdisciplinary Reviews: Computational Molecular Science* **2012**, *2*, 73, DOI: `10.1002/wcms.81`.

[137] Neese, F. *Wiley Interdisciplinary Reviews: Computational Molecular Science* **2018**, *8*, e1327, DOI: `10.1002/wcms.1327`.

[138] Neese, F.; Wennmohs, F.; Becker, U.; Riplinger, C. *The Journal of Chemical Physics* **2020**, *152*, 224108, DOI: `10.1063/5.0004608`.

[139] Schrödinger, E. *Physical Review* **1926**, *28*, 1049, DOI: `10.1103/PhysRev.28.1049`.

[140] Slater, J. C. *Physical Review* **1951**, *81*, 385, DOI: `10.1103/PhysRev.81.385`.

[141] Slater, J. C. *Physical Review* **1953**, *91*, 528, DOI: `10.1103/PhysRev.91.528`.

[142] Slater, J. C. *Physical Review* **1929**, *34*, 1293, DOI: `10.1103/PhysRev.34.1293`.

[143] Condon, E. U. *Physical Review* **1930**, *36*, 1121, DOI: `10.1103/PhysRev.36.1121`.

[144] Szabo, A.; Ostlund, N. S., *Modern Quantum Chemistry: Introduction to Advanced Electronic Structure Theory*; Dover Publications: 1989.

[145] Roothaan, C. C. J. *Reviews of Modern Physics* **1951**, *23*, 69, DOI: `10.1103/RevModPhys.23.69`.

[146] Hall, G. G. *Proceedings of the Royal Society of London. Series A. Mathematical and Physical Sciences* **1951**, *205*, 541, DOI: `10.1098/rspa.1951.0048`.

[147] Pople, J. A.; Nesbet, R. K. *The Journal of Chemical Physics* **1954**, *22*, 571, DOI: `10.1063/1.1740120`.

[148] Jensen, F., *Introduction to Computational Chemistry*, Third edition; Wiley: Chichester, UK ; Hoboken, NJ, 2017.

[149] Cramer, C. J., *Essentials of Computational Chemistry: Theories and Models*, 2nd ed; Wiley: Chichester, West Sussex, England ; Hoboken, NJ, 2004.

[150] Jensen, P.; Bunker, P. R., *Computational Molecular Spectroscopy*; Wiley: Chichester ; New York, 2000.

[151] Helgaker, T.; Jørgensen, P.; Olsen, J., *Molecular Electronic-Structure Theory*; John Wiley & Sons, Ltd: Chichester, UK, 2000, DOI: `10.1002/9781119019572`.

[152] Møller, C.; Plesset, M. S. *Physical Review* **1934**, *46*, 618, DOI: `10.1103/PhysRev.46.618`.

[153] Hylleraas, E. A. *Zeitschrift für Physik* **1930**, *65*, 209, DOI: `10.1007/BF01397032`.

[154] Pulay, P.; Saebø, S. *Theoretica Chimica Acta* **1986**, *69*, 357, DOI: `10.1007/BF00526697`.

[155] Vahtras, O.; Almlöf, J.; Feyereisen, M. *Chemical Physics Letters* **1993**, *213*, 514, DOI: `10.1016/0009-2614(93)89151-7`.

[156] Feyereisen, M.; Fitzgerald, G.; Komornicki, A. *Chemical Physics Letters* **1993**, *208*, 359, DOI: `10.1016/0009-2614(93)87156-W`.

[157] Weigend, F.; Häser, M.; Patzelt, H.; Ahlrichs, R. *Chemical Physics Letters* **1998**, *294*, 143, DOI: `10.1016/S0009-2614(98)00862-8`.

[158] Pulay, P. *Chemical Physics Letters* **1983**, *100*, 151, DOI: `10.1016/0009-2614(83)80703-9`.

[159] Pulay, P.; Saebø, S.; Meyer, W. *The Journal of Chemical Physics* **1984**, *81*, 1901, DOI: `10.1063/1.447863`.

[160] Handy, N. C.; Schaefer III, H. F. *The Journal of Chemical Physics* **1984**, *81*, 5031, DOI: `10.1063/1.447489`.

[161] Salter, E.; Trucks, G. W.; Fitzgerald, G.; Bartlett, R. J. *Chemical Physics Letters* **1987**, *141*, 61, DOI: `10.1016/0009-2614(87)80093-3`.

[162] Salter, E. A.; Trucks, G. W.; Bartlett, R. J. *The Journal of Chemical Physics* **1989**, *90*, 1752, DOI: `10.1063/1.456069`.

[163] Weigend, F.; Häser, M. *Theoretical Chemistry Accounts: Theory, Computation, and Modeling* (*Theoretica Chimica Acta*) **1997**, *97*, 331, DOI: `10.1007/s002140050269`.

[164] Neese, F. *Molecular Physics* **2007**, *105*, 2507, DOI: `10.1080/00268970701549389`.

[165] Weigend, F. *Physical Chemistry Chemical Physics* **2002**, *4*, 4285, DOI: `10.1039/b204199p`.

[166] Neese, F.; Wennmohs, F.; Hansen, A.; Becker, U. *Chemical Physics* **2009**, *356*, 98, DOI: `10.1016/j.chemphys.2008.10.036`.

[167] Stoychev, G. L.; Auer, A. A.; Neese, F. *Journal of Chemical Theory and Computation* **2018**, *14*, 4756, DOI: `10.1021/acs.jctc.8b00624`.

[168] Scuseria, G. E.; Schaefer, H. F. *Chemical Physics Letters* **1987**, *142*, 354, DOI: `10.1016/0009-2614(87)85122-9`.

[169] Adamowicz, L.; Bartlett, R. J. *The Journal of Chemical Physics* **1987**, *86*, 6314, DOI: `10.1063/1.452468`.

[170] Adamowicz, L.; Bartlett, R. J.; Sadlej, A. J. *The Journal of Chemical Physics* **1988**, *88*, 5749, DOI: `10.1063/1.454721`.

[171] Lochan, R. C.; Head-Gordon, M. *The Journal of Chemical Physics* **2007**, *126*, 164101, DOI: `10.1063/1.2718952`.

[172] Neese, F.; Schwabe, T.; Kossmann, S.; Schirmer, B.; Grimme, S. *Journal of Chemical Theory and Computation* **2009**, *5*, 3060, DOI: `10.1021/ct9003299`.

[173] Bozkaya, U.; Turney, J. M.; Yamaguchi, Y.; Schaefer, H. F.; Sherrill, C. D. *The Journal of Chemical Physics* **2011**, *135*, 104103, DOI: `10.1063/1.3631129`.

[174] Čížek, J. *The Journal of Chemical Physics* **1966**, *45*, 4256, DOI: `10.1063/1.1727484`.

[175] Paldus, J. In *New Horizons of Quantum Chemistry*; Springer Netherlands: Dordrecht, 1983, pp 31–60, DOI: `10.1007/978-94-009-7950-5_5`.

[176] Paldus, J. In *Methods in Computational Molecular Physics*, Wilson, S., Diercksen, G. H. F., Eds.; Springer US: Boston, MA, 1992; Vol. 293, pp 99–194, DOI: `10.1007/978-1-4615-7419-4_7`.

[177] Bartlett, R. J.; Dykstra, C. E.; Paldus, J. In *Advanced Theories and Computational Approaches to the Electronic Structure of Molecules*; Springer Netherlands: Dordrecht, 1984, pp 127–159, DOI: `10.1007/978-94-009-6451-8_8`.

[178] Raghavachari, K.; Trucks, G. W.; Pople, J. A.; Head-Gordon, M. *Chemical Physics Letters* **1989**, *157*, 479, DOI: `10.1016/S0009-2614(89)87395-6`.

[179] Sæbø, S.; Pulay, P. *Chemical Physics Letters* **1985**, *113*, 13, DOI: `10.1016/0009-2614(85)85003-X`.

[180] Sæbø, S.; Pulay, P. *The Journal of Chemical Physics* **1987**, *86*, 914, DOI: `10.1063/1.452293`.

[181] Sæbø, S.; Pulay, P. *The Journal of Chemical Physics* **1988**, *88*, 1884, DOI: `10.1063/1.454111`.

[182] Hampel, C.; Werner, H.-J. *The Journal of Chemical Physics* **1998**, *104*, 6286, DOI: `10.1063/1.471289`.

[183] Schütz, M.; Hetzer, G.; Werner, H.-J. *The Journal of Chemical Physics* **1999**, *111*, 5691, DOI: `10.1063/1.479957`.

[184] Schütz, M.; Werner, H.-J. *Chemical Physics Letters* **2000**, *318*, 370, DOI: `10.1016/S0009-2614(00)00066-X`.

[185] Schütz, M.; Werner, H.-J. *The Journal of Chemical Physics* **2001**, *114*, 661, DOI: `10.1063/1.1330207`.

[186] Pinski, P.; Riplinger, C.; Valeev, E. F.; Neese, F. *The Journal of Chemical Physics* **2015**, *143*, 034108, DOI: `10.1063/1.4926879`.

[187] Meyer, W. *The Journal of Chemical Physics* **1973**, *58*, 1017, DOI: `10.1063/1.1679283`.

[188] Ahlrichs, R.; Driessler, F.; Lischka, H.; Staemmler, V.; Kutzelnigg, W. *The Journal of Chemical Physics* **1975**, *62*, 1235, DOI: `10.1063/1.430638`.

[189] Ahlrichs, R.; Driessler, F. *Theoretica Chimica Acta* **1975**, *36*, 275, DOI: `10.1007/BF00549691`.

[190] Taylor, P. R.; Bacskay, G.; Hush, N.; Hurley, A. *Chemical Physics Letters* **1976**, *41*, 444, DOI: `10.1016/0009-2614(76)85390-0`.

[191] Neese, F.; Wennmohs, F.; Hansen, A. *The Journal of Chemical Physics* **2009**, *130*, 114108, DOI: `10.1063/1.3086717`.

[192] Neese, F.; Hansen, A.; Liakos, D. G. *The Journal of Chemical Physics* **2009**, *131*, 064103, DOI: `10.1063/1.3173827`.

[193] Riplinger, C.; Pinski, P.; Becker, U.; Valeev, E. F.; Neese, F. *The Journal of Chemical Physics* **2016**, *144*, 024109, DOI: `10.1063/1.4939030`.

[194] Guo, Y.; Riplinger, C.; Becker, U.; Liakos, D. G.; Minenkov, Y.; Cavallo, L.; Neese, F. *The Journal of Chemical Physics* **2018**, *148*, 011101, DOI: `10.1063/1.5011798`.

[195] Guo, Y.; Riplinger, C.; Liakos, D. G.; Becker, U.; Saitow, M.; Neese, F. *Journal of Chemical Physics* **2020**, *152*, DOI: `10.1063/1.5127550`.

[196] Pinski, P.; Neese, F. *The Journal of Chemical Physics* **2018**, *148*, 031101, DOI: `10.1063/1.5011204`.

[197] Saitow, M.; Neese, F. *The Journal of Chemical Physics* **2018**, *149*, 034104, DOI: `10.1063/1.5027114`.

[198] Stoychev, G. L.; Auer, A. A.; Gauss, J.; Neese, F. *The Journal of Chemical Physics* **2021**, *154*, 164110, DOI: `10.1063/5.0047125`.

[199] Guo, Y.; Sivalingam, K.; Valeev, E. F.; Neese, F. *The Journal of Chemical Physics* **2016**, *144*, 094111, DOI: `10.1063/1.4942769`.

[200] Pavošević, F.; Pinski, P.; Riplinger, C.; Neese, F.; Valeev, E. F. *The Journal of Chemical Physics* **2016**, *144*, 144109, DOI: `10.1063/1.4945444`.

[201] Hohenberg, P.; Kohn, W. *Physical Review* **1964**, *136*, B864, DOI: `10.1103/PhysRev.136.B864`.

[202] Kohn, W.; Sham, L. J. *Physical Review* **1965**, *140*, A1133, DOI: `10.1103/PhysRev.140.A1133`.

[203] Atkins, P. W.; Friedman, R., *Molecular Quantum Mechanics*, 5th ed; Oxford University Press: Oxford ; New York, 2011.

[204] Lee, C.; Yang, W.; Parr, R. G. *Physical Review B* **1988**, *37*, 785, DOI: `10.1103/PhysRevB.37.785`.

[205] Becke, A. D. *The Journal of Chemical Physics* **1993**, *98*, 5648, DOI: `10.1063/1.464913`.

[206] Kozuch, S.; Gruzman, D.; Martin, J. M. L. *The Journal of Physical Chemistry C* **2010**, *114*, 20801, DOI: `10.1021/jp1070852`.

[207] Kozuch, S.; Martin, J. M. L. *Physical Chemistry Chemical Physics* **2011**, *13*, 20104, DOI: `10.1039/c1cp22592h`.

[208] Kozuch, S.; Martin, J. M. L. *Journal of Computational Chemistry* **2013**, *34*, 2327, DOI: `10.1002/jcc.23391`.

[209] Grimme, S.; Antony, J.; Schwabe, T.; Mück-Lichtenfeld, C. *Org. Biomol. Chem.* **2007**, *5*, 741, DOI: `10.1039/B615319B`.

[210] Gräfenstein, J.; Cremer, D. *The Journal of Chemical Physics* **2009**, *130*, 124105, DOI: `10.1063/1.3079822`.

[211] Johnson, E. R.; Mackie, I. D.; DiLabio, G. A. *Journal of Physical Organic Chemistry* **2009**, *22*, 1127, DOI: `10.1002/poc.1606`.

[212] Sato, T.; Nakai, H. *The Journal of Chemical Physics* **2009**, *131*, 224104, DOI: `10.1063/1.3269802`.

[213] Bursch, M.; Mewes, J.-M.; Hansen, A.; Grimme, S. *Angewandte Chemie International Edition* **2022**, *61*, DOI: `10.1002/anie.202205735`.

[214] Kraka, E.; Gauss, J.; Cremer, D. *Journal of Molecular Structure: THEOCHEM* **1991**, *234*, 95, DOI: `10.1016/0166-1280(91)89008-O`.

[215] Gauss, J. In *Modern Methods and Algorithms of Quantum Chemistry*, 2000; Vol. 1, pp 509–560.

[216] Yamaguchi, Y.; Osamura, Y.; Goddard, J. D.; Schaefer, H. F., *A New Dimension to Quantum Chemistry. Analytic Derivative Methods in Ab Initio Molecular Electronic Structure Theory.* Oxford University Press: Oxford: 1994.

[217] Gerratt, J.; Mills, I. M. *The Journal of Chemical Physics* **1968**, *49*, 1719, DOI: `10.1063/1.1670299`.

[218] Pople, J. A.; Gill, P. M.; Johnson, B. G. *Chemical Physics Letters* **1992**, *199*, 557, DOI: `10.1016/0009-2614(92)85009-Y`.

[219] Stoll, S.; Schweiger, A. *Journal of Magnetic Resonance* **2006**, *178*, 42, DOI: `10.1016/j.jmr.2005.08.013`.

[220] Neese, F. In *High Resolution EPR*, Berliner, L., Hanson, G., Eds.; Springer New York: New York, NY, 2009; Vol. 28, pp 175–229, DOI: `10.1007/978-0-387-84856-3_5`.

[221] Neese, F. *Chemical Physics Letters* **2003**, *380*, 721, DOI: `10.1016/J.CPLETT.2003.09.047`.

[222] Remenyi, C.; Reviakine, R.; Arbuznikov, A. V.; Vaara, J.; Kaupp, M. *The Journal of Physical Chemistry A* **2004**, *108*, 5026, DOI: `10.1021/jp049395p`.

[223] Arbuznikov, A. V.; Vaara, J.; Kaupp, M. *The Journal of Chemical Physics* **2004**, *120*, 2127, DOI: `10.1063/1.1636720`.

[224] Hedegård, E. D.; Kongsted, J.; Sauer, S. P. A. *Journal of Chemical Theory and Computation* **2013**, *9*, 2380, DOI: `10.1021/ct400171c`.

[225] Angstl, R. *Chemical Physics* **1989**, *132*, 435, DOI: `10.1016/0301-0104(89)80038-2`.

[226] Stone, A. J. *Proceedings of the Royal Society A: Mathematical, Physical and Engineering Sciences* **1963**, *271*, 424, DOI: `10.1098/rspa.1963.0027`.

[227] Mills, I.; Cvitas, T.; Homann, K.; Kallay, N.; Kuchitsu, K., *Quantities, Units and Symbols in Physical Chemistry*, 2nd editio; Blackwell Science: London, 1993.

[228] Koseki, S.; Schmidt, M. W.; Gordon, M. S. *The Journal of Physical Chemistry* **1992**, *96*, 10768, DOI: `10.1021/j100205a033`.

[229] Heß, B. A.; Marian, C. M.; Wahlgren, U.; Gropen, O. *Chemical Physics Letters* **1996**, *251*, 365, DOI: `10.1016/0009-2614(96)00119-4`.

[230] Kutzelnigg, W. *Journal of Molecular Structure: THEOCHEM* **1989**, *202*, 11, DOI: `10.1016/0166-1280(89)87003-4`.

[231] Ditchfield, R. *Molecular Physics* **1974**, *27*, 789, DOI: `10.1080/00268977400100711`.

[232] Helgaker, T.; Jorgensen, P. *The Journal of Chemical Physics* **1991**, *95*, 2595, DOI: `10.1063/1.460912`.

[233] Neese, F. In *Electron Paramagnetic Resonance: Volume 20*; The Royal Society of Chemistry: 2006, pp 73–95, DOI: `10.1039/9781847557568-00073`.

[234] Fritz, J.; Anderson, R.; Fee, J.; Palmer, G.; Sands, R.; Tsibris, J.; Gunsalus, I.; Orme-Johnson, W.; Beinert, H. *Biochimica et Biophysica Acta (BBA) - Bioenergetics* **1971**, *253*, 110, DOI: `10.1016/0005-2728(71)90239-8`.

[235] Jayatilaka, D. *The Journal of Chemical Physics* **1998**, *108*, 7587, DOI: `10.1063/1.476193`.

[236] Weigend, F.; Ahlrichs, R. *Physical Chemistry Chemical Physics* **2005**, *7*, 3297, DOI: `10.1039/b508541a`.

[237] Dunning, T. H. *The Journal of Chemical Physics* **1989**, *90*, 1007, DOI: `10.1063/1.456153`.

[238] Kendall, R. A.; Dunning, T. H.; Harrison, R. J. *The Journal of Chemical Physics* **1992**, *96*, 6796, DOI: `10.1063/1.462569`.

[239] Krylov, A. I. In *Reviews in Computational Chemistry*; John Wiley & Sons, Inc.: 2017; Chapter 4, pp 151–224, DOI: `10.1002/9781119356059.ch4`.

[240] Byrd, E. F. C.; Sherrill, C. D.; Head-Gordon, M. *The Journal of Physical Chemistry A* **2001**, *105*, 9736, DOI: `10.1021/jp011132x`.

[241] Farnell, L.; Pople, J. A.; Radom, L. *The Journal of Physical Chemistry* **1983**, *87*, 79, DOI: `10.1021/j100224a019`.

[242] Tozer, D. J.; Handy, N. C.; Amos, R. D.; Pople, J. A.; Nobes, R. H.; Xie, Y.; Schaefer, H. F. *Molecular Physics* **1993**, *79*, 777, DOI: `10.1080/00268979300101621`.

[243] Jensen, F. *Chemical Physics Letters* **1990**, *169*, 519, DOI: `10.1016/0009-2614(90)85641-0`.

[244] Neese, F.; Hansen, A.; Wennmohs, F.; Grimme, S. *Accounts of Chemical Research* **2009**, *42*, 641, DOI: `10.1021/ar800241t`.

[245] Parkinson, C. J.; Mayer, P. M.; Radom, L. *Theoretical Chemistry Accounts: Theory, Computation, and Modeling (Theoretica Chimica Acta)* **1999**, *102*, 92, DOI: `10.1007/s002140050477`.

[246] Kossmann, S.; Neese, F. *The Journal of Physical Chemistry A* **2010**, *114*, 11768, DOI: `10.1021/jp105647c`.

[247] Bozkaya, U. *Journal of Chemical Theory and Computation* **2014**, *10*, 2371, DOI: `10.1021/ct500231c`.

[248] Zhang, Y.; Yang, W. *Physical Review Letters* **1998**, *80*, 890, DOI: `10.1103/PhysRevLett.80.890`.

[249] Hättig, C. *Phys. Chem. Chem. Phys.* **2005**, *7*, 59, DOI: `10.1039/B415208E`.

[250] Huang, J.; Rauscher, S.; Nawrocki, G.; Ran, T.; Feig, M.; de Groot, B. L.; Grubmüller, H.; MacKerell, A. D. *Biophysical Journal* **2017**, *112*, 175a.

[251] Imoto, S.; Forbert, H.; Marx, D. *Physical Chemistry Chemical Physics* **2015**, *17*, 24224, DOI: `10.1039/C5CP03069B`.

[252] Kirilina, E. P.; Prisner, T. F.; Bennati, M.; Endeward, B.; Dzuba, S. A.; Fuchs, M. R.; Möbius, K.; Schnegg, A. *Magnetic Resonance in Chemistry* **2005**, *43*, S119, DOI: `10.1002/mrc.1677`.

[253] Pavone, M.; Cimino, P.; Crescenzi, O.; Sillanpää, A.; Barone, V. *The Journal of Physical Chemistry B* **2007**, *111*, 8928, DOI: `10.1021/jp0727805`.

[254] More, C.; Bertrand, P.; Gayda, J. *Journal of Magnetic Resonance (1969)* **1987**, *73*, 13, DOI: `10.1016/0022-2364(87)90221-6`.

[255] Bratt, P. J.; Ringus, E.; Hassan, A.; Tol, H. V.; Maniero, A.-L.; Brunel, L.-C.; Rohrer, M.; Bubenzer-Hange, C.; Scheer, H.; Angerhofer, A. *The Journal of Physical Chemistry B* **1999**, *103*, 10973, DOI: `10.1021/jp992885a`.

[256] Duboc-Toia, C.; Hassan, A. K.; Mulliez, E.; Ollagnier-de Choudens, S.; Fontecave, M.; Leutwein, C.; Heider, J. *Journal of the American Chemical Society* **2003**, *125*, 38, DOI: `10.1021/ja026690j`.